REPORT DOCUMENTATION PAGE

Form Approved
OMB No. 0704-0188

PLEASE DO NOT RETURN YOUR FORM TO THE ABOVE ORGANIZATION.

1. REPORT DATE *(DD-MM-YYYY)*	2. REPORT TYPE	3. DATES COVERED *(From - To)*
13-02-2012	Final Report	01-06-2008-30-11-2011

4. TITLE AND SUBTITLE
Near-Field Propagation of Sub-Nanosecond Electric Pulses into Amorphous Masses

5a. CONTRACT NUMBER
FA9550-08-1-0191

5b. GRANT NUMBER

5c. PROGRAM ELEMENT NUMBER

6. AUTHOR(S)
Xiao, Shu
Schoenbach, Karl, H.

5d. PROJECT NUMBER

5e. TASK NUMBER

5f. WORK UNIT NUMBER

7. PERFORMING ORGANIZATION NAME(S) AND ADDRESS(ES)
Frank Reidy Research Center for Bioelectrics,
4211 Monarch Way, Ste. 300
Old Dominion University, Norfolk, VA 23508

8. PERFORMING ORGANIZATION REPORT NUMBER

9. SPONSORING/MONITORING AGENCY NAME(S) AND ADDRESS(ES)
Air Force Office of Scientific Research
875 N. Randolph St., Arlington, VA 22203-1977

10. SPONSOR/MONITOR'S ACRONYM(S)
AFOSR

11. SPONSOR/MONITOR'S REPORT NUMBER(S)
AFRL-OSR-VA-TR-2012-0965

12. DISTRIBUTION/AVAILABILITY STATEMENT
Distribution A - Approved for Public Release

13. SUPPLEMENTARY NOTES

14. ABSTRACT

The project, "Near-Field Propagation of Sub-Nanosecond Electric Pulses into Amorphous Masses", deals with the propagation of subnanosecond pulsed radiation in the near field region and its use in probing inhomogeneities in dielectrics. It also explores the possibility of changing the physical structure of lossy dielectrics by using very intense pulses. A subnanosecond high voltage pulse generator was constructed, which is able to deliver 150 ps (FWHM) pulses with 100 ps risetime (10%-90%). The maximum voltage is 17 kV and the repetition rate is 20 Hz. A prolate-spheroidal reflector antenna focuses subnanosecond pulsed electromagnetic radiation in the near field and its power density distribution has a full-width at half-maximum (FWHM) width of 32 cm in the axial direction and 10 cm in the lateral direction. The peak electric field inside the lens is 1.4 times of that in air and the spot size is decreased by a factor of 2. A focusing antenna in conjunction with a dielectric lens has been shown to have a resolution of approximately 4 cm. Subnanosecond electric pulses (200 ps) at electric field intensities on the order of 20 kV/cm cause the death of biological cells and the increased transport across the membrane at much lower exposure times or number of pulses.

15. SUBJECT TERMS
Subnanosecond pulses, focusing, antennas, lens, target detection, cell response

16. SECURITY CLASSIFICATION OF:			17. LIMITATION OF ABSTRACT	18. NUMBER OF PAGES	19a. NAME OF RESPONSIBLE PERSON
a. REPORT	b. ABSTRACT	c. THIS PAGE			Dr. John Luginsland
U	U	U	U	52	19b. TELEPHONE NUMBER *(Include area code)* 703-696-8574

Near-Field Propagation of Sub-Nanosecond Electric Pulses into Amorphous Masses

Final Report

(February 1, 2012)

Submitted to

John Luginsland

Air Force Office of Scientific Research

875 N. Randolph St., Arlington, VA 22203-1977
Phone: (703) 696-8574

FAX: (703) 696-8481

By

Shu Xiao (PI)

and

Karl H. Schoenbach (Co-PI)

Frank Reidy Research Center for Bioelectrics

4211 Monarch Way, Suite 300

Old Dominion University

Norfolk, VA, 23510

Phone: 757-683-2408

e-mail: sxiao@odu.edu

Summary

The project, “Near-Field Propagation of Sub-Nanosecond Electric Pulses into Amorphous Masses”, deals with the propagation of subnanosecond pulsed radiation in the near field region and its use in probing inhomogeneities in dielctrics. It also explores the possibility of changing the physical structure of lossy dielectrics by using very intense pulses. Our research effort has been focused on five research areas:

- Design and construction of a compact subnanosecond pulsed power generator
- Focusing of subnanosecond pulsed electric fields in the near field using prolate - spheroid wideband antennas
- Increase of the spatial resolution (reduction of the focal volume) using a dielectric lens in addition to the reflective antenna
- Target detection with focused subnanosecond radiations
- Modification of structure of biological targets with intense subnanosecond pulses

A Subnanosecond High Voltage Pulse Generator

A subnanosecond high voltage pulse generator was constructed, which is able to deliver 150 ps (FWHM) pulses with 100 ps risetime (10%-90%). The maximum voltage is 17 kV and the repetition rate is 20 Hz. This pulse generator uses a four-stage Marx-Bank to charge a peaking capacitor, which then discharges through a peaking switch into a transmission line [1-10]. As a result, a step voltage with a fast risetime followed by an exponential decay is generated. The step voltage is then cut off by a tail-cut switch to achieve the desired pulse durations. A photograph of the pulse generator is shown in Fig. 1a.

The fast rise and fall time of the pulses generated with this system is due to the fast voltage rise of the pulse generated by the Marx generator (6.6 kV/ns). Because of the high dV/dt, the voltage across the peaking switch (40 kV) reaches values of almost eight times the static breakdown voltage. The high overvoltage is the reason for the extremely fast breakdown in the temporal range of 100 ps. The tail-cut switch which is integrated into the coaxial cable in front of the load is similarly over-volted, leading to a fast cut-off of the pulse on a time scale of again 100 ps. The temporal development of the pulse is shown in Fig.1b.

Unlike most of the subanosecond switches, that are operated in gases (in hydrogen for example) at a pressure several times higher than atmospheric pressure, the spark gap switches in this pulse generator are operated in atmospheric pressure air. This allows for the construction of a simple and compact pulsed power generator (Fig. 1a).

In addition to this pulse generator a commercially available pulse generator which provided 200 ps pulses at an amplitude of up to 5 kV was used for the studies [FPG5-10PM, FID].

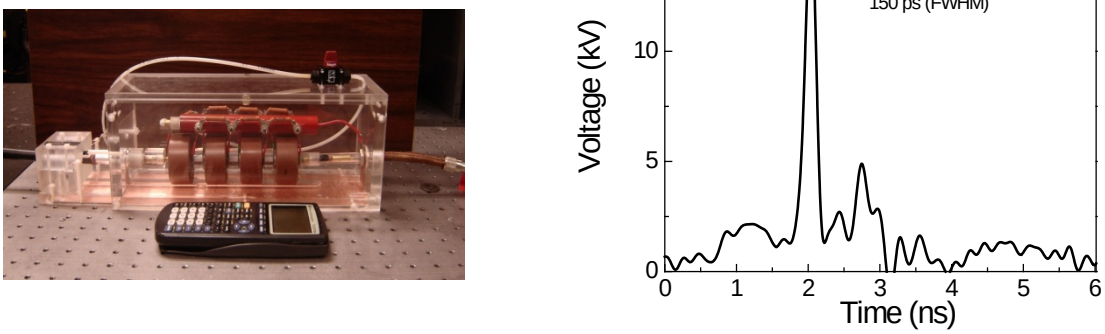

Fig.1. a) Photograph of the four-stage Marx generator including peaking switch. For size-comparison a calculator is shown; b) Temporal development of a 16 kV, 150 ps (FWHM) pulse across a 50 Ω load.

Focusing subnanosecond pulses in the near field

Focusing electromagnetic waves into soft matters were conducted using annular antenna arrays [11-17]. Narrow band signals were emitted from the array antennas and created a constructive interference at the desired focal point. Ultrawideband, pulsed signals were studied using delayed beam forming [18] and time-reversal technique [19-20]. These two techniques were limited to low power signals, which allow for high-accuracy temporal coordination among antennas. High power, narrowband reflector antennas for focusing in the near field were studied in [21-23]. The focusing cavity was even filled with low-loss dielectrics and metamaterial in order to achieve a better transmission from the antenna to the matter [24-27]. The high power, subnanosecond pulsed radiation was focused by means of a prolate-spheroidal impulse radiating antenna (IRA), which was developed by Carl Baum at the University of New Mexico [28-31], and built by Farr Research (Albuquerque, NM) (Fig.2). In this antenna, spherical waves emanate from the first focal point of the prolate-spheroidal reflector and propagate along two pairs of parallel, balanced conical transmission lines. The electromagnetic waves related to the subnanosecond pulse, that are scattered on the reflector surface and converge to the second focal point, are called “impulse”. Another part of the spherical waves which is propagating opposite to the impulse is called “prepulse” as it arrives at the second focus earlier than the impulse. The prepulse will not be focused and its amplitude decreases with distance.

The amplitudes of both prepulse and impulse are plotted in lateral and (longitudinal (axial) direction in Fig. 3 [32]. The power density of the impulse, which is proportional to the square of the electric field, is focused in both lateral and axial directions. The distribution of power density has a FWHM width of 32 cm in the axial direction and a FWHM width of 10 cm in the lateral direction (at z=16 cm).

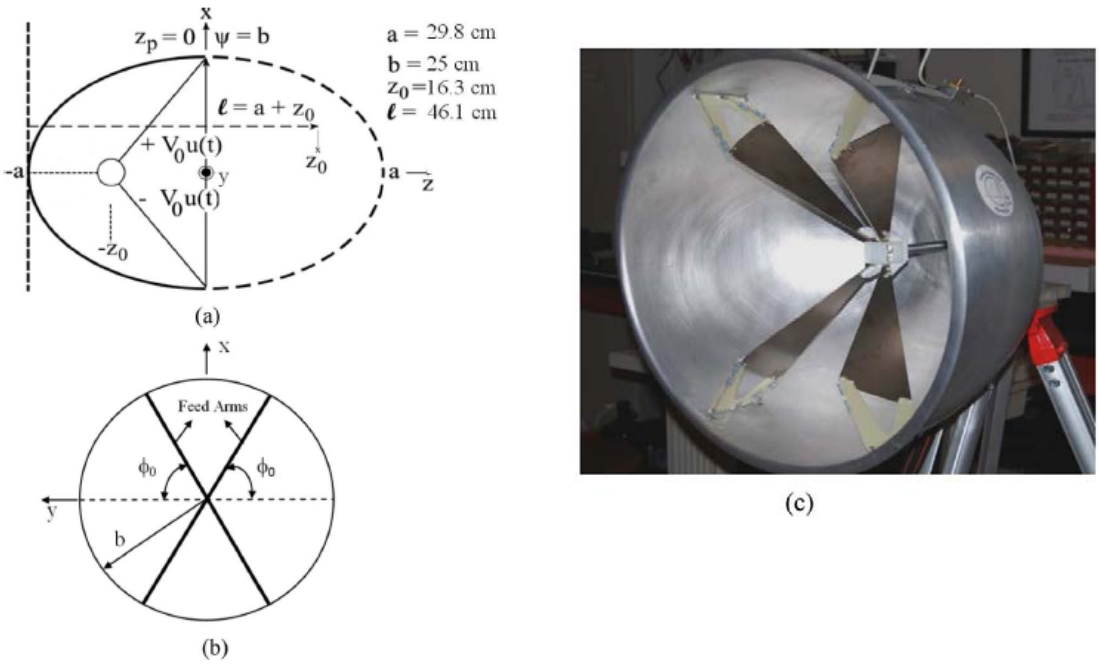

Fig.2. Antenna structure. (a) Side view. A differential signal is fed to the transmission line at the first focal point ($-z_0$). (b) Front view ϕ_0 is the angle between the feed-arm and y-axis. (c) The actual antenna.

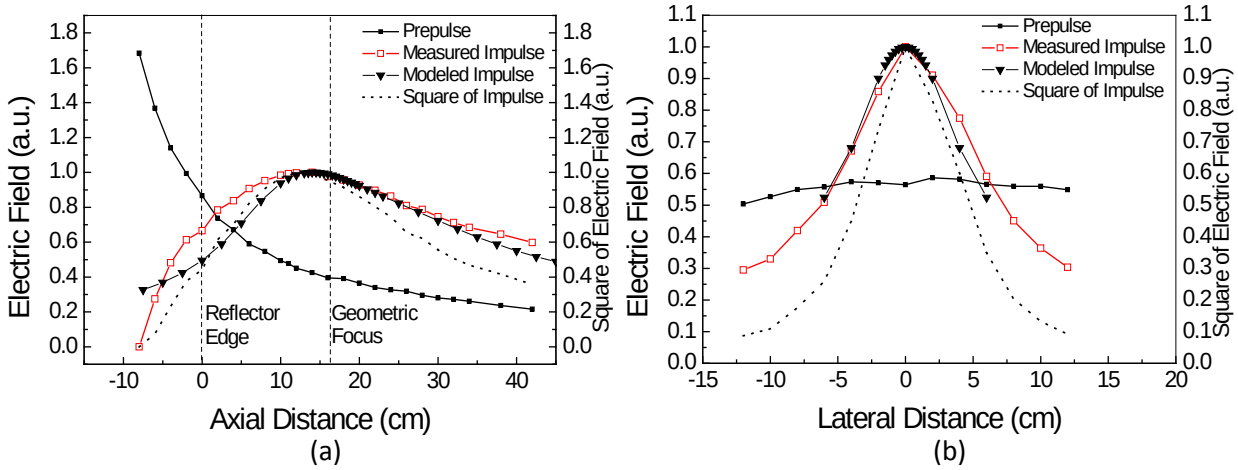

Fig.3. (a) Measured electric field (x-directed) distribution along the axis (z-axis). The prepulse, the impulse, and the square of impulse are shown. The curve with down-triangle symbols is the modeled impulse distribution along the z-axis. (b) The measured electric field (x-directed) distribution in the lateral direction (along the y-axis) at the focal plane. The prepulse, the impulse, and the square of impulse are shown. The curve with down-triangle symbols is the modeled impulse distribution in y-axis.

The electric field distribution of this antenna was modeled by using CST Microwave Studio, a 3-D, finite integral time domain (FITD), electromagnetic simulation software. The modeled results, for emission into free space agree very well with the experimental results. This holds especially near the focal point for both the axial and the lateral electric field distributions. Closer to the

reflector edge we observe a slight discrepancy between the modeled field and measured field, which could be due to the fact that the model only allows us to compute the x-directed field, but the sensor may pick up electric field components in y and z direction.

The spatial distribution of the electric fields in the near field of the focusing antenna were also modeled for dielectric media, other than in air. Because the radiation from the reflector antenna is composed of spherical waves converging to the second focus, a hemispherical shape was chosen for the dielectric with its center at the second focal point. In this case the phases of incident waves at the periphery of the hemisphere are equal. In the simulation, the dielectric hemisphere has a diameter of 12 cm and dielectric constant (ε_r) of 12. Different conductivity (σ) values, 0, 0.3 S/m and 0.5 S/m were assigned to the dielectric. A cylindrical base that has a dielectric constant of 35 and electric conductivity of 1S/m was added to the dielectric hemisphere to dampen the reflections from the boundary which is opposite to the antenna.

The modeling results show that the pulsed radiation is focused at the second focal point, which is at 6cm distance from the hemisphere surface (Fig.4a). Fig. 4b shows that the electric field at the second focus (distance = 6 cm) is 50 V/m for a ramp input of 1 V for a zero conductivity dielectric. It decreases to 20 V/m for a conductivity of 0.3 S/m. The intensity of the electric field is obviously strongly dependent on the medium conductivity: higher conductivity causing stronger attenuation in the pulse propagation path and consequently lower field intensity at the second focus.

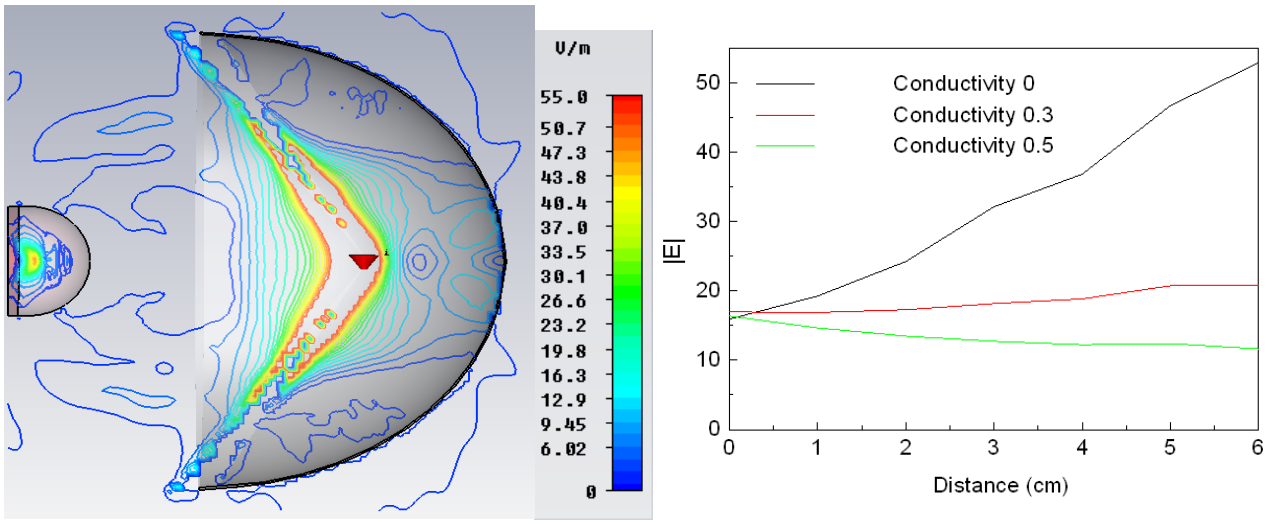

(a) (b)

Fig.4. (a) A 1 V ramp voltage with a risetime of 100 ps is launched and focused into a hemispherical target with diameter of 12 cm. The focal point is 6 cm from the sphere surface; b) The distribution of lateral electric fields in the axial direction (z-axis) for conductivities from 0-0.5 S/m.

The relatively poor matching condition on the air-dielectric interface causes intense reflection of the electromagnetic waves on the boundary, reducing the intensity of the transmitted wave even further. Therefore, it is important to place a matching layer with a permittivity between that of air and the dielectric on top of the hemispherical target (or any other target) in order to reduce the reflections at this interface.

Increasing the focusing resolution using a dielectric lens

The dielectric properties of the target medium and its surroundings determine to a large extend how effective the transfer of electromagnetic energy from the antenna into the target is. If the wave incident on the target is in air, but the target medium has a large relative permittivity (say, about 81 for water), then there will be a significant reflection of the pulse (80%). Adding a dielectric lens composed of well defined dielectric layers to the antenna allows a better matching, and consequently a higher electric field in the target. In addition it allows us to reduce the spot size, thereby increasing the field on the target even further (Fig.5).

The lens, which was designed by Carl Baum, is hemispherical [32-35] and the measurement in the lens dielectrics was discussed in [36-38]. Its focal point is in the geometric center of the hemisphere and overlaps the focus of the reflector antenna. The lens consists of five layers of dielectric materials with dielectric constants varying in an exponential profile from free space to the innermost layer ε_{rmax}. Due to the increase of the dielectric constant, the focal spot size can be reduced by a factor of $\varepsilon_{rmax}^{(-1/2)}$ at the innermost layer. The choice of the number of layers and their thickness is optimized to permit maximal transmission through these layers. The innermost layer is generally made of the same material as the medium to be probed. In this lens, the outermost layer has a dielectric constant of 1.3, and the innermost layer has a dielectric constant of 9. The spot size at the lens focus is approximately 1/3 of that in free space.

Fig.6a shows the increase in pulse amplitude right at the surface of the hemispherical lens, at the point z_0.: the ratio of the peak electric fields at this point compared to that without lens in air is 1.408[39]. Since the half-widths of the impulse responses in air and in the lens are not identical, the electric enhancement is given by the ratio of the integral of the curves, which can approximately expressed as A= (halfwidth)(peak amplitude)=FWHM*E_{max}. According to this calculation the electric enhancement is $A_{impulse\text{-}lens}/A_{impulse\text{-}air}\approx 2.11$. Fig. 6b compares the numerical simulation and experimental results of the beam width in air and in the lens. The beam width was reduced by a factor of two from 4.45 cm (no lens) to 2.04 cm (with lens).

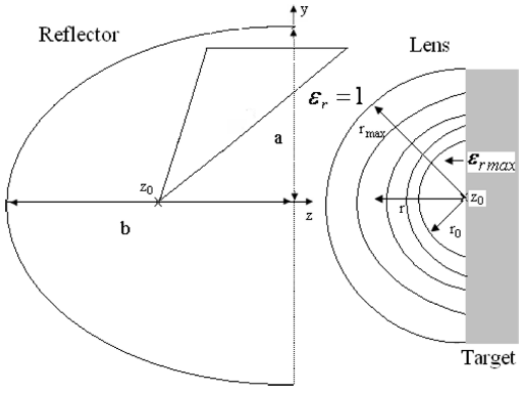

Fig.5. An impulse radiating antenna is used in combination with a dielectric lens which is located on the surface.

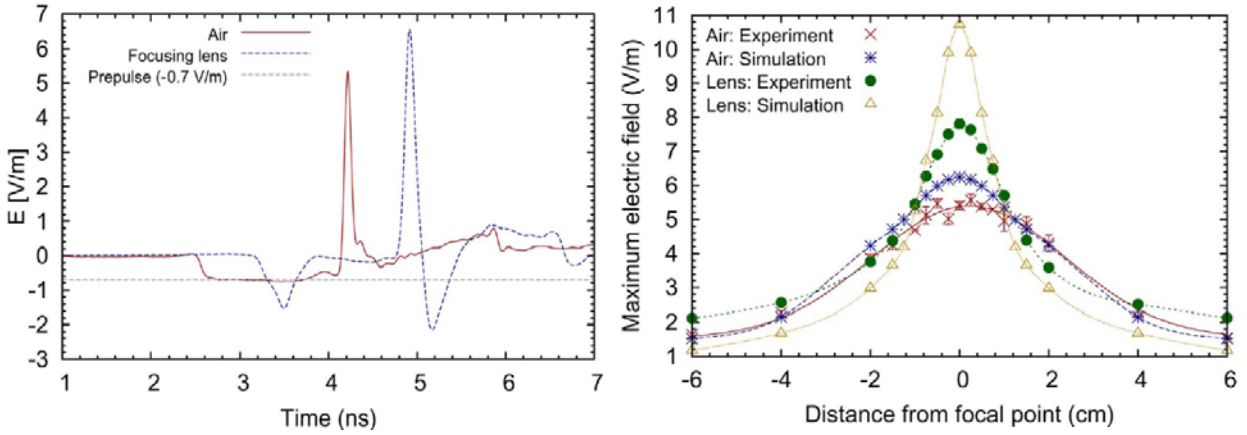

(a) (b)

Fig.6. a) Comparison of impulse waveforms, at the second focal point, in air and at the lens surface, at z_0; b) Comparison of simulation and experiment results of beam width with and without lens (at position z_0). The pulse risetime is ~100 ps.

Target Detection with Focused Subnanosecond Radiations

The antenna system as described above has been used to study the use of subnanosecond pulses to detect abnormalities in a homogeneous background. When the antenna's radiation is focused and the target at the focus is scanned, coherent backscattered signals, signals with the largest amplitude, can be recorded by the same antenna. The incoherent backscattered signals from the out-of-focus background clutter, are shifted in time and can be separated from the target signals. The technique is referred to as confocal imaging. The advantages of confocal imaging are increased signal-to-noise ratio and signal-to-clutter ratio and, therefore, improved target detection capability.

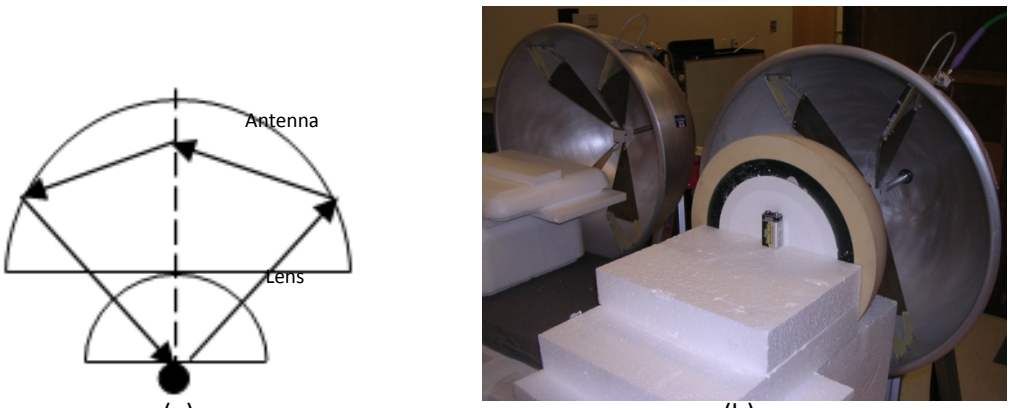

(a) (b)

Fig.7 (a) A focusing antenna in combination with a dielectric lens illuminates a target and the backscattering is collected with the same antenna. (b) The actual setup.

In the confocal imaging system, decreasing the focal spot size is important to increasing the resolution. One way to reduce the spot size is to use a dielectric lens in conjunction with the reflector antenna, as shown in Fig. 7. The lens is hemispherical. Its focal point is in the geometric center of the hemisphere and overlaps the focus of the reflector antenna. Therefore, the antenna, in combination with the lens, constitutes a confocal imaging system.

To determine the imaging resolution of the antenna-lens system, we have imaged two targets of equal dimensions 2.5X1.5X4.5cm^3 but with different spacing. The two objects are shifted from one edge at the surface of the lens to the other. This is equivalent to laterally scanning the two objects. In the experiment, the pulse risetime was 200 ps, which suggests a focal spot size of 4 cm, derived from the 100ps data shown in Fig.6b.

The background signals are subtracted from the signals obtained at each target location. The value of the difference is used to construct a 2-D image by assigning pixel values according to the magnitude of the signals received. Fig. 8 shows the image constructed with two objects with spacing of 3.5 and 5.5 cm [40]. The two targets are irresolvable in the lateral direction when the spacing is less than 3.5 cm. However, the imaging system was able to distinguish targets for a spacing of 5.5 cm. The resolution was therefore estimated to be approximately 4 cm.

Our present confocal system prevents a scanning of targets at various distances from the lens. The targets need to be placed close to the lens, within 2 cm of the focus, in order to provide return signals which can be distinguished from those obtained without lens. Scanning of targets at various depths may be possible if the probed object is placed within a hollowed-out lens.

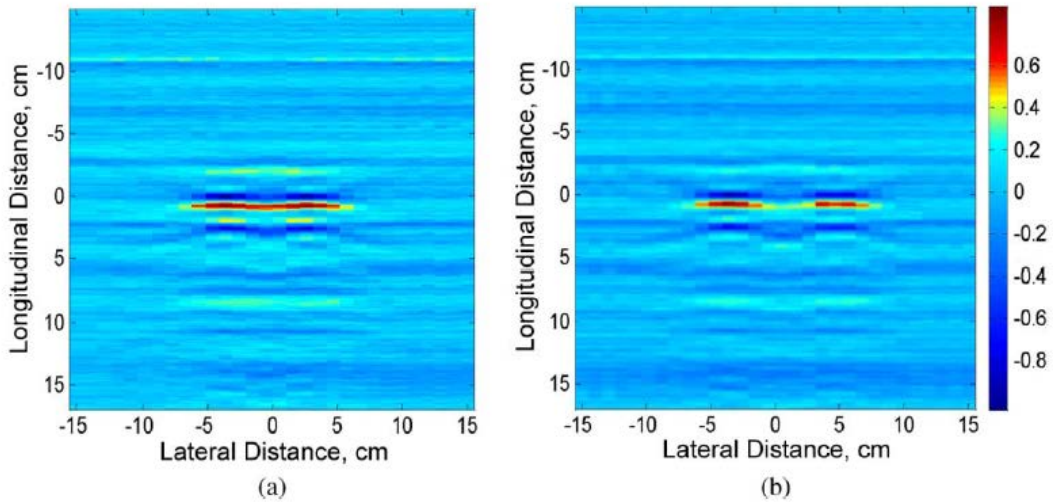

Fig.8. Images of two identical metallic objects that are separated by (a) 3.5 cm and (b) 5.5 cm. The two objects can be spatially resolved at a lateral spacing of 5.5 cm, but are irresolvable for 3.5 cm.

Modifying Target Physical Structure with Intense Subnanosecond Pulses

Focused subnanosecond pulsed radiation not only has the potential for detecting an inhomogeneity in a complex background, it also has the ability to modify structures of properties of targeted objects, such as biological cells, if the intensity of the pulses is sufficiently enhanced.

It is known that for pulses with durations shorter than the charging time of the outer membrane (~100 ns for mammalian cell), the probability of electric field acting upon intracellular structure increases. Shorter pulses in the subnanosecond range are consequently even more effective than nanosecond pulses in reaching intracelluar structures. However, this proposition should not create the impression that cell membrane will be exempt from the effect of subnanosecond pulses. We have found that, for the first time, cell membranes increase their conductance, in response to high power subnanosecond electric pulses (20 kV/cm, 200 ps).

Shown in Fig.9 are the voltage-current characteristics of a cell's membrane (NG108, Neuroblastoma Cell Lines) after it is exposed to subnanosecond pulses [41]. The IV curves were obtained by means of the patch clamp technology. The membrane currents were recorded by sweeping the voltages from -100 mV to 40 mV. At 10 and 30 seconds after exposure of 2000, 200 ps, 20 kV/cm pulses delivered at 10 Hz, the cell membrane becomes more permeable: it shows a higher leakage current compared with the cell that is not pulsed. The leakage current only flows in the inward direction from the extracellular to intracellular medium. The pathway of the current flow is most likely to be the small pores formed in the cell membranes, as is proved through other membrane integrity markers, Tl+ (atomic diameter: 0.34 nm) and Propidium+ ($1.38\times1.15\times0.54$ nm). These pores were estimated on the order of ~1.4 nm in diameter. Unexpectedly, the current rectifying characteristic of these pores is similar to synthetic nanopores in polymer foils, reportedly to be in asymmetrical conical shape [42].

Whereas causing cell membrane leakage requires 2000 pulses, we can also induce cell death by increasing the number of pulses with a high repetition rate (10 kHz in burst mode). We have observed that subnanosecond pulses caused cell death with a significant temperature rise due to a high-repetition rate and high pulse numbers. Cell viability assessed by WST assay 18 h after the exposure of 2.4 million pulses was found to be $34\% \pm 2\%$ with temperature rising to 42°C–45°C during exposure.

The cell death is due to both electric-field and thermal effects. Delivering pulses of higher electric field intensity at a lower repetition rate may allow us to separate these two effects, which justifies further study. On the other hand, subnanosecond pulses offer a potential treatment modality that can modify cell membrane properties or alter the physiological conditions of cells to induce a desired response instead of causing cell death. In this case, much lower numbers of pulses are needed to obtain this effect. Such applications can include enhancement of wound healing, or hemostasis (blood clotting), by stimulating calcium influx into platelets.

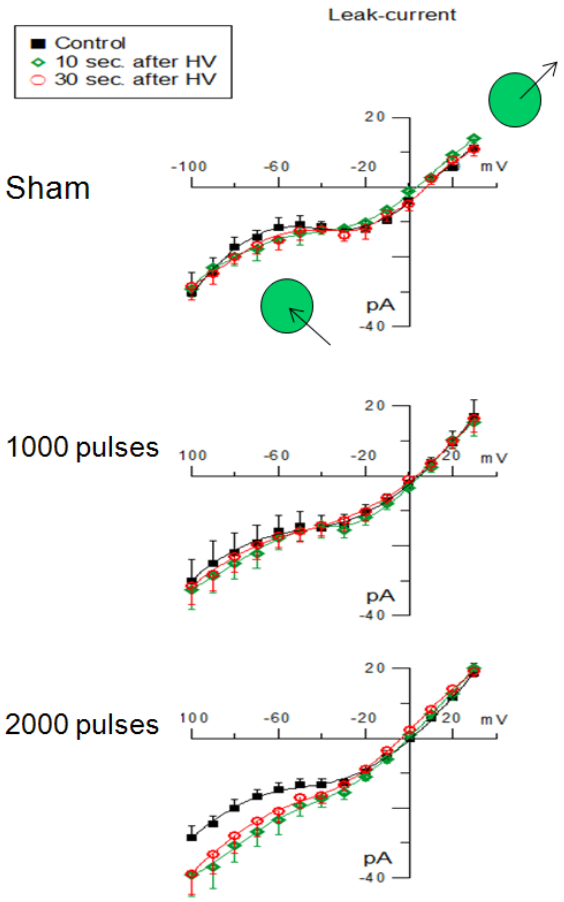

Fig.9. Current-voltage characteristics of a cell's membrane after being exposure to 200 ps, 20 kV/cm pulses. According to the convention in the patch clamp, the positive current flows outward from inside to outside cell (in the first quadrant). Conversely, the negative current flows inward (in the third quadrant) from outside to inside cell. After exposure of 2000 pulses, the cell shows leakage current increase in negative direction but no change in positive direction, which indicates inward "diodes" are produced in the cell membrane.

Future Work

Improving the spatial resolution for imaging targets and/or inducing physical changes in targets is possible but requires modifications of our system: The target and its surrounding dielectrics would need to be included into the imaging system as part of the lens. For inducing the change of dielectrics, a very high power wave launcher at the first focus needs to be constructed [43-44]. The material of the focusing lens has a tapered profile of dielectric constants in order to match the surrounding dielectrics. This lens will still be fed with the reflector antenna, but it would need to be hollowed out near the focus, by creating a hemispherical or spheroidal cavity (Fig.10). The dielectric medium surrounding the target would then be embedded into this cavity [45].

Using this technique, allows us to increase the solid angle through which the electromagnetic wave can approach the target through the lens. If the dielectric medium surrounding the target is pliant, it could then be sucked into this cavity by several small-diameter tubes drilled through the lens media to the lens/dielectrics interface. Transverse stretching will reduce the dispersion of the pulse as it approaches the target. This technique may be limited to not-too-deeply-buried targets. As one goes to deeply buried targets, one will need to increase the radius of the lens aperture to sufficiently large values compared to the depth. This will, in turn, increase the overall lens radius.

Our ultimate goal is to develop a useful delivery method of subnanosecond pulses that is able to deposit a substantial amount of energy or monitor a specific area at a specific depth inside a dielectric subject placed at the prolate spheroid reflector's focal point.

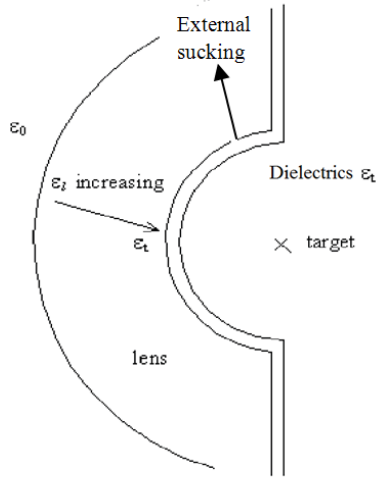

Fig.10. Embedding dielectric, hemispherical target such that it becomes part of the lens system allows us to increase the solid angle through which the electromagnetic wave can approach the target through the lens.

References

[1] J. M. Lehr, C. E. Baum and W. D. Prather, Fundamental Physical Considerations for Ultrafast Spark Gap Switching, SWN 28.

[2] C. E. Baum, W. L. Baker, W. d. Prather, J. M. Lehr, J. P. O'Loughlin, D. V. Giri, I. D. Smith, R. Altes, J. Fockler, D. Mclemore, M. D. Abdalla, and M. C. Sikpper, "JOLT: A Highly Directive, Very Intensive, Impulse-Like Radiator, " Proceedings of the IEEE, vol.92 (7), 2004.

[3] T. Heeren, J. T. Camp, J. F. Kolb, K. H. Schoenbach, S. Katsuki, and H. Akiyama, "250 kV Subnanosecond Pulse Generator with Adjustable Pulsewidth," IEEE Trans. Diel. Electr. Insul. vol. 14, pp. 884-888, 2007.

[4] W. Carey and J. Mayes, "Marx generator design and performance", in Power Modulator Symposium, 2002 and 2002 High-Voltage Workshop.Conference Record of the Twenty-Fifth International, pp. 625-628,2002.

[5] J. F. Francis, "High voltage pulse techniques", Pulsed Power Lecture Series, Plasma Laboratory, Texas Tech University, 1976.

[6] X. WANG, Y. HU, and X. SONG, "Gas discharge in a gas peaking switch," Laser and Particle Beams, 23, 553–558, 2005.

[7] Y. A. Andreev, V. P. Gubanov, A. M. Efremov, V. I. Koshelev, S. D. Korovin, B. M. Kovalchuk, V. V. Kremnev, V. V. Plisko, A. S. Stepchenko, K. N. Sukhushin, "High-power ultra wideband radiation source," Laser Part. Beams, 21, 211–217, 2003.

[8] C. A. Frost, T. H. Martin, P.E. Patterson, L. F. Rinehart, G. J. Rohwein, L.D.Roose, J. E. Aurand, "Ultrafast gas switching experiments," Proc. 9th IEEE Intern. Pulsed Power Conf. 491–494, 1993.

[9] G. M. Molen and M. S. Mazzola, "Breakdown mechanisms in a pulse-charged spark gap,"IEEE conference record of 1988, Power Modulator Symposium, Jun 20-22, p. 215-218, 1988.

[10] X. Cai, L. Wang, X. Zou, X. Wang and W. Jiang, "Overvolted breakdown and recovery of gas spark gap," Power Modulator and High Voltage Conference (IPMHVC), 2010 IEEE International, 23-27,p.541 - 544, May 2010.
[11] P. F. Turner, “Regional hyperthermia with an annular phased array,” IEEE Trans. Biomed. Eng. 31, 106–14, 1984.
[12] K. D. Paulsen, S. Geimer, J. Tang and W. E. Boyse, “Optimization of pelvic heating rate distributions with electromagnetic phased arrays,” Int. J. Hyperth. 15, 157–86, 1999.
[13] P. Wust, J. Nadobny, P. Deuflhard, G. Monich and R. Felix, “Simulation studies promote technological development of radiofrequency phased array hyperthermia,” Int. J. Hyperth, 2, 477–97, 1996.
[14] P. Wust, J. Nadobny, M. Seebass, D. Stalling, J. Gellermann, H. C. Hege, P. Deuflhard and R. Felix, “Influence of patient models and numerical methods on predicted power deposition patterns,” Int. J. Hyperth. 15 519–40, 1999.
[15] H. Kroeze, J. B. Van de Kramer, A. A. C De Leeuw and J. J. W. Lagendijk, “Regional hyperthermia applicator design using FDTD modeling,” Phys. Med. Biol. 46 1919–35, 2001.
[16] A.J. Fenn and G. A. King, “Experimental investigation of an adaptive feedback algorithm for hot spot reduction in radio-frequency phased-array hyperthermia,” IEEE Trans. Biomed. Eng. 43 273–80, 1996.
[17] M. M. Paulides, J. F. Bakker, E. Neufeld, J. Van der Zee, P. P. Jansen, P.C. Levendag and G. C. Van Rhoon , “The HYPERcollar: a novel applicator for hyperthermia in the head and neck,” Int. J. Hyperth. 23 567–76, 2007
[18] M. Converse, E. J. Bond, S. C. Hagness and B. D. Van Veen, “Ultrawide band microwave space-time beam forming for hyperthermia treatment of breast cancer: a computational feasibility study,” IEEE Trans. Microw. Theory Tech. 52 1876–89, 2004.
[19] B. Guo, L. Xu and J. Li, “Time reversal based microwave hyperthermia treatment of breast cancer, “ Microw. Opt.Tech. Lett. 47 335–8, 2005
[20] H. D. Trefna, J. Vrba and M. Persson, "Time-reversal focusing in microwave hyperthermia for deep-seated tumors," Phys. Med. Biol. 55, 2167-2185, 2010.
[21] K. Hirasawa, K. Fujimoto, T. Uchikura, S. Hirafuku, and H. Naito, “Power focusing characteristics of ellipsoidal reflector,” IEEE Trans.Antennas Propag., vol. AP-32, no. 10, pp. 1033–1039, Oct. 1984.
[22] R. C. Hansen, “Focal region characteristics of focused array antenna,” IEEE Trans. Antennas Propag., vol. AP-33, no. 12, pp. 1328–1337, Dec. 1985.
[23] J. W. Sherman, III, “Properties of focused apertures in the Fresnel region,” IRE Trans. Antennas Propag., vol. AP-10, no. 4, pp. 399–408, Jul. 1962.
[24] I.S. Karanasiou, K. T. Karathanasis KT, A. Garetsos, U. K. Uzunoglu. “Development and laboratory testing of a noninvasive intracranial focused hyperthermia system.” IEEE Trans Microw Theory Techniques 56:2160–2171. 2008.
[25] I.A. Gouzouasis, I.S. Karanasiou, N.K. Uzunoglu, “Exploring the enhancement of the imaging properties of a microwave radiometry system for possible functional imaging using a realistic human head model,” J Instr 4:P06006, 2009b.
[26] K. T. Karathanasis, I.S. Karanasiou, N.K. Uzunoglu, “Enhancing the focusing properties of a prototype non-invasive brain hyperthermia system: A simulation study. Proceedings of the 29th IEEE Engineering in Medicine and Biology Society, pp. 218–221, 2007a.
[27] I. A. Gouzouasis, K. T. Karathanasis, I. S. Karanasiou, and N. K. Uzunoglu, "Contactless passive diagnosis for brain intracranial applications:a study using dielectric matching materials," Bioelectromagnetics 31:335-349, 2010.
[28] C. E. Baum, E. G. Farr, and D. V. Giri, “Review of impulse-radiating antennas,” in Review of Radio Science 1996–1999,W. S. Stone, Ed. Oxford, U.K.: Oxford Univ. Press, 1999, ch. 12.

[29] C. E. Baum, “Focal waveform of a prolate-spheroidal impulse-radiating antenna (IRA),” Radio Sci., vol. 42, 2007, RS6S27, DOI: 10.1029/2006RS003556.
[30] S. Altunc, C. E. Baum, C. G. Christodoulou, E. Schamiloglu, and C. J. Buchenauer, “Focal waveforms for various source waveforms driving a prolate-spheroidal impulse radiating antenna (IRA),” Radio Sci., vol.43, 2008, RS4S13, DOI: 10.1029/2007RS003775.
[31] S. Altunc, “Focal waveform of a prolate-spheroidal impulse radiating antenna (IRA),” Ph.D. dissertation, Dept. Elect. Comput. Eng., Univ. New Mexico, Albuquerque, NM, 2007.
[32] S. Xiao, S. Altunc, P. Kumar, C. E. Baum, and K. H. Schoenbach, “A Reflector Antenna for Focusing in the Near Field,” IEEE Antennas and Wireless Propagation Letters, Vol. 9, 12-15, 2010.
[33] C. E. Baum, “Addition of a lens before the second focus of a prolatespheroidal IRA,” in Sens. Simulation, Apr. 2006, Note 512.
[34] C. E. Baum, S. Altunc, and P. Kumar, “Scaling relationships for electromagnetic parameters for focusing graded dielectric lenses,” in Sens. Simulation, Apr. 2009, Note 537.
[35] S. Altunc, C. E. Baum, C. G. Christodoulou, E. Schamiloglu, and C. J. Buchenauer, “Design of a special dielectric lens for concentrating a subnanosecond electromagnetic pulse on a biological target,” IEEE Trans. Dielectr. Electr. Insul., vol. 16, no. 5, pp. 1364–1375, Oct. 2009.
[36] P.Kumar, S. Altunc, C. E. Baum, C. G. Christodoulou, E. Schamiloglu, and C. J. Buchenauer, “Radially inhomogeneous spherical dielectric lens for matching 100 ps pulses into biological targets,” IEEE Trans.Plasma Sci. (Special Issue) vol. 38, no. 8, pp. 1915–1927, Aug. 2010.
[37] C. E. Baum, “Accuracy considerations in the design of B-Dot and I-Dot sensors,” in Sens. Simulation, Jun. 1992, Note 344.
[38] C. E. Baum, “Tiny fast-pulse B-Dot and D-Dot sensors in dielectric media,” in Sens. Simulation, Jun. 2009, Note 544.
[39] P. Kumar, C. E. Baum, S. Altunc, J. Buchenauer, S. Xiao, C. G. Christodoulou,E. Schamiloglu, and K. H. Schoenbach, "A Hyperband Antenna to Launch and Focus Fast High-Voltage Pulses Onto Biological Targets," IEEE Trans. Microwave Theory and Techniques, Vol.59, No. 4, 2011.
[40] C. Bajracharya, S. Xiao, C.E. Baum, and K. H. Schoenbach, "Target Detection with Impulse Radiating Antenna," IEEE Antennas and Wireless Propagation Letters, Vol.10, 2011.
[41] S. Xiao, S. Guo, V. Nesin, R. Heller and K. H. Schoenbach, “Subnanosecond Electric Pulses Cause Membrane Permeabilization and Cell Death,” IEEE Trans. Biomedical Engineering, Vol. 58, No. 5, 2011.
[42] Z. Siwy, Y. Gu, H.A. Spohr, D. Baur, A. Wolf-Reber, R. Spohr, P. Apel and Y. E. Korchev, “Rectification and voltage gating of ion currents in a nanofabricated pore,” Europhys. Lett., 60(3), 349-355, 2002.
[43] S. Altunc, C. E. Baum, C. G. Christodoulou, and E. Schamiloglu, “Analytical calculations of a lens for launching a spherical TEM wave,” in Sens. Simulation, Oct. 2008, Note 534.
[44] P. Kumar, S. Altunc, C. E. Baum, C. G. Christodoulou, and E. Schamiloglu, “Design considerations for a cylindrical pressure vessel with a spherical launching lens,” in EM Implosion, Mar. 2010, Memo 41.
[45] C. E. Baum, S. Altunc, K. H. Schoenbach, and S. Xiao, “Focusing an electromagnetic implosion inside tissue,” in Bioelectric, Oct. 2008, Note 3.

Achievements

Journal Publications:

S. Xiao, S. Altunc, P. Kumar, C. E. Baum, and K. H. Schoenbach, “A Reflector Antenna for Focusing in the Near Field,” IEEE Antennas and Wireless Propagation Letters, Vol. 9, 12-15, 2010.

C. Bajracharya, S. Xiao, C.E. Baum, and K. H. Schoenbach, "Target Detection with Impulse Radiating Antenna," IEEE Antennas and Wireless Propagation Letters, Vol.10, 2011.

S. Xiao, S. Guo, V. Nesin, R. Heller and K. H. Schoenbach, “Subnanosecond Electric Pulses Cause Membrane Permeabilization and Cell Death,” IEEE Trans. Biomedical Engineering, Vol. 58, No. 5, 2011.

P. Kumar, C. E. Baum, S. Altunc, J. Buchenauer, S. Xiao, C. G. Christodoulou,E. Schamiloglu, and K. H. Schoenbach, "A Hyperband Antenna to Launch and Focus Fast High-Voltage Pulses Onto Biological Targets," IEEE Trans. Microwave Theory and Techniques, Vol.59, No. 4, 2011.

K. H. Schoenbach, S. Xiao, R. P. Joshi, J. T. Camp, T. Heeren, J. F. Kolb, and S. J. Beebe, “The Effect of Intense Subnanosecond Electrical Pulses on Biological Cells,” IEEE Trans. Plasma Science, Vol. 36, No. 2, 2008.

Manuscript

J. T. Camp, Y. Jing, J. Zhuang, J. Kolb, S. J. Beebe, J. Song, R. P. Joshi, S. Xiao, and K. H. Schoenbach, “Cell Death Induced by Subnanosecond Pulsed Electric Fields at Elevated Temperatures,” submitted

Conference Proceedings:

S. Xiao, K. H. Schoenbach and C. E. Baum, “Time-Domain Focusing Radar for Medical Imaging,” XXIX General Assembly of URSI, Chicago, IL, August, 2008.

S. Xiao, K. H. Schoenbach and C. E. Baum, “Focusing Pulsed Electromagnetic Radiation for Therapy and Imaging,” IFMBE Proceedings, World Congress on Medical Physics and Biomedical Engineering, Munich, Germany, September, 2009.

K. H. Schoenbach, S. Xiao, J.T. Camp, M. Migliaccio, S.J. Beebe, and C. E. Baum, “Wideband, High-Amplitude, Pulsed Antennas for Medical Therapies and Medical Imaging,” Proc. 2009 International Conference on Electromagnetics and Advanced Applications (ICEAA’09), Torino, Italy, ISBN: 978-1-4244-3386-5, session 20, September, 2009.

S. Xiao, M. Migliaccio, J. T. Camp, C. E. Baum, and K. H. Schoenbach, “Focusing Pulsed Electromagnetic Radiation in the Near Field,” 2009 IEEE Pulsed Power Conference Proceedings, p. 495, Washington DC, June, 2009.

S. Xiao, C. Bajracharya, C. E. Baum, and K. H. Schoenbach, “Imaging with Focused Pulsed Electromagnetic Radiation,” Digest of Technical Papers, 2009 IEEE Pulsed Power Conference Proceedings, p. 872, Washington DC, June, 2009.

J. T. Camp, S. Xiao, S. Beebe, P. F. Blackmore, and K. H. Schoenbach, “Bioelectric Studies with Subnanosecond Pulsed Electric Fields,” 2009 IEEE Pulsed Power Conference Proceedings, p. 876, Washington DC, June, 2009.

Conference Presentations

S. Xiao and K. H. Schoenbach, “Modifying Cell Functions with Ultrashort Pulses,” USNC-URSI National Radio Science Meeting, Boulder, Co, January, 2010.

(Invited) S. Xiao, T. Camp, N. Vasyl, A. Pakhomov, R. Heller, and K. Schoenbach, “Biological Cells Response to High Power Electromagnetic Pulses,” IEEE International Power Modulator and High Voltage Conference, Atlanta, GA, May, 2010.

J. T. Camp, S. Xiao, W. Baldwin, K. Schoenbach, “Effects of the Rate of Temperature Increase on Liver Cancer Cells In Vitro,” IEEE International Power Modulator and High Voltage Conference, Atlanta, GA, May, 2010.

S. Xiao, J. T. Camp, Y. Jing and K. H. Schoenbach, “The Effect of the Rate of Temperature Rise on Cell Survival,” 18th IEEE International Pulsed Power Conference, Chicago, IL, June, 2011.

S. Xiao, Y. H. Sun and K. H. Schoenbach, “A Wideband Exposure System for In-Vitro Study,” 18th IEEE International Pulsed Power Conference, Chicago, IL, June, 2011.

M.S. Thesis

Mark Migliaccio, “Focusing EM Radiation in Dielectric Medium,” (M.S., ODU, 2009)

Ph.D. Thesis

Thomas Camp, “Cell Death Induced by Subnanosecond Pulsed Electric Fields” (to be graduated in 2012)

Chandra Bajracharya, “Near Field Impulse Radiating Antenna Characterization,” (to be graduated in 2012)

A Reflector Antenna for Focusing Subnanosecond Pulses in the Near Field

Shu Xiao, *Member, IEEE*, Serhat Altunc, *Member, IEEE*, Prashanth Kumar, Carl E. Baum, *Life Fellow, IEEE*, and Karl H. Schoenbach, *Fellow, IEEE*

***Abstract*—A prolate-spheroidal reflector antenna focusing subnanosecond pulsed electromagnetic radiation in the near field is studied. This antenna reflector is fed by a pair of balanced, conical-plate transmission lines and the radiated pulse consists of a prepulse, an impulse, and a postpulse. Whereas the prepulse amplitude decreases inversely with distance, the impulse is maximum near the geometric focus, and its power density distribution has a full-width at half-maximum (FWHM) width of 32 cm in the axial direction and 10 cm in the lateral direction.**

***Index Terms*—Focusing, impulse radiating antennas (IRAs), near field, prolate spheroidal reflector, subnanosecond pulse.**

I. Introduction

RESEARCH on the near-field radiation of subnanosecond electric pulses is motivated by the possible use of subnanosecond pulsed antennas for medical therapies and dielectric imaging. Biological cells exposed to the subnanosecond electric pulses have shown increased lethality and increased calcium release, which may lead to medical therapies, such as cancer treatment or wound healing [1]. At lower intensity, antennas fed with subnanosecond pulses can be used to explore the electrical properties of biological tissues in the near-field region, allowing us to obtain the dielectric profile of the tissue under observation and to detect abnormalities in a uniform background due to the dielectric contrast [2], [3]. Both imaging and medical application require focusing the radiation to a minimum spot size. In imaging, a small spot size allows for a 3-D scan with a good spatial resolution. For therapy, a small spot size means that only the area at the focal point will be treated as opposed to the surrounding area with lower electric field (or power density).

The antennas for radiating and focusing ultrawideband, high-power signals with low dispersion and high directivity can be reflector-type antennas, lenses or antenna arrays. For reflector-type antennas, an ellipsoidal dish is usually used. The dish has two focal points with a source placed at the first focal point and the target placed at the second focal point. In research on microwave-induced hyperthermia, an ellipsoidal reflector for focusing a narrowband signal was used [4]. For high-power ultrawideband radiation in the time domain, studies were mostly focused on long-range, far-field impulse radiating antennas (IRAs), in which a paraboloidal dish with a second focus at infinity is employed [5]. For the second focal point close to the near-field region with focal distance less than $2\mathrm{D}^2/\lambda$ (D: the aperture diameter; λ: the wavelength), the spot size is reduced, and the spot width W is approximately proportional to the focal distance (r_0) : $\mathrm{W} = \mathrm{r}_0\lambda/\mathrm{D}$, which indicates that a large aperture for a short focal distance permits a small focus [6], [7]. Recently, a series of studies, using the prolate spheroidal reflectors in conjunction with the typical TEM feed-arms used in long-range IRA, have shown focusing of a radiated impulse in the near field [8], [9]. As reported in [8] and [9], the antenna had a 1-m aperture diameter with a quarter of the prolate spheroid as a reflector. The reflector was installed on a ground plane and an unbalanced feed structure was used.

In this letter, we report a smaller version of a prolate spheroidal IRA (PSIRA) with an aperture diameter (0.5 m) designed for near-field imaging or for therapeutic applications. Whereas the previously reported PSIRA was primarily studied for the proof of concept, this PSIRA was designed a step closer to the actual applications, which require the antenna to be compact and portable. To our knowledge, this is the first IRA with a balanced feed configuration, which focuses the impulse in the near field. This antenna uses half of the prolate spheroid as the reflector. The antenna structure was scaled down by a factor of 0.5 from the suggested PSIRA dimensions [8]. It was manufactured by Farr Research, Albuquerque, NM. We have measured the electric field distribution of this antenna with an approximate Gaussian input of half-width 200 ps.

II. Antenna Structure

The antenna consists of three parts: a prolate spheroidal reflector, a conical feed structure, and a balun (Fig. 1). The semimajor axis of the reflector, $\mathrm{a} = 29.8$ cm, and the semiminor axis $\mathrm{b} = 25$ cm. The focal distance z_0 is 16.3 cm. The conical feed has two pairs of parallel, balanced conical plates as a transmission line, each arranged at an angle of 60° with respect to the y-axis (ϕ_0), resulting in an impedance of 200 Ω. A balun, made of two 100-Ω cables, allows a 1:4 ratio impedance transformation from the pulse input (50 Ω from the pulse source) to the conical transmission line (200 Ω). The balun has the advantage of doubling the voltage at the input terminal of the transmission line. The field at the focal point, with our feed-arms at 60°, is amplified by 1.6 compared to one pair of conical feed-arms [9].

Manuscript received November 25, 2009. Date of publication January 22, 2010; date of current version March 05, 2010. This work was supported by the US Air Force of Scientific Research (AFOSR) and Bioelectrics Inc.

S. Xiao is with the Department of Electrical and Computer Engineering, Old Dominion University, Norfolk, VA 23508 USA (e-mail: sxiao@odu.edu).

S. Altunc, P. Kumar, and C. E. Baum are with the Department of Electrical and Computer Engineering, University of New Mexico, Albuquerque, NM 87131 USA (e-mail: cebaum@ece.unm.edu).

K. H. Schoenbach is with the Frank Reidy Research Center for Bioelectrics, Old Dominion University, Norfolk, VA 23508 USA (e-mail: kschoenb@odu.edu).

Color versions of one or more of the figures in this letter are available online at http://ieeexplore.ieee.org.

Digital Object Identifier 10.1109/LAWP.2010.2041027

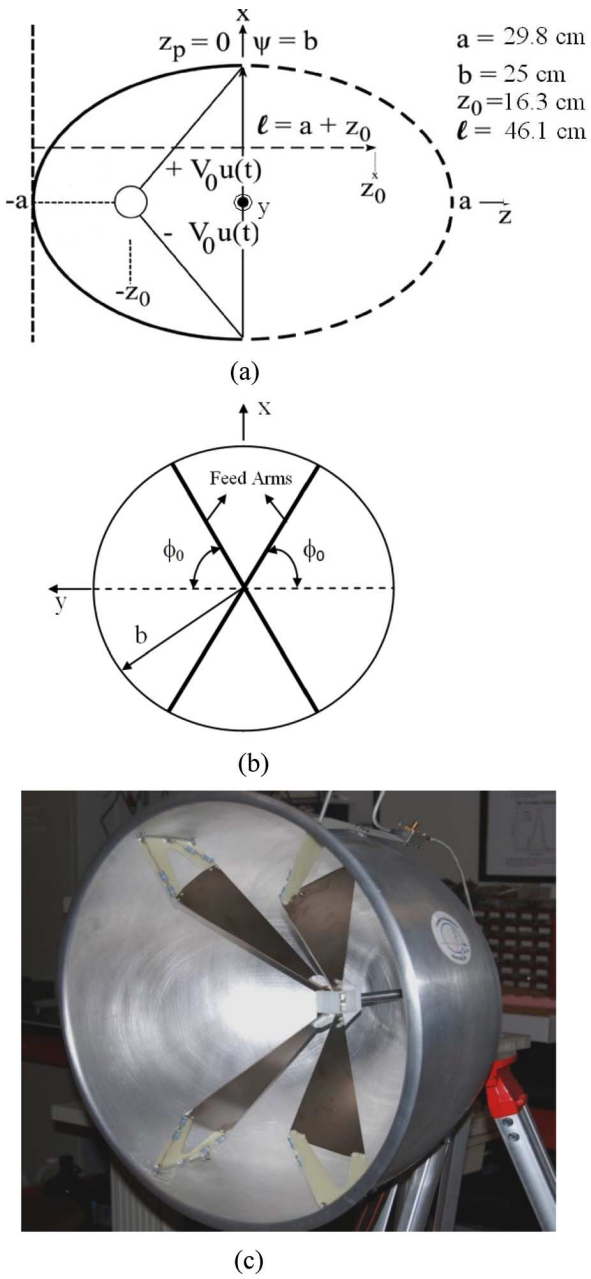

Fig. 1. Antenna structure. (a) Side view. A differential signal is fed to the transmission line at the first focal point $(-z_0)$. (b) Front view. ϕ_0 is the angle between the feed-arm and y-axis. (c) The actual antenna.

The waves scattered on the reflector surface become an exact inhomogeneous spherical TEM wave propagating toward the second focus. At the end of the conical feed plate, resistors were placed to absorb the low-frequency component of the signals.

III. Electric Field at the Focal Point

The electric field at the second focal point comprises three components: the prepulse, the impulse, and the postpulse. The prepulse $(\mathrm{E_p})$ is radiated directly from the conical transmission line, and the impulse is the electromagnetic pulse reflected from the prolate-spheroidal reflector. Only the impulse will be focused at the second focal point coherently as the reflected wave on the surface will arrive at the second focal point in the same phase.

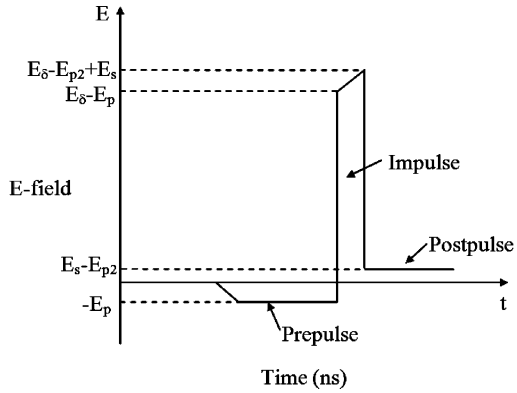

Fig. 2. The schematics of the analytical pulse shape at the focus when the antenna is fed with a step-function pulse.

Shown in Fig. 2 is the analytical focal waveform expected at the focus for a fast-rising step function feeding the antenna. The impulse part primarily contains E_δ, subtracted by $\mathrm{E_p}$. E_δ is proportional to the time derivative of the feed pulse: A faster rise-time pulse produces a higher amplitude. The prepulse, $\mathrm{E_p}$, is proportional to the amplitude of the feed pulse. The step impulse, $\mathrm{E_s}$, from the conical transmission in the opposite direction to $\mathrm{E_p}$, is reflected on the reflector and also contributes to the impulse. $\mathrm{E_s}$ and E_δ are in the same direction. $\mathrm{E_p}$ is valid until the wave travels to the truncation of the reflector along the conical transmission line. After that, $\mathrm{E_p}$ becomes a new term, $\mathrm{E_{p2}}$. The analytical analysis of these terms can be seen in [9]. In the impulse, we are interested in the dominant part, E_δ. For a given step-input, the x-axis-directed (lateral) components of the prepulse and the impulse at the geometric focus ($z_0 = 16$ cm) were calculated by integrating the fields of the reflected TEM wave over the truncated aperture plane [8]

$$\mathrm{E_p} \cong 1.6[\mathrm{V(t)}/(2\pi \mathrm{f_g})][(\mathrm{a}+\mathrm{z_0})/(\mathrm{bz_0})] \quad (1)$$

$$\mathrm{E}_\delta \cong (1.6/\mathrm{c})[\mathrm{dV(t)/dt}][(\mathrm{b/a})/(\pi \mathrm{f_g})]. \quad (2)$$

$\mathrm{V(t)}$ is the voltage of the feeding pulse, c is the speed of light, and $\mathrm{f_g}$ is the characteristic impedance factor of the conical feed-arms. It is noted that electric fields are multiplied by a factor of 1.6 for the antenna with four-feed arms at 60°. For the impulse part, the duration of the impulse is t_δ, and the field amplitude of the impulse is proportional to $\mathrm{V_0 t_\delta^{-1}}$ (V/m) for a step function with an amplitude of $\mathrm{V_0}$ and a rise time of t_δ.

From (2), it is clear that in order to produce a large field at the focal point, a large voltage-time derivative and a low launching impedance of the conical transmission line (low $\mathrm{f_g}$) are required. The pulse rise time should be short in order to increase the amplitude of the impulse.

The impulse and the prepulse have opposite signs, with the impulse being much larger than the prepulse (Fig. 2). The ratio of the impulse to the prepulse is $\mathrm{z_0}$ T/a, in which T satisfies $\mathrm{T} = 2[\mathrm{a} - \mathrm{z_0}]/\mathrm{ct}_\delta$. This ratio suggests that in order to obtain a large impulse, $\mathrm{z_0/a}$ needs to be large. A "fat" and shallow antenna should produce a larger impulse amplitude at the focus.

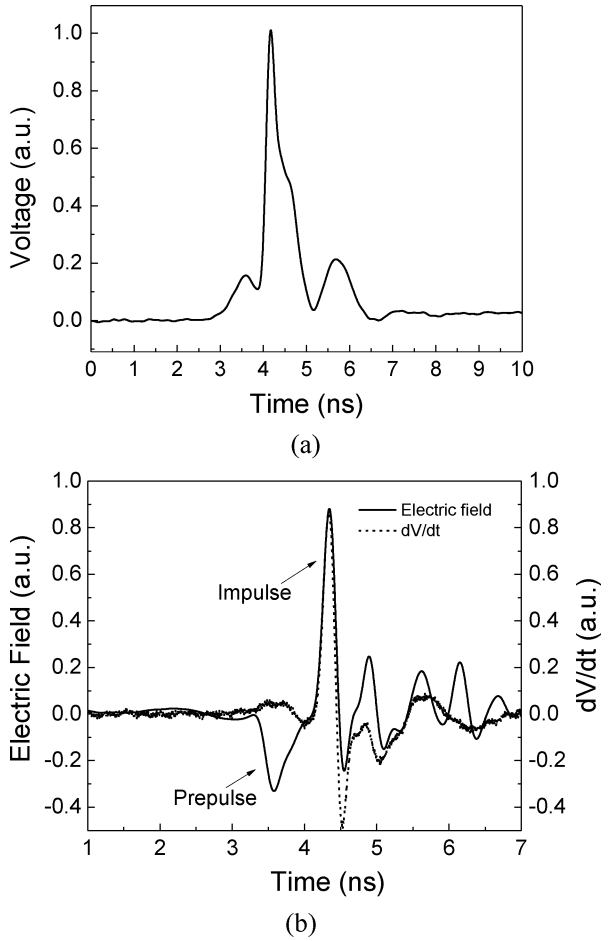

Fig. 3. (a) The measured electric pulse from the pulse generator that was fed into the antenna. (b) The measured electric field at the second focal point (solid line). The dash line is dV/dt, and V is the feed pulse shown in (a). The peak of dV/dt was normalized to the impulse amplitude.

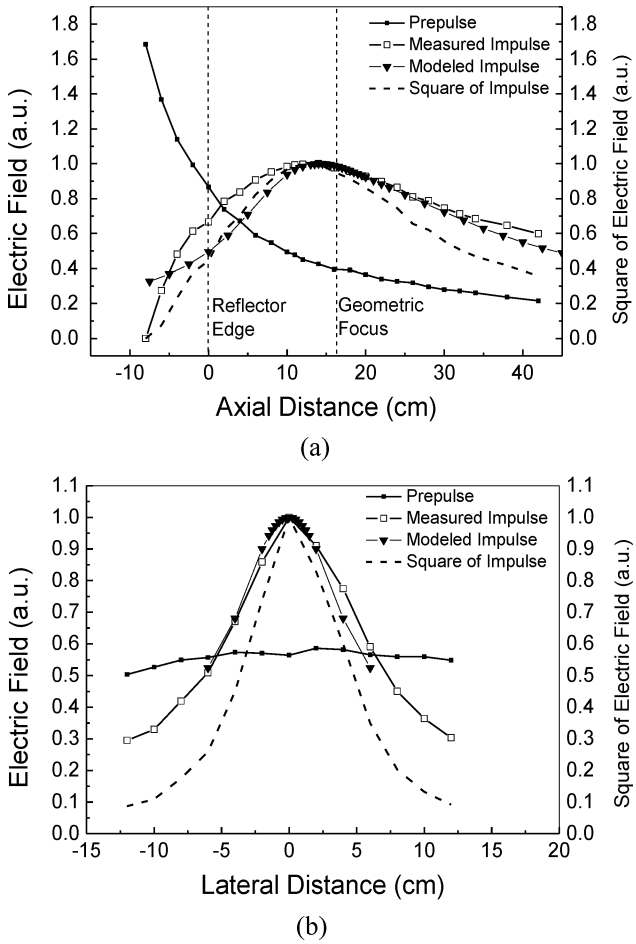

Fig. 4. (a) The measured electric field (x-directed) distribution in the axial direction (z-axis). The prepulse, the impulse, and the square of impulse are shown. The curve with down-triangle symbols is the modeled impulse distribution in z-axis. (b) The measured electric field (x-directed) distribution in the lateral direction (y-axis). The prepulse, the impulse, and the square of impulse are shown. The curve with down-triangle symbols is the modeled impulse distribution in y-axis.

IV. Electric Field Distribution

To measure the distribution of the electric field at and around the focal point of the PSIRA, we used a TEM horn antenna with two tapered, curved plates, which has the same polarization as the PSIRA and measures the x-directed electric field. The antenna has an opening distance of 4 cm. It was facing toward the prolate spheroidal antenna aperture. The antenna was moved along the z-axis to measure the longitudinal electric field distribution. Fig. 3(a) shows the input pulse, generated by a subnanosecond pulse generator (FPG5-10PM, manufactured by FID). As the sensor measures the time rate change of electric displacement field [10], the measured signal was integrated in time to obtain the electric field [Fig. 3(b)].

In Fig. 3(b), the prepulse is wider than the impulse since the prepulse is just the replica of the input pulse and the impulse is proportional to the time derivative of the feed pulse shown in Fig. 3(a). The feed pulse, which was directly measured from the pulse generator, was differentiated to obtain dV/dt [dashed line in Fig. 3(b)]. Apparently, the impulse part of the electric field is overlapped with dV/dt, which confirms the prediction of (2). The difference of frequency components of prepulse and impulse allows us to use a high-pass filter to suppress the prepulse and enhance the impulse in future applications, such as in a near-field radar. The separation in time between these two pulses, defined as cleartime, is approximately 1 ns. The postpulse after $t = 4.5$ ns may contain both diffractions from various parts of the antenna (reflector rim, edge of the conical plate, etc.) and the resonance signal of the sensor itself.

The amplitudes of both prepulse and impulse are plotted in y- and z-axes in Fig. 4. The prepulse decreases in the z-direction, with a $1/z$ dependence. For an observation point at $z = 16$ cm, the geometric focus, the prepulse stays approximately constant along the y-axis ($y = -12$ to 12 cm), indicating again that it scales as $1/z$. The power density of the impulse, which is proportional to the square of the electric field, is focused in both lateral and axial directions. The distribution of power density has a full-width at half-maximum (FWHM) width of 32 cm in the axial direction and a FWHM width of 10 cm in the lateral direction (at $z = 16$ cm).

The electric field distribution of this antenna was also modeled by CST Microwave Studio, a 3-D, finite integral time domain (FITD) electromagnetic simulation software. The input excitation is a Gaussian waveform with a half-width of 200 ps to closely model the experimental input waveform. The modeled

distributions of the impulse in the axial direction and the lateral direction are plotted in Fig. 4(a) and (b), respectively. The modeled results agree very well with the experimental results. This is true especially near the focal point in both the axial and the lateral electric field distributions. At an observing distance closer to the reflector edge, we observe a slight discrepancy between the modeled field and measured field, which could be due to the fact that the sensor may pick up other electric field components besides the x-directed field and the model only gives the x-directed field.

We also note that the maximum of the impulse electric field on the axis is shifted slightly from the geometric focus ($z = 16$ cm) toward the reflector, which is observed in both the measured result and the modeled result. This is because the impulse decreases inversely with the distance while it is focused in space. At the focal point, even though we have a coherent combination of waves, the impulse electric field is still smaller than the nearby locations toward the reflector due to a large impulse width, ct_δ (in spatial units). In order that the maximum impulse amplitude occurs at the geometric focus, the impulse width needs to be small compared to both $2z_0$ and 2b (similar discussion in the frequency domain can be seen in [7]). A pulse with faster rise time should allow the shift of the focal spot towards the geometric focus.

V. Conclusion and Future Work

The PSIRA with a reflector diameter of 0.5 m focuses the subnanosecond electric pulse radiation near the second focal point ($z = 16$ cm). The focus spot has an ellipsoidal shape, and the distribution of power density has a small diameter in the lateral direction and a wide dimension in the axial direction (10 and 32 cm in FWHM). The measured electric field distribution agrees with the modeled results to a large extent. Near the focal point, the measured electric field is exactly as the model predicts. When the focusing antenna is used for the delivery of short pulses into targets in the near field, a focusing dielectric lens near the second focal point may be used to minimize the spot size and increase the impulse amplitude [11].

References

[1] K. H. Schoenbach, S. Xiao, R. P. Joshi, J. T. Camp, T. Heeren, J. F. Kolb, and S. J. Beebe, "The effect of intense subnanosecond electrical pulses on biological cells," *IEEE Trans. Plasma Sci.*, vol. 36, no. 2, pt. 1, pp. 414–422, Apr. 2008.

[2] J. A. Rogers, "The dielectric properties of normal and tumour mouse tissue between 50 MHz and 10 GHz," *Brit. J. Radiol.*, vol. 56, pp. 335–338, 1983.

[3] M. Lazebnik, D. Popovic, L. McCartney, C. B. Watkins, M. J. Lindstrom, J. Harter, S. Sewall, T. Ogilvie, A. Magliocco, A. T. M. Breslin, W. Temple, D. Mew, J. H. Booske, M. Okoniewski, and S. C. Hagness, "A large-scale study of ultrawideband microwave dielectric properties of normal, benign and malignant breast tissues obtained from cancer surgeries," *Phys. Med. Biol.*, vol. 52, pp. 6093–6115, 2007.

[4] K. Hirasawa, K. Fujimoto, T. Uchikura, S. Hirafuku, and H. Naito, "Power focusing characteristics of ellipsoidal reflector," *IEEE Trans. Antennas Propag.*, vol. AP-32, no. 10, pp. 1033–1039, Oct. 1984.

[5] C. E. Baum, E. G. Farr, and D. V. Giri, "Review of impulse-radiating antennas," in *Review of Radio Science 1996–1999*, W. S. Stone, Ed. Oxford, U.K.: Oxford Univ. Press, 1999, ch. 12.

[6] R. C. Hansen, "Focal region characteristics of focused array antenna," *IEEE Trans. Antennas Propag.*, vol. AP-33, no. 12, pp. 1328–1337, Dec. 1985.

[7] J. W. Sherman, III, "Properties of focused apertures in the Fresnel region," *IRE Trans. Antennas Propag.*, vol. AP-10, no. 4, pp. 399–408, Jul. 1962.

[8] C. E. Baum, "Focal waveform of a prolate-spheroidal impulse-radiating antenna (IRA)," *Radio Sci.*, vol. 42, 2007, RS6S27, DOI: 10.1029/2006RS003556.

[9] S. Altunc, C. E. Baum, C. G. Christodoulou, E. Schamiloglu, and C. J. Buchenauer, "Focal waveforms for various source waveforms driving a prolate-spheroidal impulse radiating antenna (IRA)," *Radio Sci.*, vol. 43, 2008, RS4S13, DOI: 10.1029/2007RS003775.

[10] J. E. Thompson and L. H. Luessen, *Fast Electrical and Optical Measurements*. Leiden, The Netherlands: Martinus Nijhoff, 1986, vol. I, p. 73.

[11] S. Altunc, C. E. Baum, C. G. Christodoulou, E. Schamiloglu, and C. J. Buchenauer, "Design of a special dielectric lens for concentrating a subnanosecond electromagnetic pulse on a biological target," *IEEE Trans. Dielectr. Electr. Insul.*, vol. 16, no. 5, pp. 1364–1375, Oct. 2009.

Target Detection With Impulse Radiating Antenna

Chandra Bajracharya, Shu Xiao, Carl E. Baum, and Karl H. Schoenbach

***Abstract*—A prolate spheroidal reflector antenna focuses subnanosecond pulsed radiation in the near field with a small beamwidth, allowing for applications such as target detection. Confocal imaging in free space has been demonstrated with such an antenna for both transmitting and receiving. A polarized beam allows for the detection of linear target orientation. We show that decreasing the focal spot size by adding a dielectric lens enables us to resolve a target with a typical dimension of 4 cm. The spatial resolution can be further enhanced by increasing the dielectric constant of the lens' innermost layer.**

***Index Terms*—Confocal imaging, dielectric lens, near field, subnanosecond pulses.**

I. Introduction

MICROWAVE imaging, either with narrowband or wideband pulses, can detect the presence of abnormalities in a dielectric medium or retrieve the dielectric properties of a target through an inverse scattering technique. Wideband pulses in imaging systems have been used in subsurface probing, medical imaging, and seeing through walls [1]–[3] because of the high resolution (centimeters in free space) and the ability to penetrate obstacles over a broad spectrum of electromagnetic radiation. Scanning a region of interest can be performed by one antenna using synthetic aperture methods [4] or by an antenna array through digital beamforming [5]. When the antenna's radiation is focused and the target at the focus is scanned, coherent backscattered signals, the signals with the largest amplitude, will be recorded by the same antenna. The incoherent backscattered signals from the out-of-focus background clutter, on the other hand, are shifted in time and can be separated from the target signals. The technique is referred to as confocal imaging. The advantages of confocal imaging are increased signal-to-noise ratio and signal-to-clutter ratio and, therefore, improved target detection capability. The concept of confocal imaging using a fixed-focus antenna was discussed in [2], but the details of the design were not discussed, primarily because the interest was focused on the antenna array, which has the ability to vary the focus in using the digital beamforming.

Manuscript received February 16, 2011; revised April 19, 2011; accepted May 12, 2011. Date of publication May 19, 2011; date of current version May 31, 2011.

C. Bajracharya, S. Xiao, and K. H. Schoenbach are with the Frank Reidy Research Center for Bioelectrics, Department of Electrical and Computer Engineering, Old Dominion University, Norfolk, VA 23529 USA (e-mail: sxiao@odu.edu).

C. E. Baum, deceased, was with the Department of Electrical and Computer Engineering, University of New Mexico, Albuquerque, NM 87131 USA.

Color versions of one or more of the figures in this letter are available online at http://ieeexplore.ieee.org.

Digital Object Identifier 10.1109/LAWP.2011.2157070

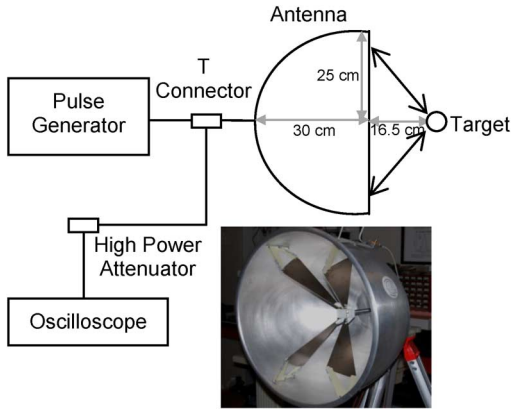

Fig. 1. Confocal imaging system with a near-field, impulse focusing antenna. The pulse generator delivers pulses with a rise-time of approximately 200 ps to the antenna, which focuses the radiation in a focal plane 16.5 cm away from the aperture plane. The prolate spheroidal reflector has a major axis of 30 cm and a minor axis of 25 cm. The aperture plane with a diameter of 50 cm is at the mid-plane of the reflector. The signals scattered by the target in free space are collected by the same antenna and sent to the oscilloscope for analysis.

In this letter, we report the use of a fixed-focus impulse radiating antenna [6], [7] for the confocal target detection. Target detection using this system is limited to targets in free space. Another possible use would be to detect a target embedded in a weakly scattering object so the focal point can be predetermined as in free space. We also use a lens in conjunction with the antenna to decrease the focal spot size and to increase the resolving ability. This lens-antenna system applies in the case when a target is in the subsurface region of a medium with known dielectric properties. The dielectric lens, in conjunction with the antenna, can be used to match the impedance from free space to the medium and to achieve the focus inside the medium. One scenario would be detecting or monitoring cancers in the skin with a lateral scanning at a fixed depth.

II. Confocal Imaging System

The confocal imaging system consists of a pulse generator (FPG-5P, manufactured by FID GmbH, Germany), an oscilloscope (Tektronix TDS7404), and a reflector antenna (Fig. 1). The reflector antenna is based on two foci of an ellipse and launches the subnanosecond pulse from the first focal point to the second, which is 16.5 cm away from the aperture plane [7]. In the confocal configuration, the antenna works as both transmitter and receiver. Usually, the operation of a single antenna as transmitter and receiver requires an ultrafast transmit–receive switch to provide adequate isolation between transmit and receive ports. Here, we instead use a T-connector, which allows the pulses to be fed to the antenna and also allows the returned signal to be sent to an oscilloscope. A high-power attenuator (NMFP-26B, Bath Electronics) is used to reduce the intensity

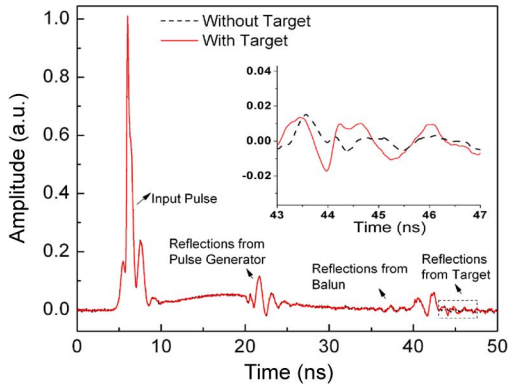

Fig. 2. Recorded signal on the real-time oscilloscope. The signals consist of four parts: 1) the input pulse from the pulse generator (14%–92% rise-time, 200 ps, FWHM: ∼600 ps); 2) the reflection from the pulse generator because of the T-connector; 3) the reflected signal from the antenna balun; and 4) the backscattered signals from the target at the focus.

of the signal, followed by two additional wideband attenuators (PE7045-20, Pasternack) on the scope.

To demonstrate the antenna's operation as a confocal transmitter and receiver, we place an aluminum rod (diameter: 2.54 cm; length: 15.5 cm) at the focus and record the signals from the target. Fig. 2 shows the signals recorded by the oscilloscope with and without the presence of the target. The recorded signal consists of four main parts: the input pulse directly from the pulse generator, the reflections from the pulse generator, the reflected signal from the antenna balun, and the backscattered signals from the target. The first three signals should be invariant and independent of the target scattering. This is confirmed by overlapping the first three signals for both cases with and without the target. The fourth part of the signal varies as a result of the introduction of the target and contains backscattered signals from the target. A more detailed analysis of the signals is not necessary since we are only interested in examining the changes of the signals in the presence of the target versus without the target.

The appearance of the signal changes indicates the presence of a target at the focal point. Once the time window of this change is identified, the oscilloscope is set in a delayed mode so that this particular time window is enlarged by setting a lower voltage scale and shorter timescale. The figure inserted in Fig. 2 shows a significant difference between the signals with and without the presence of the target. We note that the signal near 43–44 ns for the case without a target is most likely due to the reverberation between the TEM feed and the reflector. As a result, the received signal by the same antenna contains ripples in the tail, which coincide with the time window of the signal returned from the target. This coincidence may pose a limitation to some sensing applications where the change of signal obtained by subtracting the background signals is not adequate. One way to reduce the ripples is to employ an offset feed arm to replace the centered feed arm, as discussed in a parabolic impulse antenna [8].

One attractive feature of the antenna is that the wave at the second focus is linearly polarized and can be adjusted either in the vertical or horizontal direction by rotating the antenna. For

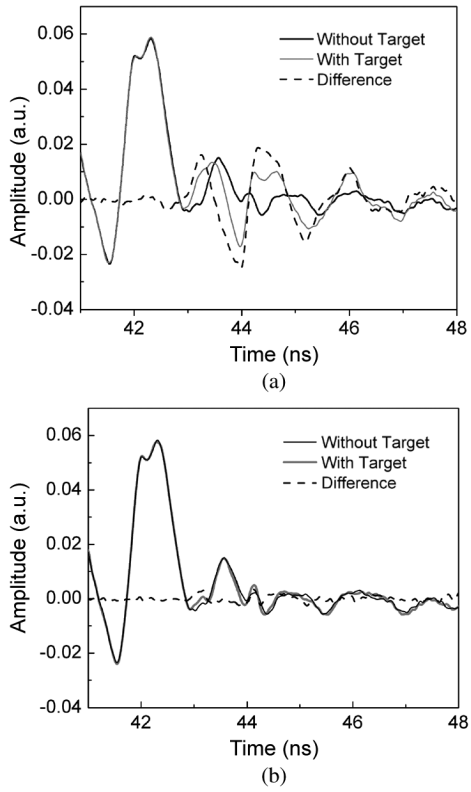

Fig. 3. Received signal for different orientations of a target when the antenna is vertically polarized. (a) The rod is placed at the focus vertically (copolarized). (b) The rod is placed at the focus horizontally (cross-polarized).

linear targets, e.g., a metallic rod (diameter: 2.54 cm; length: 15.5 cm), the backscattered signal is maximum when the target is copolarized [Fig. 3(a)]. For linear targets that are cross-polarized, the antenna rejects the backscattered signals [Fig. 3(b)], so the target is undetectable to the imaging system. This property allows us to selectively scan the targets by examining the intensity of the target return. The orientation of the antenna can be varied until a maximum backscattered signal is observed and the antenna polarization is aligned with the target orientation.

III. Confocal Imaging System With a Dielectric Lens

In the confocal imaging system, decreasing the focal spot size is instrumental to increasing the resolution. One way to reduce the spot size is to use a dielectric lens in conjunction with the reflector antenna, as shown in Fig. 4. The lens is hemispherical. Its focal point is in the geometric center of the hemisphere and overlaps the focus of the reflector antenna. Therefore, the antenna, in conjunction with the lens, is still a confocal imaging system. The lens consists of five layers of different dielectric materials with dielectric constants varying in an exponential profile from free space to the innermost layer, $\varepsilon_{\mathrm{rmax}}$ [9]. Due to the increase of the dielectric constant, the focal spot size can be reduced by a factor of $\varepsilon_{\mathrm{rmax}}^{-1/2}$ at the innermost layer. The choice of the number of layers and their thickness is optimized to permit maximal transmission through these layers. The innermost layer is generally made of the same material as the medium to be probed. In this lens, the outermost layer has a dielectric constant of 1.3, and

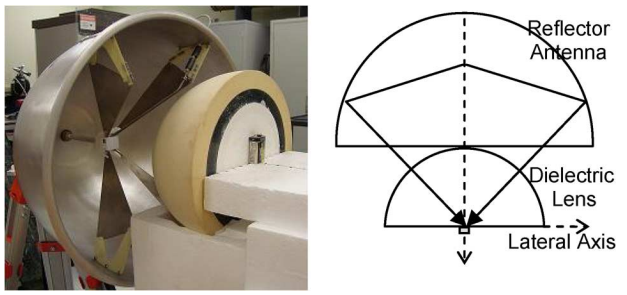

Fig. 4. Reflector antenna used in conjunction with a dielectric lens. The focal point of the dielectric lens at the center of the hemisphere is at the same position as that of the reflector antenna. The diameter of the lens is 30 cm. The target is shifted along the lateral axis and the longitudinal axis, which is equivalent to moving the antenna and lens system to scan the space along the front of the lens.

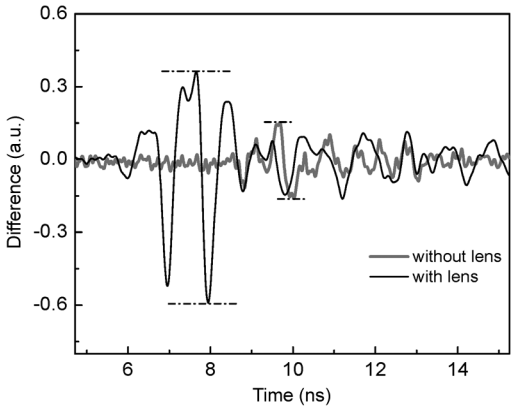

Fig. 5. Comparison of backscattered signal differences with and without the lens. The difference is obtained from the backscattered signal after subtraction of the background signal. The target is a metallic object ($2.5 \times 1.5 \times 4.5$ cm^3), placed at the focus. Dashed, horizontal lines indicate the peak value of the difference.

the innermost layer has a dielectric constant of 9. The five-layer hemispherical focusing lens was made to the lens specifications [9] by TPL, Inc., Albuquerque, NM. The nanocomposite dielectric materials developed by TPL, Inc., were used for the fabrication of the multilayer lens since desired dielectric constants can be achieved. The spot size at the lens focus is approximately 1/3 of that in free space. The lateral focal spot size of the reflector antenna was measured as 11 cm [7], so at the lens surface it is 3–4 cm.

The antenna and lens imaging system were designed to work in the case when a target is embedded in a medium that has the same dielectric constant as the innermost layer [9]. Therefore, this imaging system requires knowledge of the medium dielectric property when designing such a lens. Here, we consider a simpler case: a metallic target ($2.5 \times 1.5 \times 4.5$ cm^3) placed in free space and in front of the lens. The experimental setup is shown in Fig. 4. We compare the difference of the backscattered signals with and without the lens. As shown in Fig. 5, the lens significantly increases the difference of the scattered signal. The maximum difference (peak to peak) for the case with lens is 0.95, approximately three times greater than without the lens (0.3), which is an indication of improved sensitivity. We move the target along the lateral axis and keep the antenna and

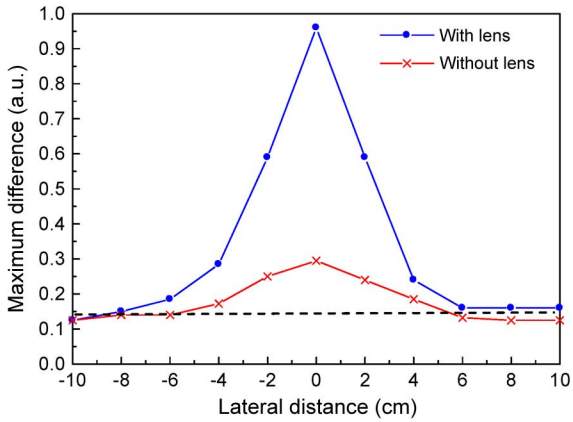

Fig. 6. Maximum differences of backscattered signals with and without the lens. The target is a metallic object ($2.5 \times 1.5 \times 4.5$ cm^3). At each lateral distance, the data is obtained by subtracting the two peaks in the difference between the backscattered signal with/without the presence of the target (Fig. 5). The focus is at zero distance from the planar lens surface.

lens static, which is equivalent to shifting the imaging system and scanning the region laterally.

The maximum differences for the cases with and without the lens are plotted in Fig. 6. For the case without the lens, the maximum differences beyond the lateral distances of ± 6 cm are in actuality the same as the noise level, which makes it hard to detect the target. For the case with the lens, the detectable range is approximately the same. When the baseline is chosen as 0.15, the full width at half-maximum (FWHM) for the case with the lens is approximately 4 cm, whereas the FWHM is approximately 6 cm without the lens. Since the FWHM of the scattering difference determines the image resolution, the resolution is therefore increased by a factor of 1.5. It is noticed that although the focal spot size is reduced by a factor of 3 [7], the resolution, i.e., the FWHM of maximum difference, is not increased accordingly by the same factor. This result suggests that the focal spot size is not the only factor that determines the imaging resolution, as the receiving characteristics of the antenna with or without the lens also contributes to the difference in the received signals.

To further verify the imaging resolution of the lens-antenna system, we have imaged two targets of equal dimensions ($2.5 \times 1.5 \times 4.5$ cm^3) with different spacing. Again, the two objects are shifted from one edge of the lens to the other, which is equivalent to laterally scanning the two objects with the antenna-with-lens system. The background signals are subtracted from the signals obtained at each target location. The value of the difference is used to construct a 2-D image by assigning pixel values according to the magnitude of the signals received. Fig. 7 shows the image constructed with two objects with spacing of 3.5 and 5.5 cm. The two targets are irresolvable in the lateral direction when the spacing is shorter than 3.5 cm. However, the imaging system is able to distinguish targets for a spacing of 5.5 cm, so the resolution can be estimated as 4 cm.

While we have demonstrated confocal scanning in the lateral direction, longitudinal scanning is beneficial to probe a more deeply buried target. Because the focus is fixed along the longitudinal axis in our system, the confocal configuration can only detect targets near the focus, which means close to the lens

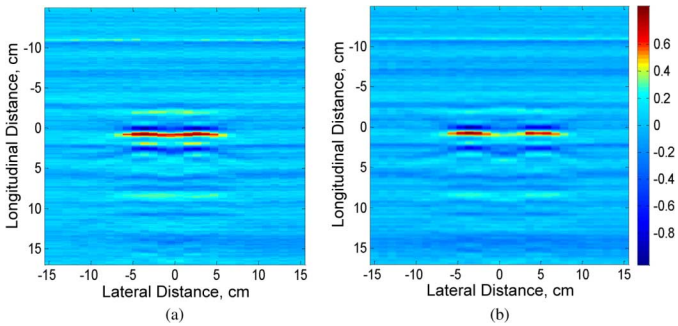

Fig. 7. Images of two identical metallic objects ($2.5 \times 1.5 \times 4.5$ cm^3) that are separated by (a) 3.5 cm and (b) 5.5 cm. The two objects can be resolved at a lateral spacing of 5.5 cm, but are irresolvable for 3.5 cm.

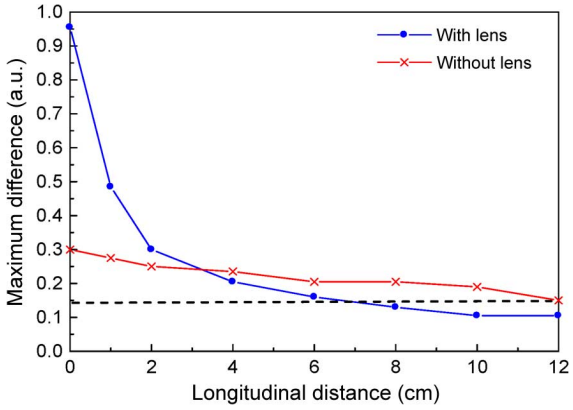

Fig. 8. Maximum differences of backscattered signals with and without the lens. The target is a metallic object ($2.5 \times 1.5 \times 4.5$ cm^3). At each longitudinal distance, the data is obtained by subtracting the two peaks in the difference between the backscattered signal with/without the presence of the target (similar to the signals shown in Fig. 5). The focus is at zero distance from the planar lens surface.

surface. Longitudinal confocal scanning therefore requires different lenses with different focus. Here, we demonstrate confocal detection of a target when the target is placed along the longitudinal axis of the lens. Fig. 8 shows the maximum differences of the signals in the cases with and without the lens. At the focal point (longitudinal distance $= 0$), the difference is greatest and is about three times higher than without the lens. Until the target is moved 2 cm away from the focus, we still obtain a higher difference than without the lens. Beyond 2 cm, the difference decreases faster with the lens than without, as the wave exiting the lens is an evanescent wave and decreases exponentially in space.

IV. Conclusion

We have explored near-field target detection with a focusing prolate spheroidal antenna using a confocal technique. As the antenna was designed to focus in free space, the use of such a system is limited to the detection of targets in free space or otherwise embedded in a weakly scattering medium. When linear targets are placed at the focal position, the antenna is sensitive to their orientation. A focusing antenna in conjunction with a dielectric lens has been shown to have a resolution of approximately 4 cm. The resolution can be further improved by increasing the dielectric constant of the material in the innermost layer of the lens. Our present confocal system prevents a scanning of depth as the target needs to be placed close to the lens, within 2 cm of the focus, in order to show a stronger signal return compared to without the lens. Scanning of depth may be possible if the probed object is placed within a lens of a different design.

References

[1] L. Peters, Jr., J. J. Daniels, and J. D. Young, "Ground penetrating radar as a subsurface environmental sensing tool," *Proc. IEEE*, vol. 82, no. 12, pp. 1802–1822, Dec. 1994.

[2] S. C. Hagness, A. Taflove, and J. E. Bridges, "Two-dimensional FDTD analysis of a pulsed microwave confocal system for breast cancer detection: Fixed-focus and antenna-array sensors," *IEEE Trans. Biomed. Eng.*, vol. 45, no. 12, pp. 1470–1479, Dec. 1998.

[3] A. O. Boryssenko, E. Boryssenko, V. Ivashchuk, A. Lishchenko, and V. Prokhorenko, "UWB subsurface radar with antenna array for imaging of internal structure of concrete structural elements," in *Ultra-Wideband Short Pulse Electromagnetics*. Norwell, MA: Kluwer/Plenum, 2002, vol. 5, pp. 199–206.

[4] M. Dehmollaian, M. Thiel, and K. Sarabandi, "Through-the-wall imaging using differential SAR," *IEEE Trans. Geosci. Remote Sens.*, vol. 47, no. 5, pp. 1289–1296, May 2009.

[5] X. Li, E. J. Bond, B. D. Van Veen, and S. C. Hagness, "An overview of ultra-wideband microwave imaging via space-time beamforming for early-stage breast cancer detection," *IEEE Antennas Propag. Mag.*, vol. 47, no. 1, pp. 19–34, Feb. 2005.

[6] C. E. Baum, "Focal waveform of a prolate-spheroidal impulse-radiating antenna," *Radio Sci.*, vol. 42, p. RS6S27, 2007.

[7] S. Xiao, S. Altunc, P. Kumar, C. E. Baum, and K. H. Schoenbach, "A reflector antenna for focusing subnanosecond pulses in the near field," *IEEE Antennas Wireless Propag. Lett.*, vol. 9, pp. 12–15, 2010.

[8] K. Kim and W. R. Scott, "Impulse-radiating antenna with an offset geometry," *IEEE Trans. Antennas Propag.*, vol. 53, no. 5, pp. 1738–1744, May 2005.

[9] S. Altunc, C. E. Baum, C. J. Buchenauer, C. G. Christodoulou, and E. Schamiloglu, "Design of a special dielectric lens for concentrating a subnanosecond electromagnetic pulse on a biological target," *IEEE Trans. Dielect. Elect. Insul.*, vol. 16, no. 5, pp. 1364–1375, Oct. 2009.

A Hyperband Antenna to Launch and Focus Fast High-Voltage Pulses Onto Biological Targets

Prashanth Kumar, *Member, IEEE*, Carl E. Baum, *Life Fellow, IEEE*, Serhat Altunc, *Member, IEEE*, Jerald Buchenauer, *Member, IEEE*, Shu Xiao, *Member, IEEE*, Christos G. Christodoulou, *Fellow, IEEE*, Edl Schamiloglu, *Fellow, IEEE*, and Karl H. Schoenbach, *Fellow, IEEE*

***Abstract*—This paper briefly reviews the design of a prolate-spheroidal impulse-radiating hyperband antenna system to launch and focus fast (100 ps) high-voltage (>100 kV) pulses onto biological targets. Design and experiments on a graded five-layer dielectric lens, designed to match the pulses into the target medium, are outlined. The design and numerical simulations of a switch system to launch high-voltage spherical TEM pulses are also presented.**

***Index Terms*—Apoptosis, focusing lens, hyperband antenna, impulse-radiating antenna, launching lens, picosecond pulses, prolate-spheroidal reflector, switch.**

I. Introduction

THE EFFECT of high-intensity nanosecond electrical pulses on biological cells and tissue has received considerable attention by the scientific community, particularly over the past five years, and has led to the establishment of a new research field: bioelectrics [1]. In the time domain below approximately 100 ns, the rise time of the pulse is faster than the charging time of the plasma membrane of most mammalian cells, meaning that the field will pass through the membrane into the cytoplasm. High-voltage pulses in the nanosecond range have been shown to penetrate into living cells to permeabilize intracellular organelles, and release Ca^{2+} from the endoplasmic reticulum. They provide a new approach for physically targeting intracellular organelles with many applications including activation of platelets and release of growth factors for accelerated wound healing [2] and precise control of programmed cell death (apoptosis), which has been shown to cause complete elimination of melanoma tumors [3]. The pulses were, in this case, delivered by needle-electrodes to the tumors.

Manuscript received July 02, 2010; revised December 29, 2010; accepted January 08, 2011. Date of publication March 03, 2011; date of current version April 08, 2011.

P. Kumar is with the Department of Electrical Engineering, University of New Mexico, Albuquerque, NM 87131 USA (e-mail: prash@unm.edu).

C. E. Baum, S. Altunc, J. Buchenauer, C. G. Christodoulou, and E. Schamiloglu are with the Department of Electrical and Computer Engineering, University of New Mexico, Albuquerque, NM 87131 USA (e-mail: cebaum@ece.unm.edu; serhat.altunc@nasa.gov; cjbuch@ece.unm.edu; christos@ece.unm.edu; edl@ece.unm.edu).

S. Xiao and K. H. Schoenbach are with the Department of Electrical and Computer Engineering, Old Dominion University, Norfolk, VA 23508 USA (e-mail: sxiao@odu.edu; schoenbach@ece.odu.edu).

Color versions of one or more of the figures in this paper are available online at http://ieeexplore.ieee.org.

Digital Object Identifier 10.1109/TMTT.2011.2114110

The bioelectric effects of ultrashort square wave pulses were shown to follow a scaling law [4]

$$S = S(E\tau N^{1/2}) \tag{1}$$

with S being a quantity that describes the intensity of the observable bioelectric effect, E being the electric field amplitude, τ being the pulse duration, and N being the number of pulses. This law, which was shown to hold for nanosecond pulses, indicates that for picosecond pulses to achieve similar effects the electric field will need to be much higher than for nanosecond pulses. However, there are two reasons to enter the picosecond-pulsed electric field range. The first one is that for extremely short pulses, the permittivity of the various cell components, rather than their resistivity, determines the electric field distribution in the cell [5]. The electric field then acts directly on membrane proteins, rather than causing charging of the membrane, and, if sufficiently strong, can cause direct and instant conformational changes. Subnanosecond pulses (200 ps) were found to alter the cell membrane conductance and unirectifying channels are formed when cells are exposed to electric field strength on the order of 20 kV/cm [6] for 2000 pulses. The disruption of the membrane integrity may lead to the change of physiological conditions of the cell and cause cell death.

Second, besides providing the opportunity to explore a new field of electric field-cell interactions, subnanosecond pulses will ultimately allow medical applications for delivery of pulsed electric fields without invasive electrodes, using antennas instead. A possible configuration that allows us to generate very high electric fields uses a focusing antenna [7], [8] and may be able to induce apoptosis in tissue without using needles as the delivery system for electric pulses, Fig. 1. In addition to using a reflecting antenna, efforts are underway to utilize lenses in combination with the reflector in order to achieve higher spatial resolution [9], [10].

Besides using ultrashort (10 ns) electrical pulses for medical therapies [11], the pulsed radiation may lead to medical imaging methods. Imaging is based on the measurement of changes in the complex permittivity of tissue, and may complement other methods based on the measurement of other physical parameters, such as X-ray computed tomography (CT), magnetic resonance imaging (MRI), and ultrasound. Generally, the resolution is limited by the diffraction time, which restricts the detectable target size to larger than the pulsewidth. For example, the spatial resolution in the centimeter range is expected if the pulse is near 100 ps. In such an imaging system, the electromagnetic waves

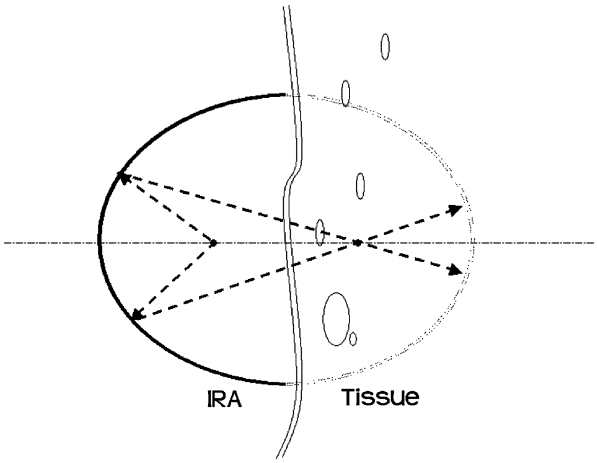

Fig. 1. Concept of treatment of cancerous tissue inside the body. For imaging a second, an identical IRA in a confocal arrangement could be used as a receiver.

are focused on a target inside the body. The scattered signal contains information on the dielectric properties and the geometry of the target and allows its identification through an inverse scattering method. 3-D scanning allows us to obtain the dielectric profile of the tissue and to detect any abnormality in a uniform background.

Research on the use of impulse radiating antennas (IRAs) for medical applications requires, in addition to the development of focusing antennas, research on the biological effect of subnanosecond pulses. Experimental studies with 800-ps-long pulses with electric field amplitudes of up to 1 MV/cm applied to melanoma (B16) cells have provided information on the pulse parameters required to induce cell death [5]. Studies with 200-ps-long pulses are underway. First results indicate that cell death requires a large number of pulses $(>10^6)$ at moderate electric field intensities of 20 kV/cm [6]. However, synergistic effects such as caused by local tissue heating might allow us to reduce the pulse number considerably, and to establish IRAs as a new tool in treatment of cancer.

This paper presents a prolate-spheroidal impulse radiating antenna (PSIRA) system to focus fast (100 ps) high-voltage $(>100\text{-kV})$ pulses on to a biological target. The treatment of skin cancer (melanoma) is used as an illustrative example. Currently, needle arrays are used for treating melanoma tumors. This approach is invasive and often results in discomfort to the patient. The PSIRA has the advantage of noninvasively delivering the required pulsed electric fields to melanoma tissues. By directly focusing on the target cells, it reduces damage to the tissue layers surrounding the target and skin.

The design of the PSIRA and focusing lens system are briefly reviewed in this paper. New experimental results comparing the focal impulse waveforms and the beamwidths, in air and in the focusing lens, are presented. It is found that the focusing lens can be viewed as a bandpass filter. The design of a switch system to launch high-voltage $(\geq 100\text{-kV})$ spherical TEM pulses from such an antenna are detailed. The experimental results on the focusing lens and the design of the switch system are significant novel contributions that complete the conceptual realization of the PSIRA system. The details provided in this paper can be used for the fabrication and deployment of a prototype PSIRA system, with the focusing and launching lenses, as a less invasive, safer, and more effective treatment method.

II. PSIRA

The IRA is a focused aperture hyperband[1] antenna suited for radiating very fast high-voltage $(>100\text{-kV})$ pulses in a narrow beam [14]. A fast-rising step-like input into the antenna gives an approximate delta-function response. IRAs thus provide an attractive means to deliver electric pulses to induce apoptosis in tissue cells without using needles.

A. Prolate-Spheroidal Reflector

IRAs are composed of two main parts: a conical TEM transmission line, called the feed arms, and a focusing optic, which is usually a reflector or a lens. Paraboloidal reflector IRAs, where the radiated impulse is focused at infinity, are by far the most common, as they have been used in a variety of applications such as transient radars, buried target identication, etc. However, for use in the biological application described above, where electric fields need to be focused onto a target in the near field, a prolate-spheroidal reflector must be used [7], [15].

The front and side views of a four feed-arm PSIRA are shown in Fig. 2. The feed-arms are oriented at 60°, as this amplifies the field intensity by a factor of 1.606 compared to the two-arm configuration [16]. The dimensions of the feed arms are determined by their 200-Ω pulse impedances.

The PSIRA system has two foci. An inhomogeneous spherical TEM wave launched on guiding conical conductors from one focus $(-z_0)$ is converted, by a double stereographic transformation, to a second (reflected) inhomogeneous spherical TEM wave propagating toward the second focus (z_0) [17].

B. Focal Waveform

For an ideal step input, the electric field waveform at the second focal point is shown in Fig. 3. The waveform has three main parts: the pre-pulse, impulse, and post-pulse. The pre-pulse is the direct radiation from the feed. It has a low magnitude and lasts for a long duration. The impulse is due to the fields from the reflector converging at the focal point. It lasts for a short time and has a large amplitude. The post-pulse is mostly due to diffraction effects and the fields outside the aperture. The pre-pulse and impulse dominate the early-time (high frequency) behavior of the IRAs, while the post-pulse provides information on the late-time (low frequency) behavior. The prolate-spheroidal reflector differentiates the input; the derivative of the step input thus results in the impulsive part of the waveform. It is the impulse that induces electroporosis or apoptosis in the cells, and therefore, must be maximized.

C. Optimization of Reflector Dimensions

The pre-pulse reduces the amplitude of the impulse. It is therefore desirable to have as small a pre-pulse as possible. The magnitude of the pre-pulse is solely determined by the size of the reflector [15], [17]. The reflector geometry and position of

[1]The term hyperband refers to a band ratio (not bandwidth) greater than one decade [12]. It is a well-established International Electrotechnical Commission (IEC) standard (61000–2–13) [13].

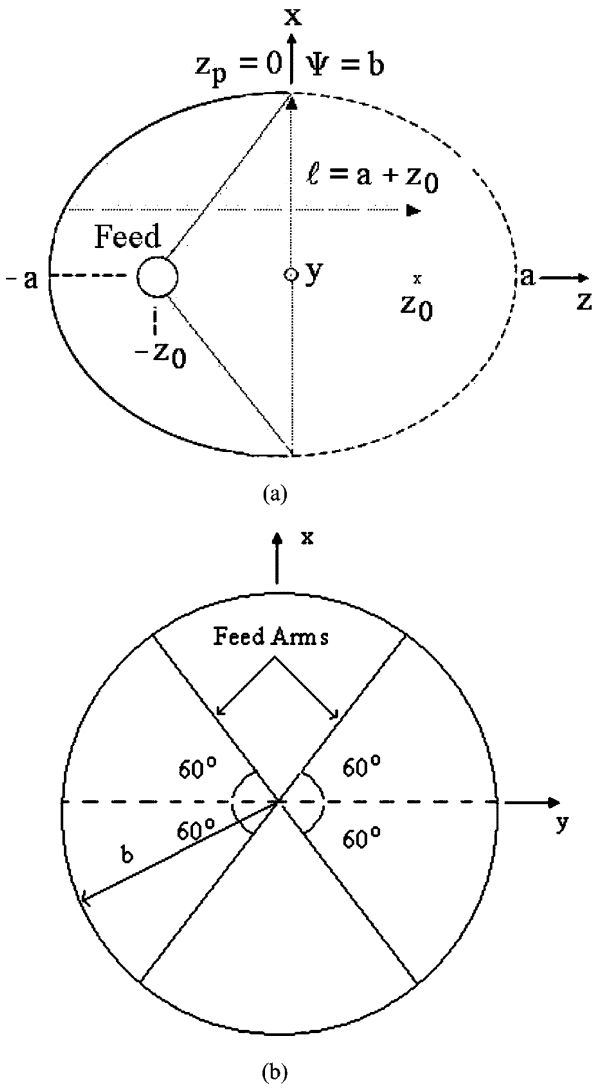

Fig. 2. Side and front views of the prolate-spheroidal reflector. (a) Side view. (b) Front view.

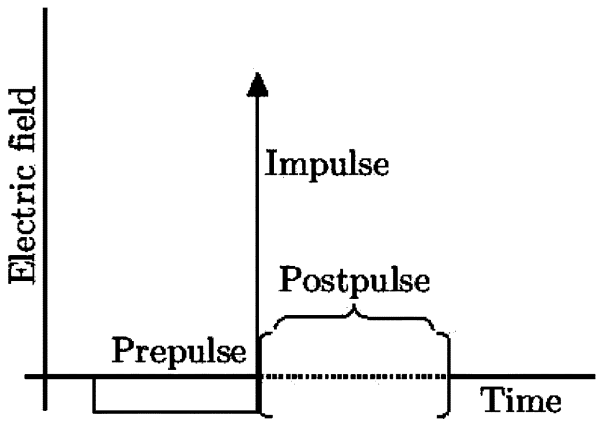

Fig. 3. Idealized electric field waveform at the second focal point.

the truncation plane z_p are optimized to obtain an acceptable compromise between the physical dimensions of the reflector and the pre-pulse amplitude.

After investigation of various electromagnetic parameters, the following dimensions were found to be most suitable [7], [15]:

$$z_p = 0 \quad a = 0.625\ \text{m} \quad b = \Psi = 0.5\ \text{m} \quad z_0 = 0.375\ \text{m} \quad l = 1\ \text{m} \tag{2}$$

where

$z_p = z$ – coordinate of the truncation plane
$a, b =$ radii of the prolate-spheroid
$z_0 = (a^2 - b^2)^{1/2}$ focal distance
$l = a + z_0 =$ distance used for normalization
$\Psi =$ radial coordinate

as shown in Fig. 2(a). For the values in (2), the reflector can be easily fabricated. The symmetry of the geometry greatly also simplifies the problem.

A pulsewidth of 100 ps is used to validate the applicability of the PSIRA to deliver pulses in the picosecond regime. A 100-ps pulse duration leads to a reflector with practically acceptable dimensions. For pulses less than 100 ps, the reflector can be made smaller. For pulsewidths greater than 100 ps, a larger system is required. However, using the PSIRA system for pulses with durations much greater than 100 ps, e.g., >500 ps, is not recommended, as the size of the system may not be very practical. The reflector dimensions in (2) were optimized for a 100-ps ramp rising input.

CST Microwave Studio, a 3-D finite integral time domain (FITD) commercially available software, was used for simulations. A 1-V 100-ps ramp rising step was used as the input in all simulations.

III. Focusing Lens

Section II considered the design of a prolate-spheroidal reflector for concentrating a pulse, in the near field, from one of the foci onto a target at the second focus. The idea is to get a very fast very intense electromagnetic pulse to illuminate the target (e.g., a tumor). By very fast we mean fast enough to get the spot diameter (beamwidth) at the focus down to the target size, or as close to this as technology allows. At the same time, a small spot size also implies large fields [18].

One problem with placing fields on the target concerns the dielectric properties of the target medium and its surroundings. If the wave incident on the target is in air, but the target medium has a large relative permittivity (say, about 81 for water), then there will be a significant reflection of the pulse, leading to a smaller field in the target medium [18]. This section discusses the addition of a lens, called the focusing lens, to better match the wave to the target, and to reduce spot size, thereby increasing the field on the target. A schematic of the PSIRA and focusing lens system is shown in Fig. 4. A brief overview of the design and experiments on a five-layer lens is presented [10].

The PSIRA and lens system can deliver 100-ps electric field pulses with a spatial resolution in the millimeter range. While

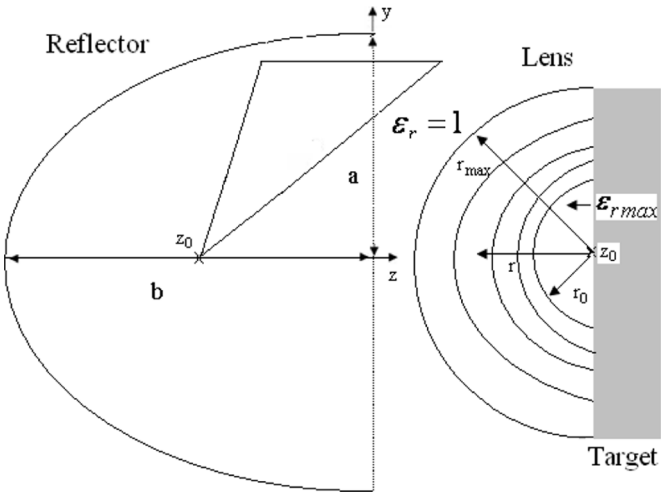

Fig. 4. PSIRA and lens system to focus and match into (biological) target medium [10].

our experiments use 10-V 45-ps rising signals, the design is for 100 kV or greater to achieve the desired field strengths with 100-ps rising pulses.

A. Summary of Design

The design of a spatially limited graded hemispherical dielectric focusing lens, with relative permitivity varying from $\epsilon_{r_{\min}} = 1$ to $\epsilon_{r_{\max}} = 81$, is based on a transmission line model. There are two important parameters to consider in the design, which are: 1) the dimension of the lens and 2) the number of layers. Detailed calculations to minimize the lens radius and optimize the number of layers are provided in [9] and [10]. The lens is designed such that all layers have the same electrical width. A ten-layer lens with a 15-cm radius was found to provide satisfactory electric enhancement.

Based on plane-wave approximations, scaling relationships for various electromagnetic parameters are calculated in [10] and [19]. The following results are most significant:

- electric enhancment $= \epsilon_{r_{\max}}^{1/4}$;
- focal spot size reduction $= \epsilon_{r_{\max}}^{-1/2}$;
- displacement enhancement $= \epsilon_{r_{\max}}^{5/4}$;

as they are used to quantify the efficacy of the lens. The large displacement enhancement is extremely advantageous, as it is the electric displacement that acts on the (abnormal) cells.

The graded lens design assumes that the biological target is placed in direct contact with the last layer. Some preliminary considerations regarding the problems and design options for focusing more deeply buried targets are presented in [20]. The focal spot size will be affected if the lens is used on an uneven surface as the rays arrive at the focal point at different times. For such uneven surfaces, more innovative techniques for using the lens are currently being explored [10]. As a proof-of-concept, a five-layer focusing lens, $\epsilon_{r_{\min}} = 1$ to $\epsilon_{r_{\max}} = 9$, is considered in this paper. Numerical simulations and experiments, explained in Section IV, are used to demonstrate the viability and applicability of such a system.

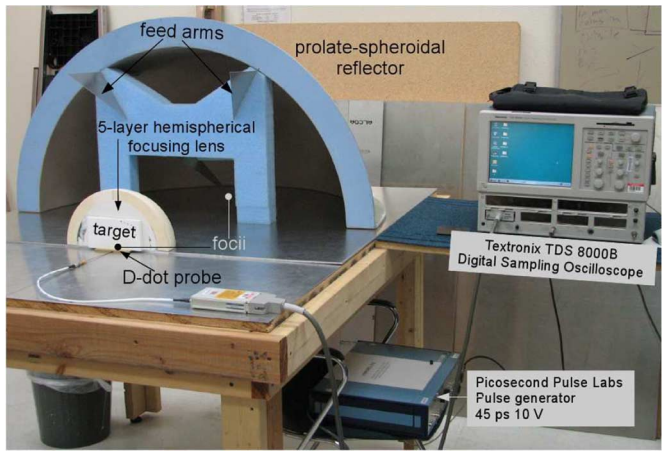

Fig. 5. Experimental setup of 60° four feed-arm PSIRA with focusing lens, target, and D-dot probe [10].

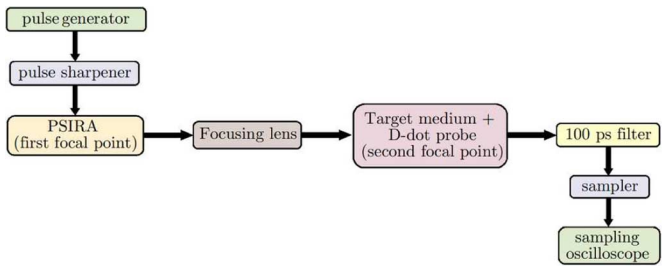

Fig. 6. Block diagram of the experimental setup.

B. Experimental Results

Fig. 5 shows the experimental setup. A block diagram of the setup is shown in Fig. 6. It consists of a prolate-spheroidal reflector and two feed arms at 60° over a ground plane, i.e., a 60° four feed-arm PSIRA configuration. A 10-V 45-ps ramp-rising signal, generated by a Picosecond Pulse Laboratories, Boulder, CO[2] pulse generator, was used as a source at the first focal point. Our analytical calculations assume an input with a rise time of 100 ps. Therefore, a filter is placed between the D-dot probe and the sampler. This filter converts the 45-ps signal from the pulser to one with a rise time of 100 ps [21]. The lens and target medium (slab) are placed at the second focal point.

The five-layer hemispherical focusing lens and target were made to our specifications by TPL Inc., Albuquerque, NM.[3] The nanocomposite dielectric material developed by TPL Inc. is ideal for the fabrication of our multilayer lens since desired dielectric constants can be achieved. The lens is placed at the second focal point. A slab placed in front of the lens is used to simulate the target medium. A handmade fast D-dot sensor is placed inside the target medium. The signal from the D-dot probe was measured using a Textronix TDS 8000B digital sampling oscilloscope. The experimental results are normalized to a 1-V input [10].

Complete details of the D-dot probe are provided in [10] and [21]. Basically, the probe is a 3-mm-high 2-D teardrop-shaped electrode designed to have a pulse impedance of 50 Ω in the dielectric medium, i.e., 150 Ω in air. The impedance mismatch

[2][Online]. Available: http://www.picosecond.com/

[3][Online]. Available: http://www.tplinc.com/

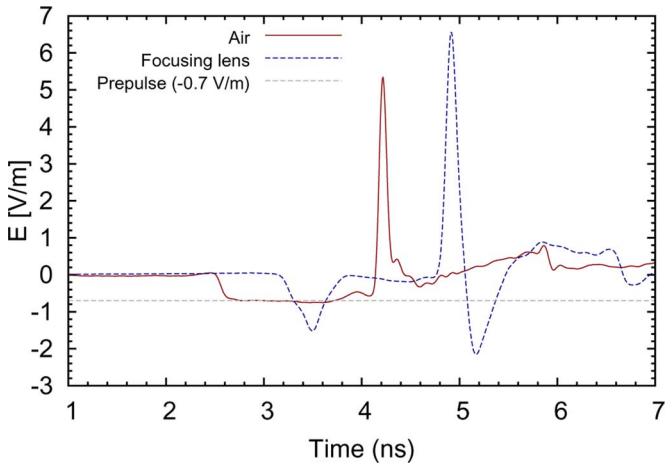

Fig. 7. Comparison of focal impulse waveforms, at the second focal point, in air and inside the lens, with the 100-ps filter.

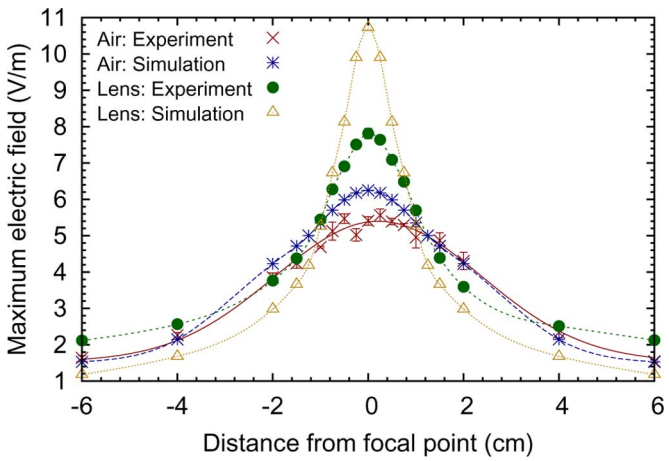

Fig. 8. Comparison of simulation and experiment results of beamwidth in air and inside the lens.

between the probe tip and the input pulse, for the measurements in air, causes reflections. However, the probe, of height $h = 3$ mm, is resonant at frequencies above

$$f \approx \frac{c}{\frac{h}{4}} = \frac{3 \times 10^{11} \text{ mm}}{0.75 \text{ mm}} = 0.4 \text{ THz} \tag{3}$$

i.e., in a quasi-static sense, the measurements are valid over a very large frequency spectrum of the input pulse and are therefore considered to be sufficiently accurate.

The measurement of fast (≤ 100 ps) electromagnetic pulses inside a high-permittivity medium presents some challenges. These are especially associated with the shorter wavelengths and the contact of the D-dot antenna with the medium. Some techniques to mitigate these problems to some degree are discussed extensively in [22]–[24].

Fig. 7 compares the focal impulse waveforms in air and inside the focusing lens. The amplitude of the impulse in air is 5.44 V/m and the full width at half maximum (FWHM) is 85 ps. One would expect the FWHM to be identical to the maximum rate of rise of the input pulse, i.e., $t_{\text{mr}} = 100$ ps [21]. The reason for this discrepancy is that the higher frequencies in the input pulse are better focused than the lower frequencies, i.e., the focusing action itself filters out lower frequency content in the focused waveform. Similar results observed in simulations corroborate this explanation. The amplitude of the impulse in the focusing lens is 7.66 V/m and the FWHM is 127.5 ps. The large FWHM is most likely due to loss and dispersion in the lens materials (without loss and dispersion, the FWHM would be 100 ps).

In Fig. 7, one observes the enhancement inside the lens. Since the half-widths of the impulse responses in air and in the lens are not identical, the electric enhancement is given by the ratio of the areas, $A = (\text{halfwidth})\,(\text{peak amplitude}) = \text{FWHM} \cdot E_{\max}$, under the curves, i.e.,

$$\begin{aligned} A_{\text{impulse-air}} &= (85 \text{ ps})\,(5.44 \text{ V/m}) \\ &= 462.4 \text{ ps V/m} \\ A_{\text{impulse-lens}} &= (127.5 \text{ ps})\,(7.66 \text{ V/m}) \\ &= 976.65 \text{ ps V/m}. \end{aligned}$$

TABLE I
BEAMWIDTH OF ELECTRIC FIELD IN AIR AND WITH FOCUSING LENS

	Simulation	Experiment
No lens (EFSS_{NL} in cm)	3.61	4.451
With Lens (EFSS_{WL} in cm)	1.19	2.036
$\text{EFSS}_{\text{WL}}/\text{EFSS}_{\text{NL}}$	3.04	2.187

The electric enhancement is $A_{\text{impulse-lens}}/A_{\text{impulse-air}} \approx 2.11$. This is much larger than the analytical estimate, $\epsilon_r^{1/4} = 8.2^{1/4} \approx 1.69$. The reason for this disagreement is due to the 85-ps FWHM of the impulse in air [21]. The analytical approximations do not consider the filtering of the lower frequencies due to the focusing of the wave, at the second focal point, in air. This results in a much higher electric enhancement, as observed above. Of course, one could also simply examine the ratio of the peak electric fields inside the lens and in air, which is $7.66/5.44 = 1.408$. The analogous enhancement obtained from simulations is $10.725/6.247 = 1.717$.

Fig. 8 compares the numerical simulation and experimental results of the beamwidth in air and in the lens. Errors in the experimental data are of the order of the spot size. Note that the geometric focal point in the lens is shifted to the right by approximately $x = +0.25$ cm. The discrepancy between the experimental and numerical results is due to losses occurring in the lens materials; the width of the pulse emerging from the lens is 127.5 ps, which results in a larger spot size. A summary of the spot sizes is given in Table I. Again, these results agree well with those expected from the analytical calculations.

C. Focusing Lens as a Bandpass Filter

The ratio of the magnitudes of the Fourier transform of the impulse waveforms from experiments, in the lens and in air, is shown in Fig. 9.

The bandwidth of the lens is approximately 3 GHz, from 0.4 to 3.4 GHz. Above 3.5 GHz, there is almost no electric field enhancement (analytical or experimental). The focusing lens thus acts as a bandpass filter, filtering frequencies below 0.4 GHz

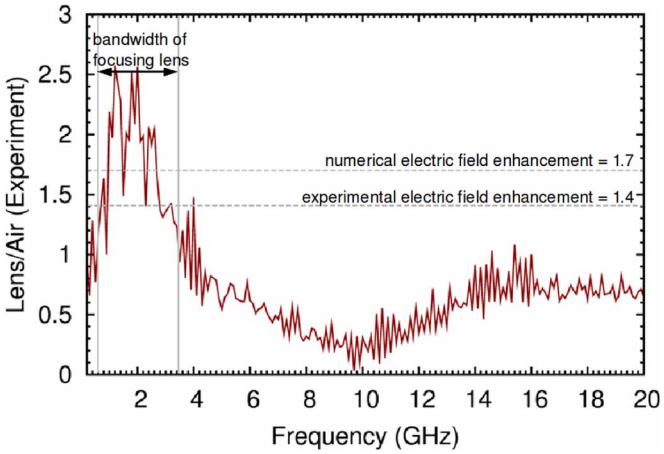

Fig. 9. Ratio of magnitude of Fourier transform of the focal impulse waveform from experiments.

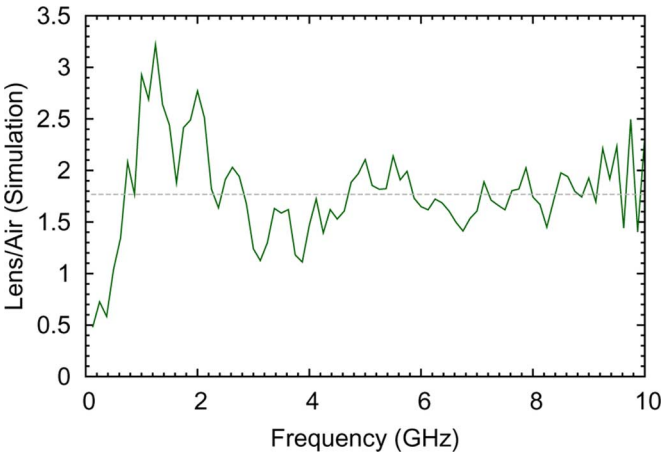

Fig. 10. Ratio of magnitude of Fourier transform of the focal impulse waveform, from simulations, for an input pulse with 100-ps rise time. The dotted gray line is 1.77, the electric enhancement obtained with the lens.

and above 3.4 GHz. The filtering of higher frequencies is due to losses occurring in the lens materials, while the the lower frequencies are filtered due to the lens geometry [25].

The curve in Fig. 9 is compared to similar results obtained from simulations in Fig. 10. The (average) amplification is approximately 1.77 (dotted gray line) up to a frequency of 10 GHz, as expected, since the lens materials are assumed lossless and dispersionless in the simulations. This is closer to that obtained from the ratio of the peak focal electric fields, i.e., $10.725/6.247 = 1.717$. Therefore, the analogous experimental enhancement, $7.66/5.44 = 1.408$, is considered in Fig. 9.

IV. Switch System Design

For input voltages of 100 kV or more, a switch system and "launching" lens are necessary to effectively launch a spherical TEM wave from the first focal point. The switch system consists of switch cones, a pressure vessel (PV), and a gas (typically hydrogen) chamber. The hydrogen chamber (HC) is required to support the high field intensities without breaking down, and hence, allow conduction. The design and numerical simulations of such a switch system and launching lens are presented in this section. Although the input for the numerical simulations is only 1 V, analogous designs for the prototype IRA tested at high-voltages ($>$100 kV) [26] indicate that similar results can be expected for the switch system configurations in this section.

A. Initial Launching Lens Designs

The initial approach to the design of a launching lens followed methodologies similar to those used in the prototype IRA [27]. This approach assumes the feed point and the focal point to be spatially isolated. The objective of the lens design is to ensure that, within the lens, a spherical TEM wave is centered on the feed point. However, outside the lens, an approximate spherical TEM wave is centered at the first focal point. Uniform and nonuniform designs explored are summarized below.

1) Uniform Lens Design: Analytical calculations defining the boundary of a dielectric lens, with fixed relative permittivity, are detailed in [28]. These equations are derived using high-frequency (optical) approximations. It is shown that the dielectric constant required for such a design must be greater than 25. This constraint is a serious drawback since materials with such high dielectric constants have a large loss and dispersion.

2) Nonuniform Lens Design: Lower dielectric constants can be obtained by designing a lens in which the ϵ_r varies (discretely) across the lens boundary. Note that the lens is assumed to be a body-of-revolution. An analytically aided simulation approach is used. The lens boundary, dielectric constants of various layers, and thicknesses of the layers are first estimated analytically. Simulations are then used to examine the time-of-arrival of electric fields on a spherical surface to ensure that a spherical TEM wave originates from the first focal point. This procedure is iterated until the design is achieved within the desired tolerance. Two designs are described below: the planar and the conical [29]–[32].

Planar Design: The planar lens is one in which the relative permittivity of the layers varies along the (rotational) axis of the lens. The design is log periodic, i.e., all layers have the same electrical length. Three- and six-layer designs were investigated. Simulations indicated that the time spread in the rays originating from the source was over 100 ps. This time spread is highly undesirable, as it indicates that the spherical wavefront is distorted well beyond the acceptable tolerance of 20 ps.

Conical Design: In this design, the relative permittivity of the layers is a function of the polar angle θ. Simulation results from a seven-layer configuration were almost identical to the planar design.

Due to the very large distortion of the spherical wave, the planar and conical designs were not iterated, as this would have been too resource intensive. The large distortion in the spherical wavefront could be due to many reasons, such as the optical approximations breaking down at lower frequencies, reflections from inner layers, etc. This approach was abandoned in favor of the simpler designs described in Sections V and VI.

B. Investigation of Various Switch Configurations

In the design of the launching lens described above it was assumed that the feed point and first focal point were spatially isolated. This assumption imposed a severe constraint on the lens design. The problem is greatly simplified if the geometric center of the feed point is made to coincide with the first focal point.

TABLE II
PEAK FOCAL IMPULSE AMPLITUDE AND BEAMWIDTH FOR VARIOUS SWITCH CONFIGURATIONS

Configuration	$E_{\max}$ (V/m)	Spot size (cm)
VBCS-75	6.727	3.894
VBCS-100	5.619	4.065
VBCS-125	4.708	4.304
VBCS-150	4.057	4.414
4FASC	6.363	3.546
T4FASC	7.217	3.889
S4CFA	5.114	3.39

VBCS-Z denotes a vertical bicone switch with impedance $2Z$ Ω.

Before proceeding to the launching lens designs, various switch configurations are described where the geometric center of the switch cones is the first focal point. The focal impulse amplitude, $E_{\max}$, and beamwidth were compared for the following switch configurations [33].

1) *Four Feed Arms with Switch Cones (4FASC)*: A 200-Ω bicone switch, of height 1.0 cm, centered at the first focal point transitions to the feed-arms of the PSIRA. The connection between the switch cone base and the feed-arms is called the loft connection.
2) *Truncated Four Feed Arms with Switch Cones (T4FASC)*: This configuration is identical to the 4FASC except that the feed arms are truncated at a distance of 19 cm from the first focal point.

One notes that the rise time of $t_\delta = 100$ ps corresponds to a physical distance of $ct_\delta = 3$ cm (in air). Therefore, a switch of appropriate dimensions can also serve as a guiding structure. The following two such configurations were studied.

1) *Vertical Bicone Switch (VBCS)*: A vertical bicone is used as the source where the height of each cone is 6.0 cm. This structure also serves to guide the spherical TEM waves originating from the feed point. The impedance of the cones was varied.
2) *Slanted Four-Cone Feed Arms (S4CFA)*: This structure is almost identical to the T4FASC, except that the feed arms are replaced by 200-Ω cones. Each cone is 6.0 cm in height.

Results from numerical simulations for $E_{\max}$ and the spot size, at the second focal point, for the various configurations are summarized in Table II.

One finds the VBCS-75 and T4FASC designs to be the most promising. Both these configurations are easy to fabricate, yield a relatively high peak electric field and an acceptable spot size compared to the other configurations in Table II. Additionally, it is also found that the pre-pulse is shorter with these structures, compared to those in [10]. Therefore, these configurations are further considered for the launching lens designs in Section V.

C. PV Designs

The gas chamber, PV, and launching lens are necessary as, in the final experimental realization of the PSIRA, 100 kV or more will be applied across the switch gap. The gas chamber typically contains hydrogen or SF_6 under high pressure. In this paper, hydrogen is used as an example. As mentioned in Section IV-B, the location of the geometric center of the switch cones at the first focal point greatly simplifies the design. The design

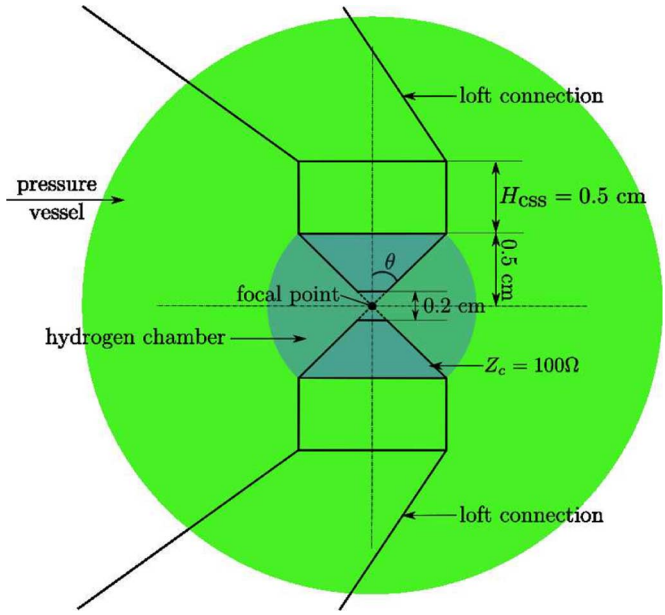

Fig. 11. Side view of the T4FASC configuration with a spherical PV and spherical HC.

TABLE III
DIMENSIONS OF SWITCH SYSTEM COMPONENTS FOR THE T4FASC-SPV DESIGN

Component	Height (cm)	Radius (cm)
switch cone	$h = 0.5$	0.51
cylindrical support	$H_{\text{CSS}} = 0.5$	0.51
hydrogen chamber	–	0.71
pressure vessel	–	$r_{\text{PV}} = 2.0$
oil medium	–	$r_{\text{oil}} = 5.0$

is further simplified if one considers the PV to serve the function of the lens. The switch system then consists of only three components, which are: 1) switch cones and guiding structures; 2) HC; and 3) PV.

The PV may be cylindrical or spherical. The peak focal impulse amplitudes of the VBCS-75 configurations, with a spherical PV, were approximately 30% lower than the corresponding T4FASC designs. Therefore, numerical simulation results for only the T4FASC configuration with the spherical and cylindrical PV designs are presented here [34], [35].

1) T4FASC With a Spherical PV (T4FASC-SPV): To provide structural support to the PV, a cylindrical support section (CSS), of height H_{CSS}, is added to the T4FASC design. The PV and HC are spherical. The relative permittivity of the PV medium is assumed to be 3.7. The impedance of the switch cones is 200 Ω in the PV medium, i.e., half-angle $\theta = 45.58°$. A spherical container, with $\epsilon_r = 2.25$ (transformer oil), surrounds the PV and is used to denote the oil "bath" that would be used in the final practical design. Fig. 11 shows the side view of the various components of the switch system. Dimensions of these components are summarized in Table III.

Probes to monitor the time-of-arrival of electric fields were placed on a (virtual) sphere of radius 10 cm (near field). The normalized responses from these probes are shown in Fig. 12

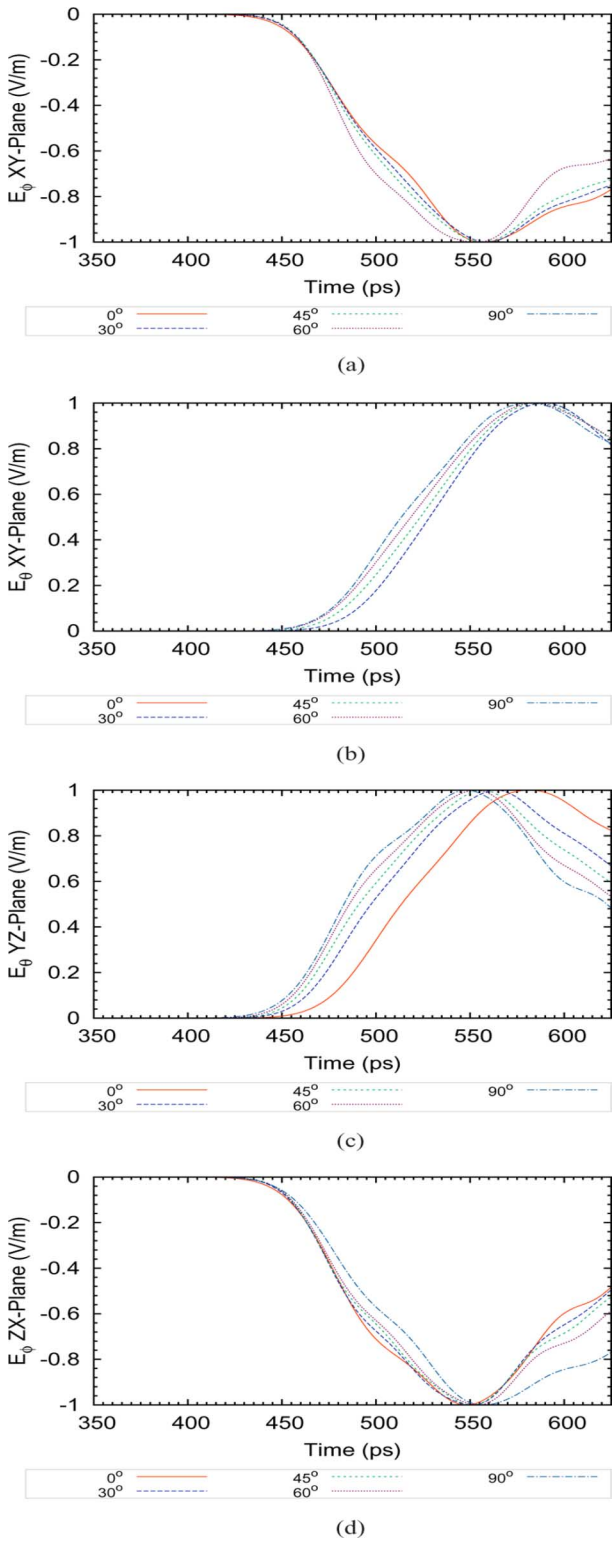

Fig. 12. Normalized E_θ and E_ϕ components of the responses from the electric field probes on the xy–, $-yz$-, and $-zx$-planes for the T4FASC-SPV configuration. (a) Normalized E_ϕ in the xy-plane (b) Normalized E_θ in the xy-plaen (c) Normalized E_θ in the $-yz$-plane (d) Normalized E_ϕ in the $-zx$-plane.

(each response is normalized with respect to its maximum). The E_ϕ component in the $-yz$-plane and the E_θ component in the $-zx$-plane are 0. The time spread in the electric fields is less than 20 ps, which is within the acceptable tolerance.

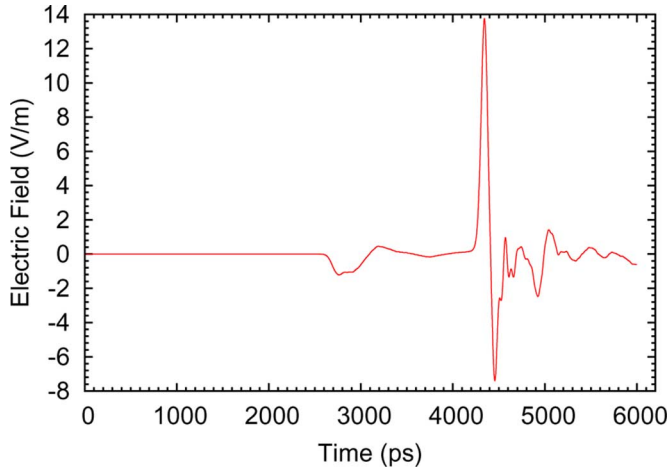

Fig. 13. Electric field focal impulse waveform for the T4FASC-SPV configuration.

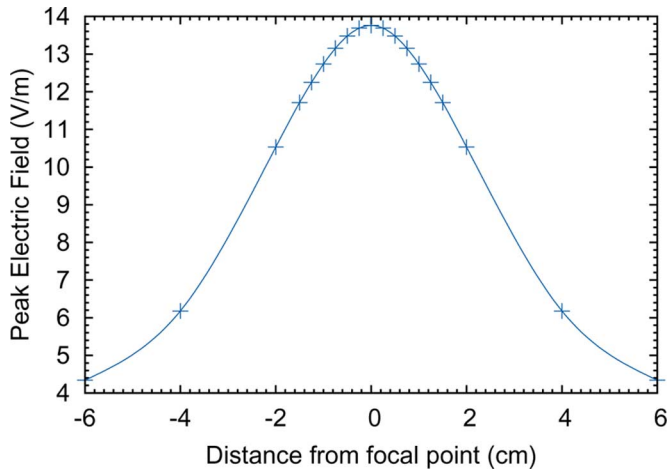

Fig. 14. Spot size for the T4FASC-SPV configuration.

The focal waveform and spot size are shown in Figs. 13 and 14. These results indicate that the electric field is enhanced, compared to the T4FASC configuration in Table III, with the PV by approximately 91%, $E_{\max} = 13.76$ V/m, with a corresponding increase of only 19% in the spot diameter, beamwidth $= 4.64$ cm. The electric field is enhanced due propagation through the PV dielectric medium.

2) T4FASC With a Cylindrical PV (T4FASC-CPV): Analytical calculations using optical approximations for a T4FASC configuration with a cylindrical PV and cylindrical HC are detailed in [36]. It is shown that for a given relative permittivity, radius, and height of the PV, the surrounding oil medium can be used as the launching lens. Fig. 15 shows the side view of the various components of the switch system.

The dimensions of the components are summarized in Table IV. The radius and height of the PV are determined using the formulas in [36] for $r_{hc} = h\tan\theta = 0.5\tan(45.58°) = 0.51$ cm and $\epsilon_{r_{ll}} = 2.25$; $\epsilon_{r_{ll}}$ is the relative permittivity of the launching lens. Note that $h_{\text{pv}} = h + H_{\text{css}}$ in Table IV.

The time-of-arrival of the electric fields on probes placed on a spherical surface, of radius 10 cm, showed a time spread similar to that of the T4FASC-SPV, i.e., less than 20 ps. The focal

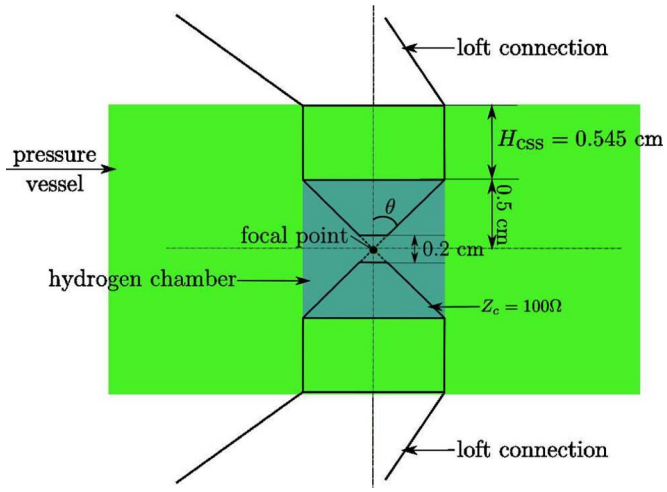

Fig. 15. Side view of the T4FASC configuration with a cylindrical PV and cylindrical HC.

TABLE IV
DIMENSIONS OF SWITCH SYSTEM COMPONENTS FOR THE T4FASC-CPV DESIGN

Component	Height (cm)	Radius (cm)
switch cone	$h = 0.5$	0.51
cylindrical support	$H_{\rm css} = 0.545$	0.51
hydrogen chamber	$h_{\rm hc} = 1.0$	0.51
pressure vessel	$h_{\rm pv} = 1.045$	$r_{\rm pv} = 1.905$
oil medium	–	$r_{\rm oil} = 5.0$

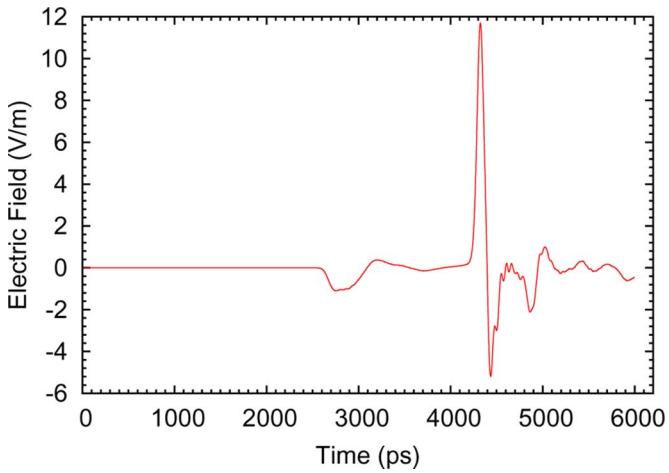

Fig. 16. Electric field focal impulse waveform for the T4FASC-CPV configuration.

waveform and spot size are shown in Figs. 16 and 17. These results indicate that the electric field is enhanced, compared to the T4FASC configuration in Table IV, with the PV by approximately 62%, $E_{\max} = 11.7$ V/m. The corresponding increase in the spot diameter is only 18%, beamwidth $= 4.95$ cm. Although $E_{\max}$ is less than T4FASC-SPV, the T4FASC-CPV configuration is attractive since it is easier to fabricate.

Various components of the switch and PV design were optimized so that a large peak electric field, with a small spot size, was obtained. For the spherical PV configuration, the following ranges yield a reasonable electric field amplification:

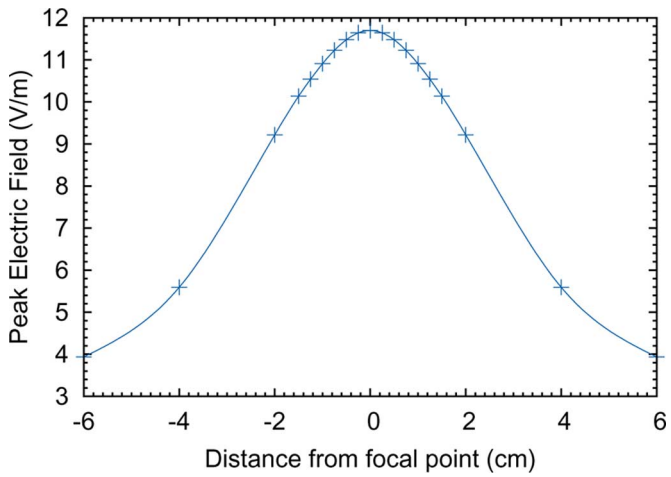

Fig. 17. Spot size for the T4FASC-CPV configuration.

- feed arm length: 18 cm $\leq l \leq$ 22 cm;
- height of cylindrical support structure: 0.2 cm $\leq H_{\rm css} \leq$ 0.6 cm;
- PV radius: 1.50 cm $\leq r_{\rm pv} \leq$ 3.0 cm.

The height and radius of the PV for the cylindrical PV design are fixed by the formulas in [36]. The range of the feed arm length, l, for the T4FASC-CPV configuration is identical to the T4FASC-SPV design.

V. DISCUSSION

The design of the PSIRA, with the focusing lens and switch system, presented above is conceptually complete. The system can deliver <200-ps pulses with a spot area of approximately 2 cm^2, which is adequate for biological applications. However, there remain two major technological challenges before a prototype device can be field-tested.

The first concerns the dielectric materials used in the focusing lens. As observed in Section III, the amplitude of the impulse is reduced, and the beamwidth increased, due to losses occurring in the lens materials. It is also observed that the lens filters frequencies above 5 GHz. Therefore, materials with less losses and a better frequency response, from 0 to 10 GHz, must be explored.

The second hurdle pertains to high-frequency switching. Numerical simulations used in the design of the switch system in Section IV do not consider the physics of gas discharges. For the switch designs considered, current technology limits the repetition rate to a few hundred hertz. Higher frequencies, of the order of a few kilohertz, are required to induce apoptosis in cells. Hence, techniques to increase the frequency of switch discharges must be investigated.

VI. CONCLUDING REMARKS

This paper has reviewed the design of a prolate-spheroidal impulse-radiating hyperband antenna to concentrate 100-ps pulses onto biological targets. The design of a graded five-layer focusing lens system, to better match the pulses from air into the target medium, has been outlined. Experimental results with the PSIRA and lens system agree well with those obtained

from numerical simulations. It has been shown that the focusing lens acts as a bandpass filter. The design and numerical simulations of a switch system have been presented. Spherical (T4FASC-SPV) and cylindrical (T4FASC-CPV) PV designs have been shown to yield an enhanced focal impulse with less than 20-ps distortion in the spherical wave originating from the first focal point.

REFERENCES

[1] K. H. Schoenbach, B. Hargrave, R. P. Joshi, J. F. Kolb, C. Osgood, R. Nuccitelli, A. Pakhomov, R. J. Swanson, M. Stacey, J. A. White, S. Xiao, J. Zhang, S. J. Beebe, P. F. Blackmore, and E. S. Buescher, "Bioelectric effects of intense nanosecond pulses," *IEEE Trans. Dielect. Electr. Insul.*, vol. 14, no. 5, pp. 1088–1119, Oct. 2007.

[2] J. Zhang, P. F. Blackmore, B. Y. Hargrave, S. Xiao, S. J. Beebe, and K. H. Schoenbach, "Nanosecond pulse electric field (nanopulse): A novel non-ligand agonist for platelet activation," *Arch. Biochem. Biophys.*, vol. 471, pp. 240–248, Mar. 2008.

[3] R. Nuccitelli, U. Pliquett, X. Chen, W. Ford, R. J. Swanson, S. J. Beebe, J. F. Kolb, and K. H. Schoenbach, "Nanosecond pulse electric fields cause melanomas to self-destruct," *Biochem. Biophys. Res. Commun.*, vol. 343, pp. 351–351, 2006.

[4] K. H. Schoenbach, C. E. Baum, R. P. Joshi, and S. J. Beebe, "A scaling law for membrane permeabilization with nanopulses," *IEEE Trans. Dielect. Electr. Insul. (Special Issue)*, vol. 16, no. 5, pp. 1224–1235, Oct. 2009.

[5] K. H. Schoenbach, S. Xiao, R. P. Joshi, J. T. Camp, T. Heeren, J. F. Kolb, and S. J. Beebe, "The effect of intense subnanaosecond electrical pulses on biological cells," *IEEE Trans. Plasma Sci.*, vol. 36, no. 2, pp. 414–422, Apr. 2008.

[6] S. Xiao, S. Guo, J. T. Camp, N. Vasyl, A. Pakhomov, R. Heller, and K. H. Schoenbach, "Biological cells response to high power electromagnetic pulses," in *IEEE Int. Power Modulator and High Voltage Conf.*, May 2010, Invited Talk, Session 9O1/2.

[7] C. E. Baum, "Focal waveform of a prolate-spheroidal impulse-radiating antenna," *Radio Sci.*, vol. 42, 2007, Art. ID RS6S27.

[8] S. Xiao, S. Altunc, P. Kumar, C. E. Baum, and K. H. Schoenbach, "A reflector antenna for focusing in the near field," *IEEE Antennas Wireless Propag. Lett.*, vol. 9, pp. 12–15, 2010.

[9] S. Altunc, C. E. Baum, C. G. Christodoulou, E. Schamiloglu, and C. J. Buchenauer, "Design of a special dielectric lens for concentrating a subnanosecond electromagnetic pulse on a biological target," *IEEE Trans. Dielect. Electr. Insul.*, vol. 16, no. 5, pp. 1364–1375, Oct. 2009.

[10] P. Kumar, S. Altunc, C. E. Baum, C. G. Christodoulou, E. Schamiloglu, and C. J. Buchenauer, "Radially inhomogeneous spherical dielectric lens for matching 100 ps pulses into biological targets," *IEEE Trans. Plasma Sci. (Special Issue)*, vol. 38, no. 8, pp. 1915–1927, Aug. 2010.

[11] K. H. Schoenbach, R. P. Joshi, J. F. Kolb, N. Chen, M. Stacey, P. F. Blackmore, E. S. Buescher, and S. J. Beebe, "Ultrashort electric pulses open a new gateway into biological cells," *Proc. IEEE*, vol. 92, no. 7, pp. 1122–1137, Jul. 2004.

[12] D. V. Giri and F. M. Tesche, "Classification of intentional electromagnetic environments (IEME)," *IEEE Trans. Electromagn. Compat.*, vol. 46, no. 3, pp. 322–328, Aug. 2004.

[13] "Electromagnetic compatibility (EMC)—Part 2–13: Environment—High-power electromagnetic (HPEM) environments—Radiated and conducted," Int. Electrotech. Commission, Geneva, Switzerland, Mar. 2005.

[14] C. E. Baum, D. V. Giri, and E. G. Farr, "John Kraus antenna award," *IEEE Antennas Propag. Mag.*, no. 3, pp. 101–102, Jun. 2006.

[15] S. Altunc, C. E. Baum, C. G. Christodoulou, E. Schamiloglu, and G. Buchenauer, "Focal waveforms for various source waveforms driving a prolate-spheroidal impulse radiating antenna," *Radio Sci.*, vol. 43, Feb. 2008, Art. ID RS003775.

[16] S. Altunc, "Focal waveform of a prolate-spheroidal impulse radiating antenna (IRA)," Ph.D. dissertation, Dept. Elect. Comput. Eng., Univ. New Mexico, Albuquerque, NM, 2007.

[17] C. E. Baum, "Focal waveform of a prolate-spheroidal IRA," in *Sens. Simulation*, Feb. 2006, Note 509.

[18] C. E. Baum, "Addition of a lens before the second focus of a prolate-spheroidal IRA," in *Sens. Simulation*, Apr. 2006, Note 512.

[19] C. E. Baum, S. Altunc, and P. Kumar, "Scaling relationships for electromagnetic parameters for focusing graded dielectric lenses," in *Sens. Simulation*, Apr. 2009, Note 537.

[20] C. E. Baum, S. Altunc, K. H. Schoenbach, and S. Xiao, "Focusing an electromagnetic implosion inside tissue," in *Bioelectric*, Oct. 2008, Note 3.

[21] P. Kumar, S. Altunc, C. E. Baum, C. G. Christodoulou, and E. Schamiloglu, "Experimental results for the focal waveform and beam width in air with a 100 ps filter," in *EM Implosion*, Jul. 2010, Memo 50.

[22] C. E. Baum, *Electromagnetic Sensors and Measurement Techniques*, J. E. Thompson and L. H. Luessen, Eds. Dordrecht, The Netherlands: Martinus Nijhoff, 1986, ch. Fast Electrical and Optical Measurements, pp. 73–144.

[23] C. E. Baum, "Accuracy considerations in the design of B-Dot and I-Dot sensors," in *Sens. Simulation*, Jun. 1992, Note 344.

[24] C. E. Baum, "Tiny fast-pulse B-Dot and D-Dot sensors in dielectric media," in *Sens. Simulation*, Jun. 2009, Note 544.

[25] P. Kumar, S. Altunc, C. E. Baum, C. G. Christodoulou, and E. Schamiloglu, "Experimental results for the focal waveform and beam width in the focusing lens with a 100 ps filter," in *EM Implosion*, Jul. 2010, Memo 51.

[26] D. V. Giri, J. M. Lehr, W. D. Prather, C. E. Baum, and R. J. Torres, "Intermediate and far fields of a reflector antenna energized by a hydrogen spark-gap switched pulser," *IEEE Trans. Plasma Sci.*, vol. 28, no. 5, pp. 1631–1636, Oct. 2000.

[27] C. E. Baum, E. G. Farr, and D. Giri, *Review of Impulse-Radiating Antennas*, W. R. Stone, Ed. New York: Oxford Univ. Press, 1996–1999, ch. Review of Radio Science, pp. 403–439.

[28] S. Altunc, C. E. Baum, C. G. Christodoulou, and E. Schamiloglu, "Analytical calculations of a lens for launching a spherical TEM wave," in *Sens. Simulation*, Oct. 2008, Note 534.

[29] P. Kumar, S. Altunc, C. E. Baum, C. G. Christodoulou, and E. Schamiloglu, "Analytical considerations for curve defaining boundary of a non-uniform launching lens," in *EM Implosion*, Jun. 2009, Memo 26.

[30] P. Kumar, S. Altunc, C. E. Baum, C. G. Christodoulou, and E. Schamiloglu, "Simulation results for 3-layer and 6-layer planar non-uniform launching lens," in *EM Implosion*, Jun. 2009, Memo 27.

[31] P. Kumar, S. Altunc, C. E. Baum, C. G. Christodoulou, and E. Schamiloglu, "Derivation of the dielectric constant as a function of angle for designing a conical non-uniform launching lens," in *EM Implosion*, Jun. 2009, Memo 28.

[32] P. Kumar, S. Altunc, C. E. Baum, C. G. Christodoulou, and E. Schamiloglu, "Simulation results for 6-layer and 7-layer conical non-uniform launching lens," in *EM Implosion*, Jun. 2009, Memo 29.

[33] P. Kumar, S. Altunc, C. E. Baum, C. G. Christodoulou, and E. Schamiloglu, "Investigation of various switch configurations," in *EM Implosion*, Feb. 2010, Memo 39.

[34] P. Kumar, S. Altunc, C. E. Baum, C. G. Christodoulou, and E. Schamiloglu, "The truncated four feed-arm configuration with switch cones (T4FASC) and a spherical pressure vessel," in *EM Implosion*, May 2010, Memo 42.

[35] P. Kumar, S. Altunc, C. E. Baum, C. G. Christodoulou, and E. Schamiloglu, "150 Ω impedance-matched bicone switch configuration with a spherical pressure vessel," in *EM Implosion*, May 2010, Memo 43.

[36] P. Kumar, S. Altunc, C. E. Baum, C. G. Christodoulou, and E. Schamiloglu, "Design considerations for a cylindrical pressure vessel with a spherical launching lens," in *EM Implosion*, Mar. 2010, Memo 41.

Prashanth Kumar (M'07) received the B.E. degree in Eelectrical and eectronics engineering from the University of Madras, Madras, India, in 2003, the Masters degree from the University of New Mexico (UNM), Albuquerque, in 2007, and is currently working toward the Ph.D. degree at UNM.

Since March 2009, he has been with the Transient Antenna Measurement Laboratory, UNM, where he is currently involved with electromagnetic lens and switch designs for the prolate-spheroidal impulse-radiating antenna. He is also involved with terahertz antenna designs for secure communications.

Carl E. Baum (S'62–M'63–SM'78–F'84–LF'06) was born in Binghamton, NY, on February 6, 1940. He received the B.S. (with honors), M.S., and Ph.D. degrees in electrical engineering from the California Institute of Technology, Pasadena, in 1962, 1963, and 1969, respectively, and the Dr.Ing.E.h. degree (*honoris causa*) from the Otto von Guericke University, Magdeburg, Germany, in 2004.

From 1963 to 1967 and from 1968 to 1971, he was stationed at the Air Force Research Laboratory, Directed Energy Directorate (formerly Phillips Laboratory, which is formerly the Air Force Weapons Laboratory), Kirtland AFB, Albuquerque, NM. From 1971 to 2005, he had served as a civil servant as a Senior Scientist with the Air Force Research Laboratory. Since 2005, he has been a Distinguished Research Professor with the Department of Electrical and Computer Engineering, University of New Mexico, Albuquerque. He is the Editor of several interagency note series on electromagnetic pulse (EMP) and related subjects. He is the founder and President of the SUMMA Foundation, which sponsors various electromagnetics-related activities including scientific conferences, publications, short courses, fellowships, and awards. He has led EMP and HPE short courses at numerous locations around the globe.

Dr. Baum is a member of Commissions A, B, and E of the U.S. National Committee, International Union of Radio Science. He was the recipient of the Air Force Research and Development Award (1970), the AFSC Harold Brown Award (1990), the Air Force Research Laboratory Fellow (1996), the Richard R. Stoddart Award of the IEEE Electromagnetic Compatibility (EMC) Society (1984), the John Kraus Antenna Award of the IEEE Antennas and Propagation Society (2006), the Harry Diamond Memorial Award (1987), and the IEEE Electromagnetics Field Award (2007).

Serhat Altunc (M'07) received the B.S. degree in electrical and electronics engineering from Istanbul Technical University, Istanbul, Turkey, in 2000, the M.S. degree in communication engineering from Yildiz Technical University, Istanbul, Turkey, in 2003, and the Ph.D. degree in electrical engineering from the University of New Mexico (UNM), Albuquerque, in 2007.

From 2001 to 2003, he was a Teaching Assistant with Yildiz Technical University. He is currently a Postdoctoral Fellow with UNM, where since August 2004, he has been with the Transient Antenna Measurement Laboratory. He is currently involved with IRAs, ultra-wideband (UWB) antenna design, and the applications of UWB antennas.

Jerald Buchenauer (M'70) received the A.B. degree in physics from Franklin and Marshall College, Lancaster, PA, in 1962, and the Ph.D. degree in solid-state physics from Cornell University, Ithaca, NY, in 1970.

He was a Postdoctoral Research Associate with Brown University and the University of Utah, where he conducted research on inelastic light scattering in solids. In 1974, he joined the Idaho National Engineering Laboratory, Idaho Falls, ID, as a Senior Research Engineer, involved with fission reactor diagnostic measurements. He had been a Technical Staff Member with the Los Alamos National Laboratory, Los Alamos, NM, where from 1975 to 2006, he was involved with controlled thermonuclear research programs, optics, and electromagnetic phenomenology. From 1991 to 1998, he was also an Intergovernmental Personnel Act (IPA) employee with the Air Force Research Laboratory, Albuquerque, NM, where he conducted research on time-domain antennas and sensors and pulsed power phenomena. Since 2003, he has also been a member of the faculty with the University of New Mexico, Albuquerque, as a Research Professor, where he is involved with the Compact Pulsed Power Multidisciplinary University Research Initiative Program.

Shu Xiao (M'04) received the Ph.D. degree in electrical engineering from Old Dominion University, Norfolk, VA, in 2004.

From 1996 to 2001, he partcipated in the Ph.D./Master joint program of the University of Electronic Sciences and Technology of China, Sichuan, China. His research interests include pulsed power, high power electromagnetics, and electrical discharges in liquids and gases. He is currently an Assistant Professor with the Department of Electrical and Computer Engineering, Old Dominion University. He is also with the Frank Reidy Research Center for Bioelectrics, where he uses pulsed power and pulsed electromagnetic radiation in both biological and imaging applications.

Dr. Xiao was a guest editor for a special issue of the IEEE TRANSACTIONS ON PLASMA SCIENCE.

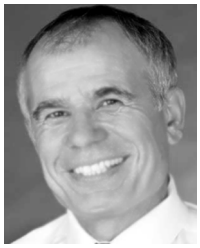

Christos G. Christodoulou (S'80–M'84–SM'90–F'02) received the Ph.D. degree in electrical engineering from North Carolina State University, Raleigh, in 1985.

He is currently an Intergovernmental Personnel Act (IPA) employee with the Air Force Philips Laboratory, Kirtland, NM, the Director of the Aerospace Institute, University of New Mexico, Albuquerque, and the Chief Research Officer for the Configurable Space Microsystems Innovations and Applications Center (COSMIAC). He has authored or coauthored over 370 papers in journals and conferences and 12 book chapters. He coauthored four books. He has been an Associate Editor with the *International Journal of Signal and Imaging Systems Engineering* and the *Journal of RF and Microwave Computer-Aided Engineering*. His research interests are in the areas of cognitive radio, reconfigurable systems, machine learning, and smart RF/photonics.

Dr. Christodoulou is a member of the U.S. National Committee Commission B, URSI. He was the general chair of the IEEE Antennas and Propagation Society (IEEE AP-S)/URSI 1999 Symposium, Orlando, FL. He was appointed as an IEEE AP-S Distinguished Lecturer (2007-present). He has served as an associate editor for the IEEE TRANSACTIONS ON ANTENNAS AND PROPAGATION and IEEE ANTENNAS AND WIRELESS PROPAGATION LETTERS. He was a member of the Board of Directors for the Global Wireless Education Consortium (GWEC) (2002–2006). He was the recipient of the 2010 IEEE John Krauss Antenna Award for his work on reconfigurable fractal antennas using microelectromechanical systems (MEMS) switches, the Lawton-Ellis Award, and the Gardner Zemke Professorship of the University of New Mexico.

Edl Schamiloglu (M'90–SM'95–F'02) received the B.S. and M.S. degrees from the School of Engineering and Applied Science, Columbia University, New York, NY, in 1979 and 1981, respectively, and the Ph.D. degree in applied physics (with a minor in mathematics) from Cornell University, Ithaca, NY, in 1988.

In Summer 1990, he was a Lecturer with the U.S. Particle Accelerator School (USPAS), Harvard University, Cambridge, MA. In Summer 1997, he lectured at the USPAS, Massachusetts Institute of Technology (MIT), Cambridge. He was an Assistant Professor of electrical and computer engineering with the University of New Mexico (UNM), Albuquerque, in 1988, where he is currently a Professor with the Department of Electrical and Computer Engineering and directs the Pulsed Power, Beams, and Microwaves Laboratory. He has authored or coauthored 60 refereed journal papers and over 100 reviewed conference papers. He holds three patents. He co-edited *Advances in High-Power Microwave Sources and Technologies* (IEEE Press, 2001), and is currently coauthoring *High Power Microwaves, 2nd Ed.* (IOP, 2006). His research interests are in the physics and technology of charged-particle beam generation and propagation, high-power microwave sources, plasma physics and diagnostics, electromagnetic-wave propagation, pulsed power, and infrastructure surety.

Dr. Schamiloglu is a member of the American Physical Society and the American Society for Engineering Education (ASEE). He is an associate editor of the IEEE TRANSACTIONS ON PLASMA SCIENCE. He was the recipient of the Sandia

National Laboratories Research Excellence Award (1991) and the UNM School of Engineering Research Excellence Award (twice; the junior faculty in 1992 and senior faculty in 2001). He was bestowed the title of UNM Regents' Lecturer in 1996.

Karl H. Schoenbach (F'94) received the Diploma degree in physics and Dr. rer. nat. degree in physics from the Technische Hochschule Darmstadt (THD), Darmstadt, Germany, in 1966 and 1970, respectively.

From 1970 to 1978, he was with the THD, involved in the areas of high-pressure gas discharge physics and on the dense plasma focus. From 1979 to 1985, he held a faculty position with Texas Tech University, where he was involved in research on fast opening switches, especially electron-beam and laser-controlled diffuse discharge opening switches. In 1985, he joined Old Dominion University, Norfolk, VA. He served as Director of the Frank Reidy Research Center for Bioelectrics from 2002 to 2008, and held an Endowed Chair, the Batten Chair in Bioelectric Engineering from 2005 until his retirement in 2010. He has authored or coauthored over 400 papers in refereed journals and in conference proceedings. He holds 15 patents. He coedited *Low Temperature Plasma Physics* (Wiley-VCH, 2001 and 2007, 2nd ed.) and *Non-Equilibrium Air Plasmas at Atmospheric Pressure (Series in Plasma Physics)* (IOP, 2005). He was active in research on photoconductive and electron-beam controlled switches until 1993, and has since concentrated his research efforts on high-pressure glow discharges, particularly microdischarges, on glow (streamer) discharges in liquids, and on environmental and medical applications of pulse power technology. He continues to be actively involved in bioelectrics research, particularly in research on bioelectric effects of intense subnanosecond pulses and high-power microwaves.

Dr. Schoenbach chaired a number of workshops and conferences, among them the 1991 IEEE International Conference on Plasma Science, and the First International Symposium on Nonthermal Medial/Biological Treatments Using Electromagnetic Fields and Ionized Gases (ElectroMed99) in 1999. He has been an associate editor of the IEEE TRANSACTIONS ON PLASMA SCIENCE since 1989, guest editor of the IEEE TRANSACTIONS ON ELECTRON DEVICES (1990), the IEEE TRANSACTIONS ON PLASMA SCIENCE (1999), and the IEEE TRANSACTIONS ON DIELECTRICS AND ELECTRICAL INSULATION (2003). He was the recipient of the High Voltage Award (2000) sponsored by the IEEE Dielectric and Electrical Insulation Society, the Peter Haas Pulsed Power Award (2007), and the Frank Reidy Bioelectrics Award (2010).

Subnanosecond Electric Pulses Cause Membrane Permeabilization and Cell Death

Shu Xiao*, Siqi Guo, Vasyl Nesin, Richard Heller, and Karl H. Schoenbach

***Abstract*—Subnanosecond electric pulses (200 ps) at electric field intensities on the order of 20 kV/cm cause the death of B16.F10 murine melanoma cells when applied for minutes with a pulse repetition rate of 10 kHz. The lethal effect of the ultrashort pulses is found to be caused by a combination of thermal effects and electrical effects. Studies on the cellular level show increased transport across the membrane at much lower exposure times or number of pulses. Exposed to 2000 pulses, NG108 cells exhibit an increase in membrane conductance, but only allow transmembrane currents to flow, if the medium is positively biased with respect to the cell interior. This means that the cell membrane behaves like a rectifying diode. This increase in membrane conductance is a nonthermal process, since the temperature rise due to the pulsing is negligible.**

***Index Terms*—Cell death, current rectifying, permeabilization, pulsed electric field, subnanosecond pulses.**

I. Introduction

INTENSE electrical pulses with durations of microseconds to milliseconds are known to cause electroporation [1]–[7]. The pulses charge the membrane and cause an increase in transmembrane voltage from 250 mV to 1 V [8], at which point membrane permeabilization or pore formation sets in. This pore formation allows delivery of drugs or genes into the cell. If the pores close after the pulses, the process is known as reversible electroporation. Direct cell killing can also be achieved with pulses of the same duration but of higher amplitude, referred to as irreversible electroporation [9]. However, when shorter pulses are applied, with durations in the submicrosecond range, internal effects have been observed without permanent damage to the cell membrane (intracellular electromanipulation) [10]. The effects include internal calcium bursts [11], [12], permeabilization of internal granules [13], and control of cell death through apoptosis. The transition from electroporation to intracellular electromanipulation occurs for pulse durations, which are on the order of the charging time constant of a cell membrane, which is approximately 100 ns for mammalian cells. Yet, the duration of the pulses is not the only criterion for the onset of electroporation or intracellular electroporation. The peak electric field strength is important too. For example, nanosecond pulses with high intensity and fast rise time can also cause membrane effects, such as membrane permeabilization [14], [15], nanometer-sized pore formation [16], and phosphatidylserine (PS) externalization [17]. In fact, increasing the number of nanosecond pulses can cause the permeabilization of the membranes of endocytotic vesicles as well as the plasma membrane [18]. Nonetheless, one could still expect that the shorter the pulse duration is, the higher the likelihood that the pulses can interact with the cell internal organelles is. For subnanosecond pulses, the probability of penetrating into the interior of the cell is even higher than for nanosecond pulses [19]. In this case, the electric field distribution is determined by the dielectric permittivity rather than the resistivity of cell components [20].

There are two reasons to enter the subnanosecond range of pulse electric fields. The first is that for extremely short pulses, the electric field acts directly on membrane proteins, rather than causing charging of the membrane, and, if sufficiently strong, may cause direct and instant conformational changes. A model analysis [21] has shown that subnanosecond pulses can perforate a cell membrane. In addition, subnanosecond pulses (800 ps) have been shown to cause B16 cells to increase trypan blue uptake [20], which is a clear indication of the disruption of membrane integrity. The second reason is that subnanosecond pulses may allow us to use an impulse antenna [22], [23] to deliver such pulses for noninvasive treatment of deep lesions. The preferred pulse duration for subnanosecond pulses is in the range of 100–200 ps, making it possible to focus the radiation on the target efficiently and produce a focal spot of 1-cm size in the tissue.

In this paper, we present a study of cell responses to 200 ps (70% peak width). The biological cell response to such short pulses has not been investigated to the best of our knowledge. Cell survival for different pulse numbers was assessed with the water soluble tetrazolium (WST) assay, 18 h after exposure. The membrane transport process immediately after exposure was studied using patch clamp. Our goal was to assess the primary response of the cell membrane within 1 min after the exposure, as well as to evaluate the cell death 18 h after the exposure.

II. Materials and Methods

Two types of cells were studied: B16.F10 murine melanoma cells (ATCC CRL-6322) and NG108 neuroblastoma-glioma hybrid cells (ATCC HB-12317). B16 cells were used for the cell survival study. NG108 cells have voltage-gated (VG) sodium

Manuscript received September 10, 2010; revised November 26, 2010, and January 17, 2011; accepted January 26, 2011. Date of publication February 7, 2011; date of current version April 20, 2011. This work was supported by the U.S. Air Force Office of Scientific Research (AFOSR) and Bioelectrics, Inc. *Asterisk indicates corresponding author.*

*S. Xiao is with the Frank Reidy Research Center for Bioelectrics, Department of Electrical and Computer Engineering, Old Dominion University, Norfolk, VA 23529 USA (e-mail: sxiao@odu.edu).

S. Guo, V. Nesin, R. Heller, and K. H. Schoenbach are with the Frank Reidy Research Center for Bioelectrics, Old Dominion University, Norfolk, VA 23529 USA (e-mail: s2guo@odu.edu; nesin.vasyl@gmail.com; rheller@odu.edu; kschoenb@odu.edu).

Color versions of one or more of the figures in this paper are available online at http://ieeexplore.ieee.org.

Digital Object Identifier 10.1109/TBME.2011.2112360

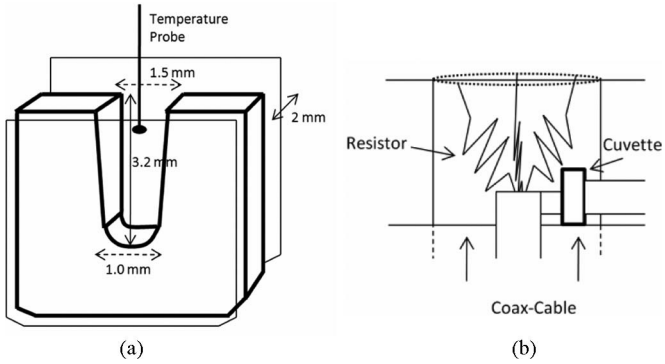

Fig. 1. Subnanosecond exposure system. (a) Cuvette with a loading volume of 6 μL. The electrodes are 70-μm-thick stainless steel foils. (b) Cuvette was placed at the end of a coax-cable (RG 217). A conical resistor array was connected in parallel with the cuvette for matching the 50-Ω coaxial, subnanosecond pulse delivery cable.

channel current that is sensitive to the electric pulses and, therefore, were used for studying the change of transmembrane conductance due to the electric pulses. The pulse conditions for B16 cell viability study were also used on NG108 cells to assess the cell death. The cells were maintained as monolayers in 90% McCoy's medium (B16) or Dulbecco's Modified Eagle's Medium without sodium pyruvate with 10% fetal bovine serum (NG108). The media ingredients were purchased from Gibco (Grand Island, NY). B16 cells were removed from flasks using a cell nonenzymatic dissociation solution (Sigma, St. Louis, MO) [24].

To evaluate the effects that subnanosecond pulses have on biological cells, we used a specially designed cuvette with plane-parallel electrodes, 2 mm apart, for cell exposure. The geometry of the cuvette is shown in Fig. 1(a). The electrodes are stainless steel foil with a thickness of 70 μm. The cuvette was loaded with 6-μL cell buffer. The reason for choosing such a small volume was to minimize the capacitance of the cuvette in order to ensure that the fast rise time of the pulse will not be slowed. The total capacitance is calculated as 1.4 pF, which allows the shortest rise time of the pulse to be 70 ps for a 50-Ω coaxial delivery system. The pulses in our experiment have a rise time of 200 ps (14%–92% pulse amplitude) and, therefore, retained their fidelity across the cuvette. The second reason was that the cuvette had to be small in order to be placed in a coaxial well [see Fig. 1(b)]. The cuvette was placed in parallel with a conical resistor array that was connected to the delivery cable from the pulse source. The conical resistor array (total value: 48.9 Ω) allows for a continuous potential distribution from the delivery cable and terminates the power flow without creating strong reflections. For a 200-ps pulse, the 1/*e* bandwidth is approximately 3 GHz. We used an HP network analyzer (HP8753E) to measure the returned loss for frequencies from 30 kHz to 3 GHz and it was found to be between -30 dB and -11dB in this range; therefore, the cuvette was well matched to the pulse delivery cable, and the reflection was minimized. The subnanosecond pulses, with an amplitude of 5 kV were generated by a pulse generator FPG 5-P (FID GmbH, Germany); therefore, the electric field was 25 kV/cm. This electric field is far less than the breakdown field of 4 MV/cm in water and 75 kV/cm in air for 20-ns-long electric pulses [25], [26]. For subnanosecond pulses, the breakdown field is even higher in both air and water than for nanosecond pulses. Therefore, we eliminate the possibility of electric breakdown inside the cuvette. During pulsing, the temperature was monitored by a fiberoptic temperature sensor (T1 C-11000 A, Neoptix, Canada) with a tip diameter $\sim$300 μm. The temperature probe was positioned on a micrometer stage and was dipped into the cell buffer from the opening of the cuvette. The sampling frequency was 2 Hz.

A separate electrode configuration was used to study the transmembrane conductance with the patch clamp technology. The pulses were delivered to cells on a cover slip on a microscope stage by a mini-coax cable (300 μm outer diameter, and 70 μm diameter of the inner conductor). The mini-coax has its end opened with the inner conductor exposed (exposed length: 350 μm). With the help of a robotic manipulator (MP-225, Sutter), the electrode was positioned above the cover slip surface, and the angle between the cover slip and the electrode was 20°. The leakage field from the inner conductor to the outer conductor provides the exposure environment for the cells. The electric field at the cell location on the cover slip between the electrodes was calculated by 3-D simulations with a finite-element Laplace equation solver Amaze 3-D (Field Precision, Albuquerque, NM). The electric field was calculated to be 20–40 kV/cm in the exposure area of 200 μm $\times$ 200 μm on the cover slip. Membrane currents were measured before exposure to subnanosecond pulses and at 10 and 20 s after it. The strong inhomogeneity of the field prevents us from exposing a large number of cells to the same electric field intensity. Therefore, this pulse system was not used for cell viability study using the WST assay.

III. Results and Discussions

A. Cell Survival After Exposure to Subnanosecond Pulses

Our previous study [20] showed that for the 800-ps pulses and an electric field of 150 kV/cm, approximately 18 000 pulses were required in order to cause 50% B-16 cell death. At the present state of antenna technology, such electric fields cannot be generated in tissues by means of wideband antennas. We, therefore, set the electric field to 25 kV/cm. Compared to the earlier study [20], both the electric field and the pulse duration were decreased considerably. It raised the question of how effective these short pulses can be in eliminating unwanted cells.

An initial assessment of B16 cell death for the 200-ps pulses at 25 kV/cm was performed under two pulse conditions, 1000 pulses (300 Hz) and 10 000 pulses (300 Hz). Using a WST assay 18 h after the pulsing, we observed no significant effect of exposure. The results were comparable to the control (in which cells were cultured in the incubator all along) and the sham exposure (when cells were loaded into the exposure cuvette, but no pulse was applied).

In order to achieve significant cell death, the number of pulses has to be increased considerably. The repetition rate also needs to be increased, as it was shown [27] that increasing the pulse repetition rate caused an increase of cell killing, even though the

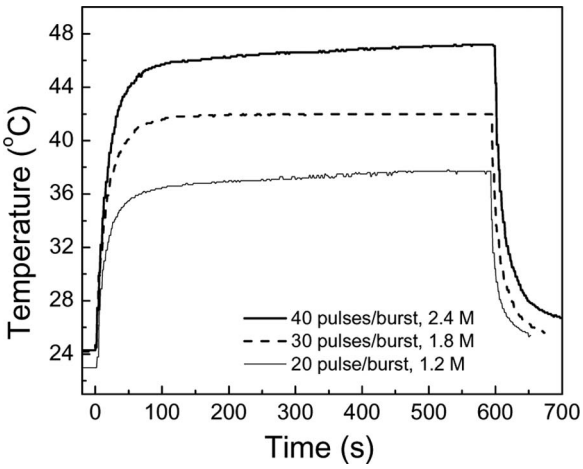

Fig. 2. Temperature increases due to the application of 1.2 M, 1.8 M, and 2.4 M pulses. Here, "M" stands for a million. The pulses were applied in the burst-mode with 20, 30, and 40 pulses/burst. The repetition rate in each burst was 10 kHz and each burst repeated every 10 ms (100 Hz). The exposure time for each of these three exposure conditions was 10 min. The starting temperature was 24 °C ± 1 °C.

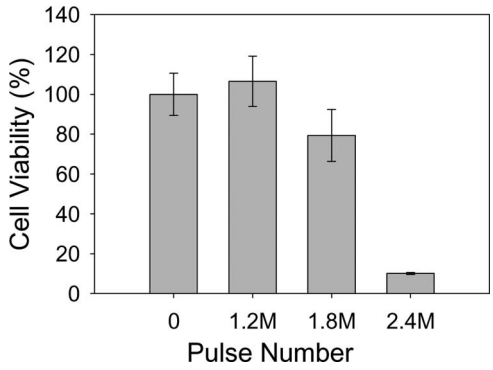

Fig. 3. Survival of B-16 cells after exposure to burst-mode pulsing. Pulse number, 0, refers to sham exposure. Pulse number 1.2 M, 1.8 M, and 2.4 M corresponds to the burst-mode exposure with 20, 30, and 40 pulses/burst. Here, "M" stands for a million. The error bars represent the standard deviation of the mean ($n = 10$ for each pulsing condition). A single factor ANOVA analysis yielded $p = 0.22$ (1.2 M pulses) and $p < 0.003$ for both 1.8 M and 2 M pulses.

applied voltage was lower than the membrane breakdown voltage. We have increased the repetition rate to 10 kHz, the maximum rate the pulse generator allowed. Thermal effects, which generally can be neglected for nanosecond and subnanosecond pulses at low repetition rates must be taken into account at high repetition rates. We have found that the pulses delivered to a cuvette at high repetition rates caused a significant increase in the temperature of the cell buffer. For a 10-min exposure at 3 kHz, a total of 1.8 million pulses, at maximum temperature of 37 °C, was measured. Results obtained at 10 kHz, showed a much higher absolute temperature (>60 °C). The exposure at the increased temperature also caused evaporation of the cell buffer and the loss of volume of the buffer, seen from the volume retrieved through a micropipette with a gel-loading tip (Fisher Scientific, PA).

Instead of applying pulses continuously, we used a burst mode to deliver the pulses. Each burst consisted of 20, 30, or 40 pulses and the burst repeated itself every 10 ms (100 Hz). The pulses in each burst had a repetition frequency of 10 kHz (100 μs between pulses). For 20, 30, and 40 pulses/burst, the total pulse numbers are 1.2, 1.8, and 2.4 million for 10-min exposure. The temperature developments are shown in Fig. 2. The starting temperature was 24 ± 1 °C. Within approximately 1 min, the temperature rose and became stable. The corresponding maximum temperature was measured as 37 °C, 41 °C, and 47 °C. We note that the temperature in Fig. 2 was measured when the temperature probe tip was just submerged in the cell buffer, less than 1 mm deep. For other positions, the maximum temperatures decreased to 34 ± 1 °C for 20 pulses/burst, 37 ± 1 °C for 30 pulses/burst, and 44 ± 1 °C for 40 pulses/burst, respectively. The higher temperature near the cell buffer surface can be explained by the electric field enhancement of the sharp edge electrodes as they are thin stainless steel (70-μm-thick) foil. The field near the surface can be estimated at 10% higher than the average field in the gap. On the other hand, for the exposure of 2.4 million pulses, the energy W required to increase the temperature of the 6-μL cell buffer for a temperature increase, $\Delta T = 23$ °C, can be estimated as 0.6 J ($\Delta W = C_v \rho \Delta T V$, $C_v = 4.2$ J/g°C, $V = 6$ μL). The overall energy W deposited in the buffer is 24 J, calculated from $W = \sigma E^2 \tau N V$, where $\sigma = 1.3$ S/m, $E = 25$ kV/cm, $\tau = 200$ ps, and $N = 2.4$ million. It is obvious that most of the energy was dissipated through the electrical contact. Fig. 3 shows the viability of B16 cells 18 h after exposure. For exposure to 1.2 million pulses at 10 kHz and 20 pulses/burst, Fig. 3 indicates a slight increase of cell survival. This, however, should not be interpreted, as a higher number of cells proliferated compared to the sham. Instead, this tells us the cells increased their mitochondrial activity and metabolic rate due to pulsing. As the pulse number increased, the number of cells that survived pulsing decreased. Approximately 20% cell death was observed for 1.8 million pulses (10 kHz and 30 pulses/burst), and 90% cell death for 2.4 million pulses (10 kHz and 40 pulses/burst). It should be noted that WST is a colorimetric assay, which measures the activity of mitochondrial enzymes. It is likely that subnanosecond pulses penetrate into the cell interior and affect the metabolic activity directly, and it is possible that the effect could occur even in viable cells. However, we observed that most of the cells treated with 2.4 million pulses were isolated and detached from the culture dish. In addition, when cell viability was assessed by adding trypan blue, there was a clear indication that most of the cells were dead. In contrast, live cells in sham conditions, which served as a control, were confluent and remained attached to the culture dish (as well as appearing viable by WST). Therefore, we think the result obtained by the WST assay is a valid means for determining cell death. In order to better understand whether the temperature rise was the cause of the observed cell death, we incubated cells in a water bath at various temperatures for 10 min. Fig. 4(a) shows the temperature profile during the 10-min water bath treatment at 42 °C when the cells were loaded into a test tube. The temperature in the tube rose to the water bath temperature in approximate 50 s, which is a similar trend as in the pulsed conditions. The survival results were again obtained from the WST assay 18 h after exposure and shown in Fig. 4(b).

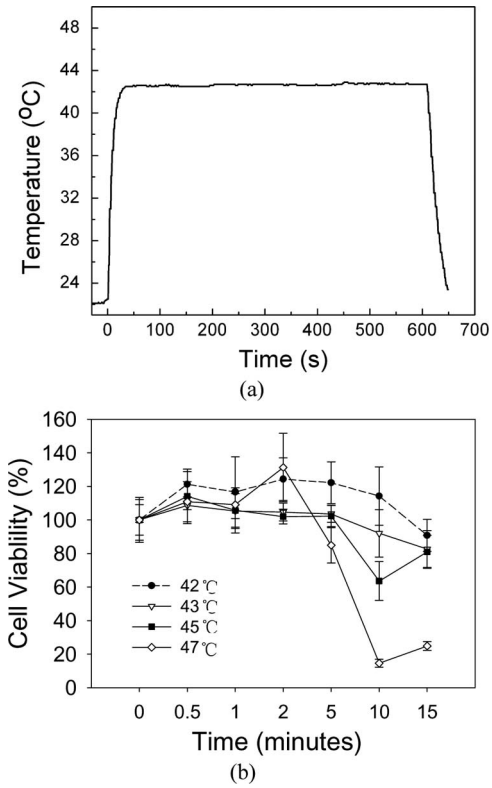

Fig. 4. Cell viability after treatment in water baths at different temperatures. (a) Temperature profile for 10-min treatment was measured in a plastic test tube loaded with 15-μL cell buffer. (b) B-16 cell survival after exposure to heating in water baths at various temperatures up to 15 min. The error bars represent the standard deviation of the mean ($n = 4$). The time does not exactly correspond to the treatment time at the water bath temperature, as the temperature in the test tube took approximately 50 s to rise. At 45 °C, the 15-min data are not significantly different from the 10-min data with $p = 0.0892$.

The cells that were exposed to 42 °C were alive, even after the 10-min exposure. However, when the water bath temperature was raised to 47 °C, almost all the cells did not survive. Recall that the temperature in the cuvette under the pulse condition of 40 pulses per burst was 44 °C –47 °C. For cells treated in the water bath at 44 °C –47 °C, we observe that cell viability could vary in the range of 20%–80% [see Fig. 4(b)]. Evidently, the heating contributed to the cell death. We, therefore, conclude that the cell death under the pulse condition of 40 pulses per burst in Fig. 3 was caused by a combination of heating and the electric field effect. However, for the pulse condition 10 kHz and 30 pulses/burst, the heating effect was minimal, as the absolute temperature was 37 °C–41 °C, which was insufficient to cause cell death, as shown in Fig. 4(b).

B. Membrane Permeabilization Caused by Subnanosecond Pulses

We have observed that subnanosecond pulses caused cell death with a significant temperature rise due to a high-repetition rate and high pulse numbers. Exposure conditions with a reduced pulse number and a negligible temperature rise appear not to induce any noticeable cell death. There are, however, other cell responses, such as a change in cell membrane conductance, which may occur due to the applied electric field, especially at the time of the exposure or right after the exposure. Under normal physiological conditions, the transmembrane conductance is primarily determined by passive transport of ions through channels. Ion channels are pore-forming proteins and they help ions move across the plasma membrane according to electrochemical gradients. The most important are two types: ligand-gated ion channels and VG channels.

In our study, we employed whole-cell patch clamp to explore the effect of subnanosecond electric pulses on the VG sodium current (VG I_{Na}) and the leak current (I_{Leak}) in neuroblastoma cells (NG-108). All experiments were carried out at room temperature (~24 °C). Whole-cell patch-clamp configuration was established 2–3 min prior to 200-ps electric pulse (psEP) application, to allow enough time for dialysis of the cytoplasm with the pipette solution. Whole-cell currents were probed by stepping the membrane potential from −100 mV to +30 mV, in 10-mV steps from the holding potential of −80 mV. The currents were recorded 10 s before psEPs, and 10 s and 30 s after the exposure. Shown in Fig. 5 are the current–voltage curves of VG I_{Na} and I_{Leak} in cells subjected to 0 (sham, $n = 4$), 1000 pulses ($n = 6$), and 2000 pulses ($n = 9$) applied at the rate of 0.5 kHz. VG I_{Na} began to activate at a potential of −40 mV, reached peak amplitude near 10 mV, and then declined as the voltage approached its equilibrium potential. No significant change of the current–voltage characteristics of VG I_{Na} was observed after 1000 pulses and even 2000 pulses [see Fig. 5(b) and (c)]. The I_{Leak} in NG-108 cells after the exposure of 1000 psEP also did not change [see Fig. 5(e)]. However, I_{Leak} in 2000 psEP-treated cells demonstrated a slight increase in voltage-sensitive inward current [see Fig. 5(f)]. It can be seen that 10 s after exposure, the I_{Leak} in the negative voltage had increased 11.1 ± 3 pA.

This increase was still observable 30 s after the exposure, but a trend of recovery, i.e., the current level returning to the control level, could be seen. In the meantime, the current flowing out of the cell did not change. This unidirectional current was most likely due to the influx of sodium ions, the major cation presented in the cell bath. Such unidirectional current flow has also been observed in the cell membrane after exposure to nanosecond electric pulses [14] and was found to be caused by pores of nanometer size formed in the cell membrane. When nanosecond pulses are used as stimuli, this process is referred to as nanoporation. Interestingly, the current-rectifying characteristic of these pores is similar to that of synthetic nanopores in polymer foils, reported to be an asymmetrical conical shape [28].

These pores, as they were created by a relatively small number of pulses, were unlikely to cause cell death, since the cell viability assessed by WST assay 18 h after the exposure of 2.4 million pulses was found to be 34% ± 2% (temperature: 42 °C–45 °C during exposure). Cell viability after exposure to 1.8 million pulses was 70% (see Fig. 6). Once the pores are formed, can they develop into bigger ones, if more pulses are applied? Can these pores become large enough to allow trypan blue molecules to enter the cell?

One hour after exposure (1.2–2.4 million pulses), the cells did not show more trypan blue uptake than the control. This

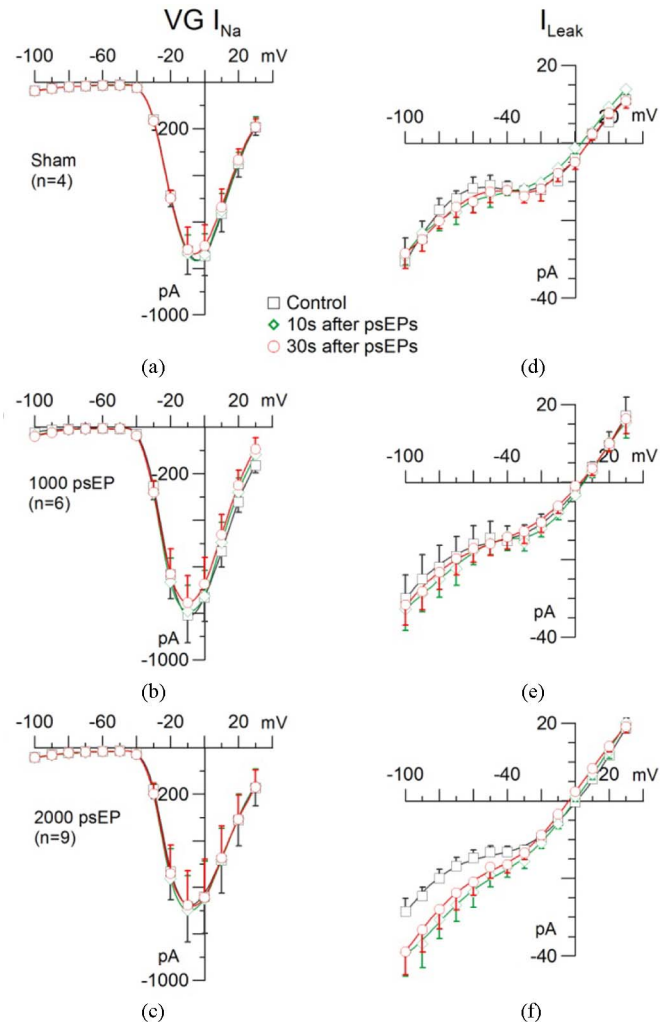

Fig. 5. Current–voltage characteristics of NG108 cell membrane before and after exposure to subnanosecond pulses. Subnanoseocnd electric pulses (psEPs) had no effect on VG I_{Na} (*left column*) but increased I_{Leak} (*right column*). The currents were recorded 10 s before psEPs (control), and 10 s and 30 s after exposure. Peak amplitude of the fast inactivating VG I_{Na} [see (a)–(c)] was measured as a negative peak during the first 15 ms of the voltage steps. I_{Leak} [see (d)–(f)] was measured at a mean current value 20–70 ms after stepping, when VG I_{Na} completely inactivated. Data are shown as the mean ± SE with $n = 4$ for sham, $n = 6$ for1000 pulses, and $n = 9$ for 2000 pulses.

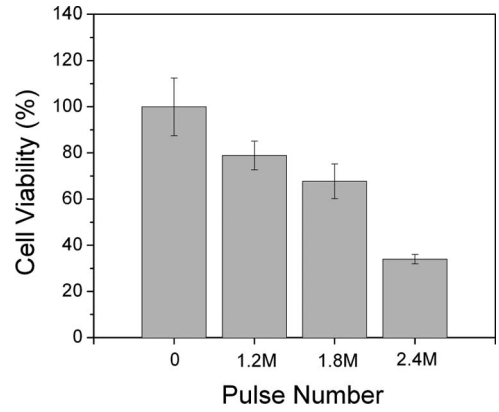

Fig. 6. Survival of NG108 cells after exposure to burst-mode pulsing using the exposure system shown in Fig. 1. Pulse number, 0, refers to sham exposure. Pulse number 1.2 M, 1.8 M, and 2.4 M corresponds to the burst-mode exposure with 20, 30, and 40 pulses/burst. Here, "M" stands for a million. The error bars represent the standard deviation of the mean ($n = 4$ for each pulsing condition). The maximum temperatures were 34 °C (20 pulses/burst), 38 °C (30 pulses/burst), and 45 °C (40 pulses/burst).

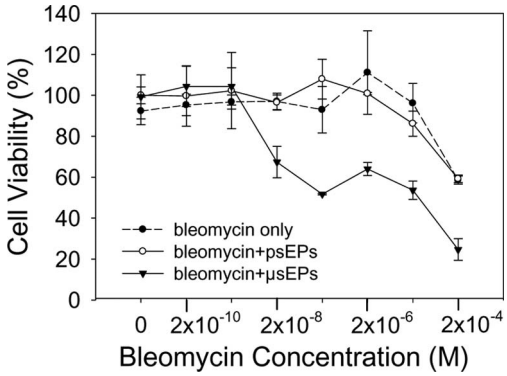

Fig. 7. B-16 cell survival for various drug (bleomycin) concentrations. The cell survival for bleomycin only and bleomycin delivery with microsecond pulses (100 μs) serve as sham and positive control. The number of microsecond pusle applied was 8. The number of subnanosecond pulses was 0.5 million. The error bars represent the standard deviation of the mean ($n = 3$).

indicates that even though there might be pores formed in the cell membrane, their size is not large enough to allow trypan blue to enter the cell. Another possibility is that these pores, even if they are formed and become larger in size, might reseal in less than 1 h, as has been observed with 800-ps-long pulses [20]. One other possibility is the pores may open to their largest size during pulsing, which may allow trypan blue molecules to enter the cell during the exposure. To test this ideas, we added trypan blue into the cell buffer before pulsing, and then applied the pulses to the cells in the buffer under the same conditions. Still, we were not able to observe any more trypan blue uptake compared to the sham.

The absence of large pores in the cell membrane was also shown in B16 cells. We added bleomycin (Sigma, molecular weight 1415.6Da), a chemotherapeutic agent, to the cell buffer [29]. We then applied the pulses to the cell buffer to see if bleomycin could enter the cell. The pulse number in this case was 500 000, still not sufficient to cause cell death. The cells were again cultured for 18 h prior to the WST assay. The survival result is shown in Fig. 7. It can be seen that the survival of the cells in the buffer with drug alone was reduced as the dose of bleomycin increased. This is an expected result. For cells treated with subnanosecond pulses, however, the survival was approximately the same as that of adding bleomycin only. Obviously, the added drug did not cause an increase in cell death. In contrast, for electroporation pulses (100 μs), which served as a positive control, the cell survival was decreased at a much lower bleomycin concentration (2×10^{-8} mol) in comparison to the toxic threshold (2×10^{-5} mol) of the drug alone. The electroporation pulses increased the rate of cell death due to uptake of bleomycin compared to using the drug alone or the use of subnanosecond pulses.

Both the trypan blue staining study and bleomycin study suggest that the nanopores, once they are formed, may not become

larger in size even though more pulses are applied. This may be due to the fact that the mechanism of such short pulses interacting with cell membrane is different than that of long pulses. For subnanosecond pulses, displacement current dominates the total current and the conduction current flowing through the pores is much less. Even though lower resistance nanopores formed, the majority of the current still passes through the rest of the cell membrane as displacement current. Conversely, for long electroporation pulses, the pore size might grow larger, if more pulses are applied. This expansion can be qualitatively understood by a positive-feedback mechanism. As the conduction current flows through the cell membrane, the current mostly chooses the high-conductivity path via pores. This results in high current density in these pores. The energy density within these narrow channels is, therefore, significantly higher than the nearby intact membrane. The temperature in the current path can, therefore, be further enhanced, and results in higher conductivity. Such positive-feedback mechanism may allow the pores to increase in diameter. To summarize, the pore formed in the subnanosecond range is most likely caused by the direct electric-field-induced conformational change, a strictly nonthermal process.

IV. Conclusion

Subnanosecond pulses, much shorter than the cell membrane charging time constant, were found to cause cell death and a change in membrane permeability. For the electric pulse condition, 200 ps, 25 kV/cm, using 1.8 million pulses, cell death ($\sim$20%) was observed 18 h after exposure. The cell death was caused by temperature-assisted electric field effects. A higher number of pulses (2.4 million) resulted in a greater temperature rise, and 90% cell death was observed. In either case, the cell membrane was found intact 1 h after exposure when tested by trypan blue.

While the pulses with durations shorter than the charging time of a cell membrane ($\sim$100 ns for mammalian cells) have a higher probability of acting upon intracellular structures, this proposition should not create the impression that cell membranes will be completely exempt from the effects of the subnanosecond pulses. Through the patch clamp study on NG108 cells, we have found that the cell membrane increased its conductance in response to subnanosecond electric pulses (electric field between 20–40 kV/cm, 200 ps). Also, the increase in the conductance lasted for at least 30 s after pulse application. This increased conductance occurred at much lower number of pulses than required for causing significant cell death, which suggests that this process is nonthermal. In addition, this process is not necessarily associated with cell death. More interestingly, the increased conductance only allowed a unidirectional current flow from the extracellular to the intracellular medium. This unidirectionality of current flow exhibited the same features as nanopores formed on the cell membrane after being exposed to nanosecond pulses. We note that if nanopores form in the cell membrane, the pores may not grow larger in size, even though more pulses are applied. These pores are not large enough to allow either trypan blue or bleomycin molecules to enter the cell interior. However, this scenario may change, if one applies higher electric fields, which may be sufficient to cause stronger conformational changes in the cell membrane.

In general, when using subnanosecond electric pulses for therapeutic applications in eliminating unwanted cells, we conclude that an electric field of at least 20 kV/cm is required. The cell death is due to both electric-field and thermal effects. Delivering pulses of higher electric field intensity at a lower repetition rate may allow us to separate the effects, which justifies further study. On the other hand, subnanosecond pulses offer a potential treatment modality that can modify cell membrane properties or alter the physiological conditions of cells to induce a desired response instead of causing cell death. In this case, much lower numbers of pulses are needed to obtain this effect. Such applications can include enhancement of wound healing, or hemostasis (blood clotting), by stimulating calcium influx into platelets [30].

References

[1] T. Y. Tsong, "Electroporation of cell membrane," *Biophys. J.*, VA, vol. 60, pp. 297–306, 1991.

[2] J. C. Weaver and Y. A. Chizmadzhev, "Theory of electroporation: A review," *Bioelectrochem. Bioenerget.*, vol. 41, pp. 135–160, 1996.

[3] J. C. Weaver, "Electroporation: A gneral phenomena for manipulating cells and tisses," *J. Cell. Biochem.*, vol. 51, pp. 426–435, 1993.

[4] L. M. Mir, L. F. Glass, G. Sersa, J. Teissie, C. Domenge, D. Miklavčič, M. J. Jaroszeski, S. Orlowski, D. S. Reintgen, Z. Rudolf, M. Belehradek, R. Gilbert, M. P. Rols, J. Belehradek, J. M. Bachaud, R. DeConti, B. Stabuc, M. Cemazar, P. Coninx, and R. Heller, "Effective treatment of cutaneous and subcutaneous malignant tumors by electrochemotherapy," *Brit. J. Cancer*, vol. 77, pp. 2336–2342, 1998.

[5] R. Heller, R. Gilbert, and M. J. Jaroszeski, "Clinical applications electrochemotherapy," *Adv. Drug Del. Rev.*, vol. 35, pp. 119–129, 1999.

[6] J. Teissie, M. Golzio, and M. P. Rols, "Mechanisms of cell membrane electropermeablilization: A minireview of our present knowledge," *Biochimica et Biophysica Acta (BBA)-General Subjects*, vol. 1724, pp. 270–280, 2005.

[7] A. G. Pakhomov, D. Miklavčič, and M. S. Markov, *Advanced Electroporation Techniques in Biology and Medicine*. Boca Raton, FL: CRC Press, 2010.

[8] T. B. Kotnik, G. Pucihar, and D. Miklavcic, "Induced transmembrane voltage and its correlation with electroporation-mediated molecular transport," *J. Membrane Biol.*, vol. 236, pp. 3–13, 2010.

[9] B. Rubinsky, G. Onik, and P. Mikus, "Irreversible electroporation: A new ablation modality-clinical implications," *Technol. Cancer Res. Treatment*, vol. 6, pp. 37–48, 2007.

[10] K. H. Schoenbach, S. J. Beebe, and E. S. Buescher, "Intracellular effect of ultrashort electrical pulses," *J. Bioelectromagn.*, vol. 22, pp. 440–448, 2001.

[11] S. J. Beebe, J. White, P. F. Blackmore, Y. Deng, K. Somers, and K. H. Schoenbach, "Diverse effects of nanosecond pulsed electric fields on cells and tissues," *DNA Cell Biol.*, vol. 22, pp. 785–796, 2003.

[12] K. H. Schoenbach, B. Hargrave, R. P. Joshi, J. F. Kolb, R. Nuccitelli, C. Osgood, A. Pakhomov, M. Stacey, R. J. Swanson, J. A. White, S. Xiao, and J. Zhang, "Bioelectric effects of intense nanosecond pulses," *IEEE Trans. Dielectr. Insul.*, vol. 14, no. 5, pp. 1088–1109, Oct. 2007.

[13] E. Tekle, H. Oubrahim, S. M. Dzekunov, J. F. Kolb, K. H. Schoenbach, and P. B. Chock, "Selective field effects on intracellular vacuoles and vesicle membranes with nanosecond electric pulses," *Biophys. J.*, vol. 89, pp. 274–284, 2005.

[14] P. T. Vernier, Y. Sun, and M. A. Gundersen, "Nanoelectropulse-driven membrane perturbation and small molecule permeabilization," *BMC Cell Biol.*, vol. 7, no. 37, pp. 1–16, 2006.

[15] A. G. Pakhomov, J. F. Kolb, J. A. White, and R. P. Joshi, "Long-lasting plasma membrane permeabilization in mammalian cells by nanosecond pulsed electric field (nsPEF)," *Bioelectromagnetics*, vol. 28, pp. 655–663, 2007.

[16] A. G. Pakhomov, A. M. Bowman, B. L. Ibey, F. M. Andrei, O. N. Pakhomova, and K. H. Schoenbach, "Lipid nanopores can form a stable ion chnnel-like conduction pathway in cell membrane," *Biochem. Biophys. Res. Commun.*, vol. 385, pp. 181–186, 2009.

[17] P. T. Vernier, Y. Sun, L. Marcu, C. M. Craft, and M. A. Gundersen, "Nanoelectropulse-induced phosphatidylserine tranlocation," *Biophys. J.*, vol. 86, pp. 4040–4080, 2004.

[18] T. B. Napotnik, M. Reberšek, T. Kotnik, E. Lebrasseur, G. Cabodevila, and D. Miklavčič, "Electropermeabilization of endocytotic vesicles in B16 F1 mouse melanoma cells," *Med. Biol. Eng. Comput.*, vol. 48, no. 5, pp. 407–413, 2010.

[19] T. Kotnik and D. Miklavčič, "Theoretical evaluation of voltage inducement on internal membranes of biological cells exposed to electric fields," *Biophys. J.*, vol. 90, pp. 480–491, 2006.

[20] K. H. Schoenbach, S. Xiao, R. P. Joshi, J. T. Camp, T. Heeren, J. F. Kolb, and S. J. Beebe, "The effect of intense subnanosecond electrical pulses on biological cells," *IEEE Trans. Plasma Sci.*, vol. 36, no. 2, pp. 414–422, Apr. 2008.

[21] R. P. Joshi, J. Song, K. H. Schoenbach, and V. Sridhara, "Aspects of lipid membrane bio-responses to subnanosecond, ultrahigh voltage pulsing," *IEEE Trans. Dielectr. Electr. Insul.*, vol. 16, no. 5, pp. 1243–1250, Oct. 2009.

[22] C. E. Baum, "Focal waveform of a prolate-spheroidal impulse-radiating antenna (IRA)," *Radio Sci.*, vol. 42, no. 6, pp. RS6–S27, 2007. DOI: 10.1029/2006RS003556.

[23] S. Xiao, S. Altunc, P. Kumar, C. Baum, and K. H. Schoenbach, "A reflector antenna for focusing in the near field," *IEEE Antennas Wireless Propag. Lett.*, vol. 9, no. 1, pp. 12–15, Jan. 2010.

[24] R Heller, M. Jaroszeski, J. Leo-Messina, R. Perrot, N. Van Voorhis, D. Reintgen, and R. Gilbert, "Treatment of B16 mouse melanoma with the combination of electropermeabilization and chemotherapy," *Bioelectrochem. Bioenerget.*, vol. 36, pp. 83–87, 1995.

[25] K. Schoenbach, J. Kolb, S. Xiao, S. Katsuki, Y. Minamitani, and R. Joshi, "Electrical breakdown of water in microgaps," *Plasma Sources Sci. Technol.*, vol. 17, pp. 024010-1–024010-10, 2008.

[26] J. E. Gruber and T. E. James, "Fast-pulse breakdown of nonuniform-field pressurised-air spark gaps," *Proc. Inst. Elect. Eng.*, vol. 115, no. 10, pp. 1530–1534, 1968.

[27] N. Matsuki, T. Ishikawa, Y. Imai, and T. Yamaguchi, "Low voltage pulses can induce apoptosis," *Cancer Lett.*, vol. 269, pp. 93–100, 2008.

[28] Z. Siwy, Y. Gu, H. A. Spohr, D. Baur, A. Wolf-Reber, R. Spohr, P. Apel, and Y. E. Korchev, "Rectification and voltage gating of ion currents in a nanofabricated pore," *Europhys. Lett.*, vol. 60, pp. 349–355, 2002.

[29] L. M. Mir, O. Tounekti, and S. Orlowski, "Bleomycin: Revival of an old drug," *Gen. Pharmacol.*, vol. 27, pp. 745–748, 1996.

[30] J. Zhang, P. F. Blackmore, B. Y. Hargrave, S. Xiao, S. J. Beebe, and K. H. Schoenbach, "Nanosecond pulse electric field (nanopulse): A novel non-ligand agonist for platelet activation," *Arch. Biochem. Biophys.*, vol. 471, pp. 240–248, 2008.

Authors' photographs and biographies not available at the time of publication.

The Effect of Intense Subnanosecond Electrical Pulses on Biological Cells

Karl H. Schoenbach, *Fellow, IEEE*, Shu Xiao, *Member, IEEE*, Ravindra P. Joshi, *Senior Member, IEEE*, James Thomas Camp, Tammo Heeren, *Member, IEEE*, Juergen F. Kolb, *Member, IEEE*, and Stephen J. Beebe

***Abstract*—Nanosecond electrical pulses have been successfully used to treat melanoma tumors by using needle arrays as pulse delivery systems. Reducing the pulse duration of intense electric field pulses from nanoseconds into the subnanosecond range will allow us to use wideband antennas to deliver the electromagnetic fields into tissue with a spatial resolution in the centimeter range. To explore the biological effect of intense subnanosecond pulses, we have developed a generator that provides voltage pulses of 160 kV amplitude, 200 ps rise time, and 800 ps pulse width. The pulses are delivered to a cylindrical Teflon chamber with polished flat electrodes at either end. The distance between the electrodes is variable and allows us to generate electric fields of up to 1 MV/cm in cell suspensions. The pulses have been applied to B16 (murine melanoma) cells, and the plasma membrane integrity was studied by means of trypan blue exclusion. For pulse amplitudes of 550 kV/cm, approximately 50% of the cells took up trypan blue right after pulsing, whereas only 20% were taking it up after 1 h. This indicates that the plasma membrane in a majority of the cells affected by the pulses recovers with a time constant of about 1 h. The cells that show trypan blue uptake after this time suffer cell death through apoptosis. Evaluation of the experimental results and molecular dynamics modeling results indicate that with a pulse duration of 800 ps, membrane charging and nanopore formation are the dominant bioelectric effects on B16 cells. This information has been used in a continuum model to estimate the increase in membrane permeability and, consequently, the increase in pore size caused by repetitive pulsing.**

***Index Terms*—Apoptosis, biological cells, cell membranes, nanopores, picosecond pulses, pulse power, wideband antenna.**

I. Introduction

THE EFFECT of high-intensity nanosecond electrical pulses on biological cells and tissue has received considerable attention by the scientific community, particularly in the past five years and has led to the establishment of a new research field: bioelectrics [1], [2]. In this time domain, the rise time of the pulse is faster than the charging time of the plasma membrane of most mammalian cells, meaning that the field will pass through the membrane into the cytoplasm. This effect can be understood qualitatively by considering the cell as an electrical circuit, describing the various cell membranes by their capacitances and the cytoplasm, which they enclose, by its resistance. Fig. 1(a) shows the cross section of a mammalian cell, with the only membrane-bound substructure shown being the nucleus. The cytoplasm, which fills much of the cell, contains dissolved proteins, electrolytes, and glucose and is moderately conductive, as are the nucleoplasm and the cytoplasm in organelles. On the other hand, the membranes that surround the cell and subcellular structures have low conductivity. We can therefore think of the cell as a conductor surrounded by an ideally insulating envelope, containing substructures with similar properties. The equivalent circuit of such a cell (which is considered as spherical for modeling purposes) with one substructure, the nucleus, is shown in Fig. 1(b).

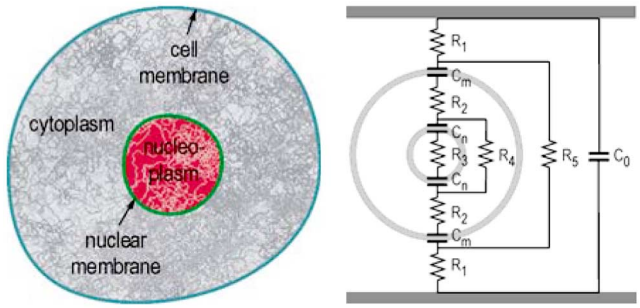

Fig. 1. (a) Structure of a biological cell (as would be seen with a light microscope). (b) Double-shell model of a biological cell and superimposed equivalent circuit of the cell [2].

If dc electric fields or pulses of long duration (compared to the charging time of the capacitor formed by the outer membrane) are applied, eventually, only the outer membrane will be charged; the electric field generated across subcellular membranes during charging will be zero for an ideal, fully insulating outer membrane. However, during the charging time of the outer membrane, we will also expect potential differences to be generated across subcellular membranes, an effect that will be stronger if the pulse rise time is shorter. Such charging times are in the submicrosecond range for human cells.

If the field is sufficiently large, it can have pronounced effects on intracellular organelles. High-voltage pulses that are nanoseconds to hundreds of nanoseconds long have been shown to penetrate into living cells to permeabilize intracellular organelles [3], [4] and release Ca^{2+} from the endoplasmic reticulum [5]–[7]. They provide a new approach for physically targeting intracellular organelles with many applications including activation of platelets and release of growth factors for accelerated wound healing [8] and precise control of apoptosis

Manuscript received September 20, 2007; revised January 9, 2008. This work is supported by Bioelectrics, Inc. and by an Air Force Office of Scientific Research Multidisciplinary University Research Initiative (MURI) grant for the Subcellular Response to Narrow-Band and Wide-Band Radio Frequency Radiation research program administered through Old Dominion University.

The authors are with the Old Dominion University, Frank Reidy Research Center for Bioelectrics, Norfolk, VA 23510 USA (e-mail: kschoenb@odu.edu).

Color versions of one or more of the figures in this paper are available online at http://ieeexplore.ieee.org.

Digital Object Identifier 10.1109/TPS.2008.918786

[9]–[12]. Most recently it has been shown that such pulsed electric fields cause shrinkage and even complete elimination of melanoma tumors [13].

Whereas the emphasis on bioelectric applications has been on nanosecond pulse effects, there are two good reasons to explore the effect of subnanosecond pulses on biological cells and tissue. The first is that for extremely short pulses, the dielectric properties, rather than the resistive characteristics of the media, determine the electric field distribution. In the equivalent circuit shown in Fig. 1(b), the conductance of the membranes is assumed to be zero, and the capacitive components of cytoplasm and nucleoplasm are neglected. These are assumptions that are only valid for a pulse duration that is long compared to the dielectric relaxation time of the cytoplasm $(\varepsilon_{\rm cp}/\sigma_{\rm cp})$, where $\varepsilon_{\rm cp}$ is the permittivity of the cytoplasm and $\sigma_{\rm cp}$ its conductivity. Only then can the capacitive term in the cytoplasm impedance be neglected compared to the resistive term. Based on the data listed in [14], this does not hold anymore for white blood cells when they are exposed to pulse durations short compared to one nanosecond. The electric fields in the various parts of the cell are then defined by their permittivity, rather than conductivity. For a membrane with a relative dielectric constant of 8, the electric field in the membrane is ten times higher than the electric field in the adjacent cytoplasm, which has a dielectric constant of 80. The electric field then acts directly on membrane proteins, rather than causing charging of the membrane, and, if sufficiently strong, can cause direct and instant conformational changes, such as voltage gating.

Second, besides providing the opportunity to enter a new domain of electric field-cell interactions, subnanosecond pulses will ultimately allow medical applications for delivery of pulsed electric fields without invasive electrodes, using antennas instead. A possible configuration that allows us to generate very high electric fields uses a focusing antenna [15] and may be able to induce apoptosis in tissue without using needles as the delivery system for electric pulses [13].

To explore effects of electrical pulses with durations right at the theoretical threshold where membrane-charging effects might become less important, and dielectric effects could already be present, we have applied 800-ps-long pulses with electric field amplitudes of up to 1 MV/cm to melanoma (B16) cells. We have measured the membrane integrity of these cells after pulsing and determined the fraction of dead cells and the type of cell death, depending on electric field intensity and number of pulses.

II. Experimental Setup and Methods

A pulsed power system, which is able to provide subnanosecond pulses to a biological load, was designed and built [16], [17] (Fig. 2). It is driven by a waveguide Marx-Bank [18] that charges a 10-cm-long coaxial cable (RG 213). The cable is discharged through a high-pressure spark gap. The system is able to generate 800-ps-long voltage pulses with an amplitude of 160 kV into a 50-Ω load. Voltages measured at the exposure cell, which acts as a high-impedance load, reach values of approximately 300 kV. A typical voltage pulse shape is shown in Fig. 3. With a gap distance of 3 mm, we have reached electric

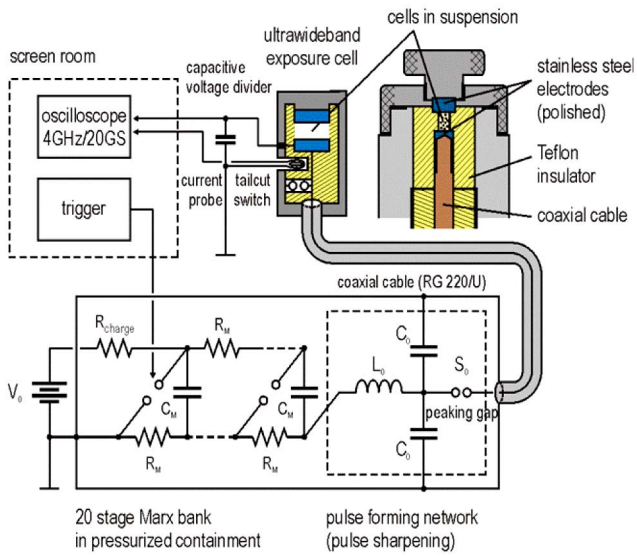

Fig. 2. Block diagram of ultrashort pulse generator with cross section of exposure system (upper right) [17].

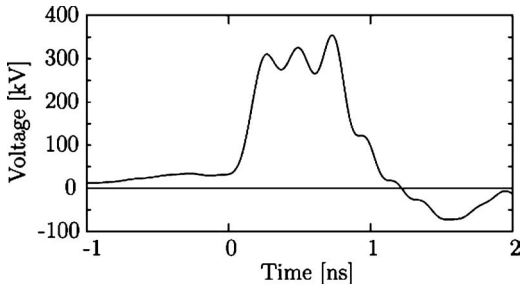

Fig. 3. Voltage measured at the exposure cuvette [17].

fields of up to 1 MV/cm. In spite of this extremely large field, no electrical breakdown was observed. This is in line with results obtained with 200 ns pulses, where the breakdown field for water exceeded values of 1 MV/cm in a pin-plate electrode configuration [19]. With pulse durations reduced by two orders of magnitude compared to those used in the water breakdown experiments, it is not surprising that even multimegavolts per centimeter fields in the subnanosecond range would not lead to electrical breakdown. However, streamer formation starting from microprotrusions at the electrodes cannot be excluded and needs to be studied [20].

A murine melanoma cell line, B16, was chosen as a mammalian cell model to determine the effects of these subnanosecond pulses on membrane permeability and cell death. The cells in suspension were placed between two plane parallel stainless steel electrodes (cuvette) with a variable gap distance d (3.15, 3.91, 5.35, and 10.67 mm, respectively). The cylindrical (flat-end) electrodes had a diameter of 2.75 mm. Cells loaded into the cuvette were exposed to multiple 800 ps pulses. The electric field in the suspension, V/d, with V being the pulse voltage, was varied between 150 kV/cm and 1 MV/cm. Cells loaded into cuvettes and merely placed into the circuit without being pulsed were used as controls.

Control (unpulsed) and treated (pulsed) cells were removed from the electroporation cuvettes following pulsing and mixed 1 : 1 with a volume of trypan blue at various times after

pulsing. A small volume of this mixture was then placed on a hemocytometer, or cell-counting slide. The cells were then counted as either stained or unstained. A total of at least 150 cells were counted, and the percentage of unstained cells was represented as percent trypan blue exclusion.

We used the trypan blue exclusion assay as an indicator of plasma membrane integrity and of cell viability. Trypan blue is normally impermeant to healthy cells. When cell membrane integrity is compromised, the dye is able to enter the cell and bind to protein, making the cell appear blue. Cells that take up this dye are usually considered dead or dying. However, in electroporation experiments with propidium iodide as a marker for membrane integrity, uptake of this marker after pulsing has also been reported for viable cells [21]. Because the size of trypan blue molecules (960 Da) is comparable to that of propidium iodide (668 Da), it cannot be assumed that observation of trypan blue uptake is necessarily an indication of cell death.

As a more definitive means to determine effects of subnanosecond pulses on cell survival, we used a clonogenic assay. The clonogenic, or colony-formation, assay measures cell survival based on the ability of a single cell to replicate successfully. In this manner, it challenges every cell in the population to undergo continuing division [22]. The clonogenic assay measures cell survival 6 days posttreatment and is linked to ultimate cell survival and accounts for all lethal mechanisms of cell injury. In this procedure, B16 cells were placed in a chamber and exposed to 1000 pulses at 800 ps and 550 kV/cm. After being allowed to grow for 6 days, single surviving clones had divided to form clusters. Clones that had formed clusters of at least 50 cells were counted as survivors and compared statistically to control survivors to yield a survival fraction percentage.

Previous results with 60-ns pulses indicated that cells died by apoptosis [9]–[12], a natural mechanism for deleting damaged or unwanted cells without inflammation, pain, or scarring [23]. To determine if apoptosis mechanisms accounted for cell death after exposure to subnanosecond pulses, we used a fluorescent cell-permeable irreversible inhibitor of active caspases as an apoptosis marker [9]–[12]. Cells are incubated with the marker and analyzed by flow cytometry at various times after treatment. The flavonoid phloretin, which induced caspase activation by a mitochondria-mediated apoptosis mechanism within 1 h in B16f10 cells (data not shown), was used as a positive control.

III. Results

The uptake of trypan blue was measured for electric field values between 150 kV/cm and 1 MV/cm, depending on the pulse number. Fig. 4 shows the results obtained for a fixed electric field value of 550 kV/cm 1 h after pulsing. There is no trypan blue uptake up to about 100 pulses. With pulse numbers increasing beyond the threshold, the trypan blue uptake (inverse of trypan blue exclusion) increases exponentially. This feature is typical for all the results obtained more than 1 h after pulsing.

The trypan blue results—obtained at 1 h or more after pulsing—are consistent with the results of clonogenic assays. Results with trypan blue uptake and the clonogenic assay both indicated similar survival rates at 1000 pulses at 800 ps and 550 kV/cm and 490 kV/cm, respectively. This showed that trypan blue uptake for these conditions can indeed be considered a marker for cell death, only if measured at least 1 h after pulsing, however. The mechanism for the cell death is, at least in part, caspase-dependent apoptosis, which is also shown in Fig. 4. Cell survival, the inverse of cell death, decreases in the same way as the intensity of the apoptosis marker increases.

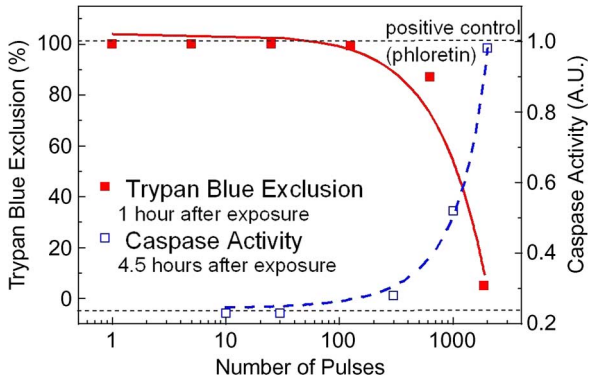

Fig. 4. Trypan blue exclusion, 1 hour after pulsing, and caspase activity, measured 4.5 h after pulsing, versus number of 800 ps pulses with average electric field amplitudes of 550 kV/cm (trypan blue exclusion) and 490 kV/cm (caspase activity), respectively.

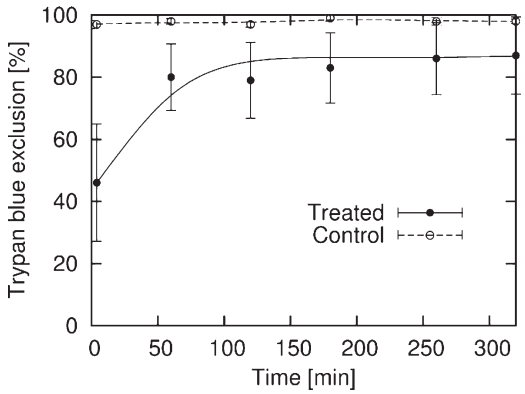

Fig. 5. Temporal development of trypan blue exclusion (625 pulses, 800 ps, 550 kV/cm).

The trypan blue exclusion results depicted in Fig. 4 hold for measurements where the trypan blue was added to the medium at least 1 h after pulsing. An interesting result was obtained when the temporal development of trypan blue uptake was studied with emphasis on the time before the one-hour mark. As shown in Fig. 5, a much larger percentage of the cells, approximately 50% for 625 pulses at 550 kV/cm, take up trypan blue right after pulsing (5 min), compared to less than 20%, which show trypan blue uptake an hour later. This indicates that poration of the cell membrane, which is caused by the 550-kV/cm pulses, is reversible for most of the cells and that the typical time constant for pore closure under these conditions is on the order of 1 h. The maximum appearance of active caspases, a marker for apoptosis, on the other hand, was observed 4.5 h postpulse.

For pulses with electric field intensity different from 550 kV/cm—varying between 150 kV/cm and 1 MV/cm—the trypan blue exclusion results are similar to those described for the 550 kV/cm case, however, the number of pulses required to reach the threshold for trypan blue uptake was strongly

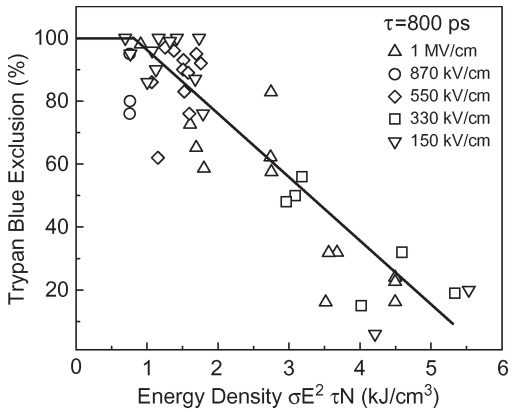

Fig. 6. Trypan blue exclusion fraction versus electrical energy density. Variables were the electric field intensity which was varied between 150 kV/cm and 1 MV/cm, and the number of pulses which was varied between 1 and 20,000.

dependent on the applied electric field intensity. For 150 kV/cm pulses it took 18,000 pulses to reach a 50% uptake mark, for 950 kV/cm pulses, it only required 125.

The data obtained with pulses of 800 ps duration seem to indicate that trypan blue uptake is a dose effect, scaling with the electrical energy density. Fig. 6 shows the trypan blue exclusion fraction (defined as: one minus uptake fraction) obtained 4 h after N pulses were applied with electric field amplitudes E, ranging from 150 kV/cm to 1 MV/cm, plotted versus the electric energy density, $\sigma E^2 \tau N$, where σ is the conductivity of the suspension (100 Ωcm). The exclusion of trypan blue decreases linearly with energy density above a threshold of approximately 0.8 kJ/cm^3.

IV. Discussion

A question that we tried to address with these studies is about the mechanism that causes cell death when such ultrashort pulses are applied. The trypan blue exclusion measurements indicate that the 800-ps pulses definitely have an effect on the outer membrane. The experimental results show immediate (minutes after pulsing) uptake of the dye, which means that nanopores with diameters large enough to allow trypan blue (960 Da) to pass have been created in the membrane.

The effect on the outer membrane is most likely a direct effect caused by membrane charging and subsequent membrane poration. The notion of membrane charging followed by poration of the membrane is also supported by modeling. Here, this is shown through molecular dynamics (MD) simulations. Details of MD simulations for membranes subjected to voltage pulsing have been reported by us elsewhere [25]–[27]. Essentially, the MD technique mimics atomistic many-body dynamics of a lipid bilayer surrounded by hundreds of water molecules. Fig. 7 shows the simulation results: a 2-ns snapshot of a section of the cell membrane (with its molecules shown in blue) in response to an 800-ps 560-kV/cm average external field. The time-dependent intensity of the membrane field used for the MD simulation was obtained by applying the actual external field input as a boundary condition to a distributed electrical representation of the cell [25], [26].

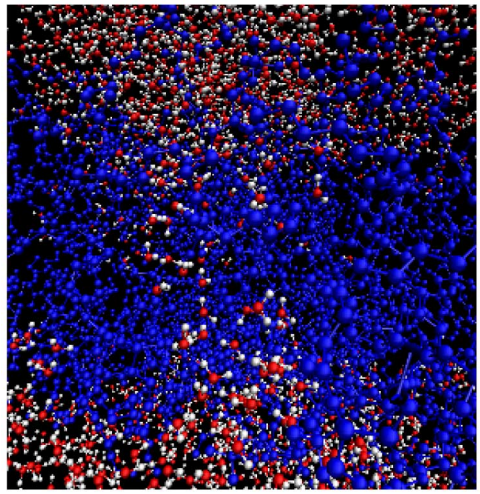

Fig. 7. MD results for subnanosecond pulsing, with water molecules (shown in red and white) beginning to form nanochannels through a cell membrane section, with its molecules shown in blue (snapshot at 2 ns after pulse application).

In Fig. 7, water is represented by the red-white combination (denoting the hydrogen-oxygen atoms) and is present at the top and bottom of the lipid bilayer. Small nanochannels of water (resembling "water nanowires") are clearly seen. Evidently, a large well-defined channel is not predicted to have formed through the membrane due to the ultrashort duration of the external voltage pulsing. However, some internal stressing and nanofracturing, indicative of a shock, exists and portends the eventual formation of aqueous pores within membranes. The salient feature is the distinct demonstration of electrical effects at membranes by the subnanosecond pulse.

The modeling results on the pore formation and the trypan blue exclusion studies (Fig. 5), which indicate pore closure with a time constant of about 1 h, can be used in a continuum model to estimate the transport of molecules through the membrane after pulsing (i.e., the rising part of the trypan blue exclusion curve in Fig. 5). The multipulse model for the pore transport model can be constructed on the following assumptions: 1) the subnanosecond pulsed electric field is "on" for a very short time compared to all other time scales; 2) each voltage pulse increases the size of existing pores on the cell membrane surface by an area, $\Delta S(t)$; 3) the increase in pore area for dye throughput, $S(t)$, after N pulses is given as

$$\mathrm{S(t)} = \sum \mathrm{N}^{1/2} \Delta \mathrm{S(t)} \tag{1}$$

where the $N^{1/2}$ term arises from the empirical scaling law discussed in [1]. In reality, the summation in (1) is an integral over the overall pore distribution; and 4) the effective pore area decreases exponentially upon pulse termination as the membrane reseals. Thus, the total, additional, pore area at any time t (assuming that the time for the pulse application is very short compared to the characteristic time constant for pore resealing τ), is given as

$$\mathrm{S(t)} = \mathrm{N}^{1/2} \Delta \mathrm{S}_0 \exp(-\mathrm{t}/\tau) \tag{2}$$

where ΔS_0 is the incremental area change produced by a single voltage pulse.

The concentration of dye molecules inside cells increases due to Fickian diffusion through the electropores. Applying Fick's law, and assuming that the dye concentration outside the cell remains almost unchanged, a time-dependent equation for $c(t)$, the concentration of dye inside a cell, can be obtained. This relation, after some algebra, is

$$\mathrm{c(t)} = \mathrm{c_0}\left[1 - \exp\left(-\{\mathrm{D}/(\mathrm{V_c}d)\}\left\{\int_{\mathrm{T}_d}^{\mathrm{t}} \mathrm{S(t)}d\mathrm{t}\right\}\right)\right] \quad (3)$$

where D is the dye diffusion coefficient, d is the membrane thickness, V_c is the average cell volume, and c_0 is the initial concentration. In (3), T_d represents a time delay after voltage pulsing in introducing the dye into the solution. Also, time t in (3) is limited to durations during which the resealing pore size remains larger than the dye molecule. With trypan blue already present in the solution at the time of voltage pulsing of the cell culture, $T_d = 0$. Integrating (3), with $S(t)$ given by (2), leads to the following relation for the excluded dye fraction $f(t, T_d)$:

$$\mathrm{f(t,T}_d) = \exp\left[\left\{\Delta \mathrm{S_0 DN}^{1/2}\tau/(\mathrm{V_c}d)\right\} \times \{\exp(-\mathrm{t}/\tau) - \exp(-\mathrm{T}_d/\tau)\}\right]. \quad (4)$$

The experimental data shown in Fig. 5, corresponding to an average external electric field of 560 kV/cm and 625 pulses, was analyzed based on the above diffusive transport model. The curve of Fig. 5 exhibits saturation in trypan blue exclusion beyond ~100 min. This implies that the membrane pores in viable cells would all have resealed to such an extent that uptake of the trypan blue molecules is no longer possible at times beyond 100 min. For such long times, the fraction as a function of the T_d can be expressed as

$$\begin{aligned}\mathrm{f(T}_d) &= \mathrm{C}\exp\left[-\left\{\left(\Delta \mathrm{S_0 DN}^{1/2}\tau\right)/(\mathrm{V_c}d)\right\}\exp(-\mathrm{T}_d/\tau)\right] \\ &\equiv \mathrm{C}\exp\left[-\mathrm{K_0}\exp(-\mathrm{T}_d/\tau)\right] \end{aligned} \quad (5)$$

where

$$\mathrm{K_0} = \left(\Delta \mathrm{S_0 DN}^{1/2}\tau\right)/(\mathrm{V_c}d) \quad (6)$$

and C is a scaling constant. Thus, there are essentially three critical fitting parameters, C, K_0, and τ, for the relation governing the fractional trypan blue exclusion dependence on time delay T_d. For the data given in Fig. 5, the following best-fit values were obtained: $\tau = 43.7$ min, $K_0 = 0.72$, and $C = 0.87$.

In the above, K_0 is an indirect measure of the relative ease for trypan blue uptake by the cells. It is characterized by the overall transport or inflow within a given population of cells. Factors that collectively influence its value are pore area, diffusion coefficient, number of pulses, and membrane resealing time. Also, the K_0 value can yield the total pore area increment ΔS_0 per pulse if the other parameters such as the number of pulses, cell volume, and dye diffusion coefficient are known. In this case, using $N = 625$, a cell radius of 5 μm, $\tau = 43.7$ min with D in the range 10^{-11} $\mathrm{m^2 s^{-1}} - 10^{-10}$ $\mathrm{m^2 s^{-1}}$ yields ΔS_0 to be in the range of 2.3 $\mathrm{nm^2}$–23 $\mathrm{nm^2}$. The range for D was roughly taken to be an order of magnitude lower than usually reported for single solvated ions [28] due to the large molecular size of trypan blue and the small openings of the membrane nanopores. This corresponds to radial increments in the size of the megapore per pulse in the 1–3 nm range, supposing that all the ΔS_0 change was to be attributed to a dominant megapore. In reality, there will be a distribution of pores with varying radii, and so the radial increments per pore and per pulse would vary around a value of $\Delta S/n$ where n is the number of pores in the cell.

Previous molecular dynamics (MD) calculations have shown the pore radii in response to nanosecond-pulsed electric fields, to be in the 1-nm range [25], [29]. Equilibrium mean pore radii (prepulse) are $r_0 = 0.4$ nm, and their density is approximately $1/\mu\mathrm{m}^2$ [30], [31]. In a spherical cell with a diameter of 10 μm we have, consequently, approximately $n = 100\pi$ pores. If we assume that each pulse contributes to an increase in the pore area, the mean (circular) pore area after N pulses would be

$$\pi \mathrm{r}^2 = \pi \mathrm{r}_0^2 + \Delta \mathrm{S_0 N}^{1/2}/\mathrm{n}. \quad (7)$$

For an initial pore radius, r_0, of 0.4 nm, the pore number for the 10-μm-diameter cell of $n = 100\pi$, and ΔS_0 varying between 2.3 and 23 $\mathrm{nm^2}$ (see previous section), the radius r after $N = 625$ pulses is in the range of 0.47–0.86 nm. These values are comparable to the estimated size of nanopores [25]–[27], [29].

The results of trypan blue uptake studies, performed after experiments with various pulse parameters, but keeping the pulse duration constant, seem to indicate that the observed biological effect is an energy density-dependent effect (see Section III, Results). However, this dependency on energy density does not hold true when the pulse duration is varied. This is clearly shown when we compare the 800-ps data (Fig. 6) with trypan blue uptake data obtained with pulses 10 ns long [Fig. 8(a)]. In Fig. 8(a) we have used experimental results on trypan blue exclusion reported in [24], complemented by results of a recent experimental study where the procedures were kept exactly the same as described in [24] (which are identical to those described in this manuscript). The results show clearly that the observed biological effect is not an energy density-dependent effect but follows a different scaling law.

Such a scaling law for biological effects of pulses with durations short compared to the plasma membrane charging time constant, but longer than the dielectric relaxation time of the cytoplasm, was discussed in [1]. The law is based on the hypothesis that in this pulse duration range (which covers both 800 ps as well as 10 ns pulses), any bioelectric effect is due to membrane charging, whether it is at the plasma membrane or subcellular membranes. It postulates that identical effects can be expected if the product of applied electric field intensity E, pulse duration τ, and the square root of the number of pulses N is kept constant. By replacing the energy density in the ordinate of Fig. 8(a), by this scaling parameter, $E\tau\sqrt{N}$, the trypan blue data for 800 ps and 10 ns can be described by the same parameter, shown in Fig. 8(b). It indicates that the observed effect of trypan blue uptake is a primary effect caused by membrane charging (and subsequent poration) and is not a

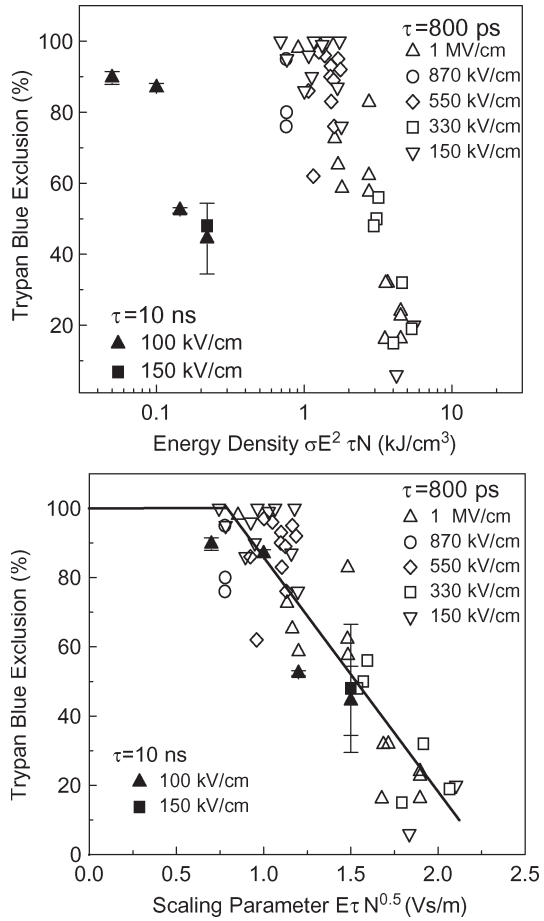

Fig. 8. (a) Trypan blue exclusion fraction versus electrical energy density for two pulse durations: 800 ps (open symbols) and 10 ns (closed symbols). The results show clearly that the dose (electrical energy density) required to achieve identical effects (trypan blue extension) is higher for shorter pulses. In this case, for 800 ps versus 10 ns pulses, it is approximately one order of magnitude. (b) Trypan blue exclusion versus the scaling parameter, $E\tau\sqrt{N}$ for two different pulse durations and a wide range of electric field amplitudes and pulse numbers.

secondary bioelectric effect, e.g., caused by the disintegration of the membrane after apoptosis has set in.

V. Conclusion

Whereas studies on nanosecond pulse effects have already led to medical applications, to our knowledge there are no experimental studies on the biological effects of subnanosecond pulses with external electric field amplitudes greater than 10 kV/cm. By using an 800-ps pulse generator we have, for the first time, focused on the effect of these pulses on melanoma cells (B16) with trypan blue as an indicator of membrane integrity. We have complemented the trypan blue studies with a clonogenic assay to determine cell death and a caspase assay to explore the mechanism of cell death.

The temporal development of the trypan blue uptake for 625 and 800 ps, respectively, and 550 kV/cm pulses shows that the generated nanopores reseal for most, but not all, of the cells with a time scale of 40 min to 1 h. Approximately 20% of the cells are not able to restore the integrity of the membrane and die, as shown by clonogenic studies. This recovery of the cell membrane is detrimental for applications such as tumor treatment, where the goal is to minimize viability. However, for applications where drugs are to be delivered into cells through the plasma membrane, this effect would be very beneficial. It might allow delivery of certain drugs or nanoparticles into the cell without strongly affecting the viability of the cells. In addition, the modeling studies indicate the possibility of externally influencing dye uptake in the first hour after pulsing through variations in the number of pulses and/or the voltage magnitude. This could be important for tailored drug delivery and selective gene/molecule insertion.

All our results point to membrane charging and nanoporation [25]–[27], [29] as a dominant effect of 800 ps pulses, which not only causes reversible pore formation in the plasma membrane but might also be the reasons for irreversible changes in the membrane that lead to cell death. That means that the equivalent circuit shown in Fig. 1 is still likely to describe the response of cells to electrical pulses, rather than a circuit that includes the capacitance of the cytoplasm. This conclusion is supported by results shown in Fig. 8(b), where the trypan blue exclusion is plotted versus the scaling parameter $E\tau\sqrt{N}$. Scaling with this parameter is based on the assumption that any observed effect is caused by membrane charging [1]. Only when this assumption is valid do the results of the 800 ps experiments and the result from a 10-ns study fall onto the same curve.

However, the fact that apoptosis seems to be the major mechanism of cell death (Fig. 5) could also indicate that direct effects on membrane proteins play a role in cell death and that the disintegration of the membrane (observed 1 h after pulsing) is partly a secondary effect due to apoptosis. Because we are in a transition range between membrane charging and direct dielectric effects with our 800-ps pulses, it is likely that both membrane charging and dielectric effects contribute to the observed biological effects. Further experiments with shorter pulses (250 ps) are underway to extend the parameter range further toward the dielectric range and to better discriminate between membrane charging and dielectric effects, such as direct effects of the electric field on membrane proteins.

One reason to extend our range of observation towards the 100-ps range is the possible use of antennas as pulse delivery systems. The use of needle or plate electrodes in therapeutic applications that rely on electroporation [32] or nanosecond-pulsed electric fields (nsPEF) [13] requires that the electrodes are brought into close contact with the treated tissue. This limits the application to treatments of tissue close to the skin, or tissue close to the surface of the body. The use of antennas, on the other hand, would allow one to apply such electric fields to tissues (tumors) that are not easily accessible with needles. Also, focusing electrical energy on the target would reduce the damage to the tissue layers surrounding the target and the skin. The spatial resolution of an electric field generated in tissue depends on the pulse duration and the permittivity of the tissue.

However, whereas the research on wideband antennas has mainly focused on the design and development of antennas operating in the far field, an "antenna" or better pulse delivery system that is used for bioelectrics applications would need to operate in the near field. There are several concepts for such a delivery system. These are mainly based on the use of a

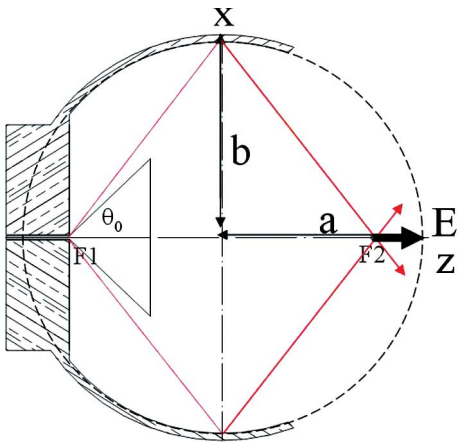

Fig. 9. A focusing antenna using a conical wave launcher and a prolate spheroidal reflector [34]. The electromagnetic wave is launched at the focal point F1, the endpoint of a coaxial cable, expands along the conical wave launcher, is reflected from the prolate spheroidal reflector, and focused again in focal point F2.

prolate spheroidal reflector, where the pulse is launched from one focal point and reflected onto a second focal point. For our application, the second focal point would be the location of a tumor inside the body. Much of the design work on such delivery systems is done at the Air Force Research Laboratories and at the University of New Mexico, both in Albuquerque, under the guidance of C. Baum [33].

At Old Dominion University, we have concentrated our efforts, in cooperation with the team of C. Baum, on a near-field antenna where the electric field generated in the target is focused by means of a prolate spheroidal reflector, in connection with a conical wave launcher (Fig. 9) [34]. The E-field at the focal point has only longitudinal components. For a 100-ps risetime, step-function input pulse, the focusing spot size (full width at half maximum) in tissue is 2–3 cm along the z-axis and <1 cm along the x-axis. For a 100-kV input pulse, the peak E-field at the second focal point was calculated to be 250 kV/cm.

Our results, which provide information on membrane integrity, and cell viability, indicate that the required electric field values for apoptosis are far above the values that can be reached with wideband antennas, even with focusing reflectors. However, by using sensitizing agents in combination with wideband radiation it might be possible to reduce the threshold for apoptosis induction considerably. On the other hand, besides apoptosis, induction of nonlethal effects such as calcium release from subcellular structures [5]–[7] or neurotransmitter release can be an attractive application of this new method. Calcium is a key regulator of numerous cellular functions and also influences cell signaling. This would, for example, have implications for electrostimulation. Because the release of calcium has been shown to require much lower electric fields than does apoptosis induction, the constraints on the pulse generator can be relaxed considerably. In general, the use of subnanosecond pulses not only allows us to enter a new field of field-cell interactions but might open the door to a range of therapeutic applications that require electromagnetic energy delivery into tissue not easily accessible by solid electrodes, such as needles.

REFERENCES

[1] K. H. Schoenbach, B. Hargrave, R. P. Joshi, J. F. Kolb, C. Osgood, R. Nuccitelli, A. Pakhomov, R. J. Swanson, M. Stacey, J. A. White, S. Xiao, J. Zhang, S. J. Beebe, P. F. Blackmore, and E. S. Buescher, "Bioelectric effects of intense nanosecond pulses," *IEEE Trans. Dielectr. Electr. Insul.*, vol. 14, no. 5, pp. 1088–1119, Oct. 2007.

[2] K. H. Schoenbach, R. P. Joshi, J. F. Kolb, N. Chen, M. Stacey, P. F. Blackmore, E. S. Buescher, and S. J. Beebe, "Ultrashort electrical pulses open a new gateway into biological cells," *Proc. IEEE*, vol. 92, no. 7, pp. 1122–1137, Jul. 2004.

[3] K. H. Schoenbach, S. J. Beebe, and E. S. Buescher, "Intracellular effect of ultrashort electrical pulses," *Bioelectromagnetics*, vol. 22, no. 6, pp. 440–448, 2001.

[4] E. S. Buescher and K. H. Schoenbach, "Effects of submicrosecond, high intensity pulsed electric fields on living cells-intracellular electromanipulation," *IEEE Trans. Dielectr. Electr. Insul.*, vol. 10, no. 5, pp. 788–794, Oct. 2003.

[5] P. T. Vernier, Y. H. Sun, L. Marcu, C. M. Craft, and M. A. Gundersen, "Nanosecond pulsed electric fields perturb membrane phospholipids in T lymphoblasts," *FEBS Lett.*, vol. 572, no. 1–3, pp. 103–108, 2004.

[6] J. A. White, P. F. Blackmore, K. H. Schoenbach, and S. J. Beebe, "Stimulation of capacitative calcium entry in HL-60 cells by nanosecond pulsed electric fields," *J. Biol. Chem.*, vol. 279, no. 22, pp. 22 964–22 972, May 2004.

[7] E. S. Buescher, R. R. Smith, and K. H. Schoenbach, "Submicrosecond intense pulsed electric field effects on intracellular free calcium: Mechanisms and effects," *IEEE Trans. Plasma Sci.*, vol. 32, no. 4, pp. 1563–1572, Aug. 2004.

[8] J. Zhang, P. F. Blackmore, B. Y. Hargrave, S. Xiao, S. J. Beebe, and K. H. Schoenbach, "Nanosecond pulse electric field (nanopulse): A novel non-ligand agonist for platelet activation," *Arch. Biochem. Biophys.*, vol. 471, no. 2, pp. 240–248, 2008. DOI:10.1016/j.abb.2007.12.009.

[9] S. J. Beebe, P. M. Fox, L. J. Rec, E. L. Willis, and K. H. Schoenbach, "Nanosecond, high-intensity pulsed electric fields induce apoptosis in human cells," *FASEB J.*, vol. 17, no. 11, pp. 1493–1495, 2003.

[10] S. J. Beebe, P. F. Blackmore, J. White, R. P. Joshi, and K. H. Schoenbach, "Nanosecond pulsed electric fields modulate cell function through intracellular signal transduction mechanisms," *Physiol. Meas.*, vol. 25, no. 4, pp. 1077–1093, Aug. 2004.

[11] S. J. Beebe, J. White, P. F. Blackmore, Y. Deng, K. Somers, and K. H. Schoenbach, "Diverse effects of nanosecond pulsed electric fields on cells and tissues," *DNA Cell Biol.*, vol. 22, no. 12, pp. 785–796, 2003.

[12] P. T. Vernier, A. Li, L. Marcu, C. M. Craft, and M. A. Gundersen, "Ultrashort pulsed electric fields induce membrane phospholipid translocation and caspase activation: Differential sensitivities of Jurkat T lymphoblasts and rat glioma C6 cells," *IEEE Trans. Dielectr. Electr. Insul.*, vol. 10, no. 5, pp. 795–809, Oct. 2003.

[13] R. Nuccitelli, U. Pliquett, X. Chen, W. Ford, J. Swanson, S. J. Beebe, J. F. Kolb, and K. H. Schoenbach, "Nanosecond pulsed electric fields cause melanomas to self-destruct," *Biochem. Biophys. Res. Commun.*, vol. 343, no. 2, pp. 351–360, May 2006.

[14] I. Ermolina, Y. Polevaya, Y. Feldman, B. Ginzburg, and M. Schlesinger, "Study of normal and malignant white blood cells by time domain dielectric spectroscopy," *IEEE Trans. Dielectr. Electr. Insul.*, vol. 8, no. 2, pp. 253–261, Apr. 2001.

[15] C. E. Baum, *Producing Large Transient Electromagnetic Fields in a Small Region: An Electromagnetic Implosion, Sensor and Simulation Notes*, Aug. 2005. Note 501.

[16] T. Heeren, J. T. Camp, J. F. Kolb, K. H. Schoenbach, S. Katsuki, and H. Akiyama, "250 kV Sub-nanosecond pulse generator with adjustable pulse-width," *IEEE Trans. Dielectr. Electr. Insul.*, vol. 14, no. 4, pp. 884–888, Aug. 2007.

[17] K. H. Schoenbach, S. Katsuki, H. Akiyama, T. Heeren, J. F. Kolb, S. Xiao, T. Camp, R. P. Joshi, C. Osgood, R. Nuccitelli, and S. J. Beebe, "Biological effects of intense subnanosecond electrical pulses," in *Proc. Conf. Rec. IEEE Power Modulator Conf.*, Washington, DC, May 14–18, 2006, pp. 573–576.

[18] W. J. Carey and J. R. Mayes, "Marx generator design and performance," in *Proc. Power Modulator Symp.*, 2002, pp. 625–628.

[19] S. Xiao, J. Kolb, S. Kono, S. Katsuki, R. P. Joshi, M. Laroussi, and K. H. Schoenbach, "High power water switches: Postbreakdown phenomena and dielectric recovery," *IEEE Trans. Dielectr. Electr. Insul.*, vol. 11, no. 4, pp. 604–612, Aug. 2004.

[20] S. Katsuki, H. Akiyama, A. Abou-Ghazala, and K. H. Schoenbach, "Parallel streamer discharges between wire and plane electrodes in water," *IEEE Trans. Dielectr. Electr. Insul.*, vol. 9, no. 4, pp. 498–506, Aug. 2002.

[21] M. P. Rols and J. Teissie, "Electropermeabilization of mammalian cells to macromolecules: Control by pulse duration," *Biophys. J.*, vol. 75, no. 3, pp. 1415–1423, Sep. 1998.
[22] N. A. P Franken, H. M Rodermond, J. Stap, J. Haveman, and C. van Bree, "Clonogenic assay of cells in vitro," *Nature Protocols*, vol. 1, no. 5, pp. 2315–2319, 2006.
[23] C. B. Thompson, "Apoptosis in the pathogenesis and treatment of disease," *Science*, vol. 267, no. 5203, pp. 1456–1462, Mar. 10, 1995.
[24] Y. Sun, S. Xiao, J. A. White, J. F. Kolb, M. Stacey, and K. H. Schoenbach, "Compact, nanosecond, high repetition-rate, pulse generator for bioelectric studies," *IEEE Trans. Dielectr. Electr. Insul.*, vol. 14, no. 4, pp. 863–870, Aug. 2007.
[25] Q. Hu, S. Viswanadham, R. P. Joshi, K. H. Schoenbach, S. J. Beebe, and P. F. Blackmore, "Simulations of transient membrane behavior in cells subjected to a high-intensity ultrashort electric pulse," *Phys. Rev. E, Stat. Phys. Plasmas Fluids Relat. Interdiscip. Top.*, vol. 71, no. 3, pp. 031914/1–031914/9, 2005.
[26] Q. Hu, S. Viswanadham, R. P. Joshi, J. Kolb, and K. H. Schoenbach, "Molecular dynamics analysis of high electric pulse effects on bilayer membranes containing DPPC and DPPS," *IEEE Trans. Plasma Sci.*, vol. 34, no. 4, pp. 1405–1411, Aug. 2006.
[27] Q. Hu, R. P. Joshi, and K. H. Schoenbach, "Simulations of nanopore formation and phosphatidylserine externalization in lipid membranes subjected to a high-intensity, ultra-short electric pulse," *Phys. Rev. E, Stat. Phys. Plasmas Fluids Relat. Interdiscip. Top.*, vol. 72, no. 3, pp. 031902/1–031902/10, 2005.
[28] R. M. Lynden-Bell and J. C. Rasaiah, "Mobility and solvation of ions in channels," *J. Chem. Phys.*, vol. 105, no. 20, pp. 9266–9280, Nov. 1996.
[29] Z. Vasilkoski, A. T. Esser, T. R. Gowrishankar, and J. C. Weaver, "Membrane electroporation: The absolute rate equation and nanosecond time scale pore creation," *Phys. Rev. E, Stat. Phys. Plasmas Fluids Relat. Interdiscip. Top.*, vol. 74, no. 2, pp. 021904/1–021904/12, 2006.
[30] V. F. Pastushenko, V. B. Arakelyan, and Y. A. Chizmadzhev, "Electric breakdown of bilayer membranes: VI. A stochastic theory taking into account the processes of defect formation and death: Membrane lifetime distribution function," *Bioelectrochem. Bioenergetics*, vol. 6, pp. 89–95, 1979.
[31] J. C. Weaver and R. A. Mintzer, "Decreased bilayer stability due to transmembrane potentials," *Phys. Lett. A*, vol. 86, pp. 57–59, 1981.
[32] S. B. Dev, D. B. Rabussay, G. Widera, and G. A. Hofmann, "Medical applications of electroporation," *IEEE Trans. Plasma Science*, vol. 228, pp. 206–223, 2000.
[33] C. E. Baum, "Focal waveform of a prolate-spheroidal impulse-radiating antenna (IRA)," *Radio Science*, vol. 42, 2007. RS6S27.
[34] S. Xiao, M. A. Migliaccio, J. T. Camp, J. F. Kolb, K. H. Schoenbach, and C. E. Baum, "A wide-band focusing system for bioelectric applications," in *Proc. PPPS*, Albuquerque, NM, Jun. 2007.

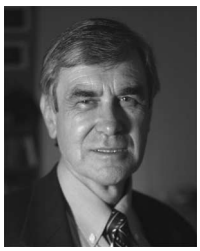

Karl H. Schoenbach (F'94) received the Dipl. degree in physics and the Dr.rer.nat. degree in physics in 1966 and 1970, respectively, from the Technische Hochschule Darmstadt (THD), Darmstadt, Germany.

From 1970–1978, he was working at the THD in the areas of high-pressure gas discharge physics and on dense plasma focus. From 1979–1985, he was on the faculty at Texas Tech University, Lubbock. In 1985, he joined Old Dominion University, Norfolk, VA, where he now concentrates his research efforts on high-pressure glow discharges, glow (streamer) discharges in liquids, and environmental and medical applications of pulse power technology. He has chaired a number of workshops and conferences, among them the 1991 IEEE International Conference on Plasma Science, and the First International Symposium on "Nonthermal Medial/Biological Treatments Using Electromagnetic Fields and Ionized Gases" (ElectroMed99) in 1999. He was elected a Fellow of the IEEE in 1994 for "contributions to the research and development of very-high-power electronic devices," and received the 2000 High Voltage Award sponsored by the Dielectric and Electrical Insulation Society of the IEEE, and the Peter Haas Pulsed Power Award in 2007. He has published over 300 papers in refereed journals and in conference proceedings and has been an Associate Editor of the IEEE TRANSACTIONS ON PLASMA SCIENCE since 1989, Guest Editor for special issues in several IEEE TRANSACTIONS, and coeditor of such books as *Low Temperature Plasma Physics* (2001), *Atmospheric Pressure Air Plasmas* (2004), and *Low Temperature Plasmas* (2008).

Shu Xiao (M'04) received the Ph.D. degree in electrical engineering from Old Dominion University, Norfolk, VA, in 2004. He was in the Ph.D./Master joint program in the University of Electronic Sciences and Technology of China, Sichuan, from 1996 to 2001.

His research interests include pulse power, electrical discharges in liquid and gas, and manipulation of biological cells with nanosecond pulses. He is currently working as a Research Assistant Professor at the Frank Reidy Center for Bioelectrics, Norfolk.

Ravindra P. Joshi (M'83–SM'95) received the B. Tech. and M. Tech. degrees in electrical engineering from the Indian Institute of Technology, Delhi, in 1983, and 1985, respectively. He earned the Ph.D. degree in electrical engineering from Arizona State University, Tempe, in 1988. He was a postdoctoral fellow at the Center of Solid State Electronics Research, Arizona State University.

In 1989, he joined the Department of Electrical and Computer Engineering, Old Dominion University, Norfolk, VA, as an Assistant Professor. He is currently a full Professor, and involved in research broadly encompassing modeling and simulations of charge transport, nonequilibrium phenomena, and bioelectrics. He also has used Monte Carlo methods for simulations of high-field transport in bulk and quantum well semiconductors. He is the author of over 80 journal publications, and he has been a visiting scientist at Oak Ridge National Laboratory, Philips Laboratory, Motorola, and NASA Goddard. He is a Guest Editor for a Special Issue of the IEEE TRANSACTIONS ON PLASMA SCIENCE.

James Thomas Camp received the B.S. degree in physics from Christopher Newport University, Newport News, VA, in 2006. He is currently working toward the Ph.D. degree in electrical and computer engineering at Old Dominion University, Norfolk, VA. His current research interests include picosecond-pulsed power physics and technology and picosecond pulsed-electric-field-induced biological effects.

Tammo Heeren (M'00) [redacted]. He received the B.S. degree from the University of Applied Science, Wilhelmshaven, Germany, in 1998, and the M.S.E.E. and Ph.D. degrees from Texas Tech University, Lubbock, in 2000 and 2003, respectively.

He was a Senior Research Assistant with the Center for Pulsed Power and Power Electronics, Texas Tech University. From 2004 to 2005, he was a Visiting Associate Professor with Kumamoto University, Kumamoto, Japan. In 2005, he was with the Frank Reidy Research Center for Bioelectrics, Old Dominion University, Norfolk, VA. Since 2007, he has been with Alcon Laboratories, Irvine, CA, where he is currently a Senior Engineer.

Juergen F. Kolb (M'02) received the Dr.rer.nat. degree in physics from the University of Erlangen, Erlangen, Germany, in 1999.

He continued his work on the interaction of heavy ion beams with plasmas as a Postdoctoral Research Associate at the Technische Hochschule Darmstadt, Darmstadt, Germany. In 2002, he joined the Physical Electronics Research Institute and the Center for Bioelectrics, Old Dominion University, Norfolk, VA. His current research interests include the effects of pulsed electric fields on biological cells, nonthermal atmospheric pressure air plasmas for biomedical and environmental applications, and the use of liquid dielectrics in pulsed power applications. He is currently an Assistant Professor in Bioelectrics, Electrical and Computer Engineering Department, Old Dominion University.

Stephen J. Beebe received the B.S. degree in zoology from Ohio University, Athens, in 1970 and the Ph.D. degree in medical sciences (pharmacology) from the Medical College of Ohio, Toledo, in 1982.

He was a Postdoctoral Fellow in the Howard Hughes Medical Institute and the Department of Molecular Physiology and Biophysics at Vanderbilt University, Nashville, TN (1982–1986). He was a Fulbright and Marshal Scholar in Department of Medical Biochemistry and the National Hospital in Oslo Norway (1987–1988). He is currently a Professor in the Frank Reidy Research Center for Bioelectrics at Old Dominion University, Norfolk VA. For the past 30 years, his research has focused on cell signal transduction with emphasis on structure-function relationships of the cAMP-dependent protein kinases (cAPK) for the regulation of physiological functions including glycogen and lipid metabolism, transcription, sperm-egg interactions, differentiation, proliferation, and apoptosis. More recently, his work has focused on cell and tissue responses to nanosecond pulsed electric fields as a means to modulate signal transduction for wound healing and cancer control.

Dr. Beebe was awarded various honors during his career including the Howard Hughes Medical Institute Postdoctoral Fellowship, the Fulbright Scholar Award, Oslo, Norway, and the Norwegian Marshall Scholar Award, and Outstanding Senior Visiting Scientist from the Norwegian Research Council. He was also a recipient of the Iwao Yasuda Award for contributions to biomedical research by the Society for Physical Regulation in Biology (2002) and Medicine and the Martin Black Prize from the Institute of Physics and Engineering in Medicine (2005).